

5G ALLSTAR



Document Number: H2020-EUK-815323/5G-ALLSTAR/D3.1

Project Name:
5G Agile and flexible integration of Satellite And cellular (5G-ALLSTAR)

Deliverable D3.1

Spectrum usage analysis and channel model

Date of delivery: 30/06/2019
Start date of Project: 01/07/2018

Version: 1.0
Duration: 36 months

Deliverable D3.1

Spectrum usage analysis and channel model

Project Number:	H2020-EUK-815323
Project Name:	5G AgiLe and fLexible integration of SaTellite And cellular

Document Number:	H2020-EUK-815323/5G-ALLSTAR/D3.1
Document Title:	Spectrum usage analysis and channel model
Editor(s):	Stephan Jaeckel (FhG-HHI)
Authors:	Stephan Jaeckel, Leszek Raschkowski (FhG-HHI), Junhyeong Kim, Gosan Noh (ETRI), Marjorie Thary, Jean-Michel Houssin (TAS), Ji-In Kim (KTSat), Nicolas Cassiau (CEA)
Dissemination Level:	PU
Contractual Date of Delivery:	30/06/2019
Security:	Public
Status:	Final
Version:	1.0
File Name:	5G-ALLSTAR_D3.1.docx

Abstract

This deliverable has been created as part of the work in the project 5G-ALLSTAR Work Package (WP3) on Spectrum Sharing. It reports on the findings of the spectrum usage analysis and presents two radio propagation models for the evaluation of interference scenarios between terrestrial and non-terrestrial networks.

The main outcomes are the two methodologies to model the radio propagation. The first one is based on a geometry-based stochastic model, whereas the second one is based on ray-tracing.

Keywords

Spectrum, frequency bands, channel model, ray-tracing, quadriga, non-terrestrial, dual-connectivity, 5G

Acknowledgements

We would like to acknowledge and thank the assistance of Prof. Ke Guan's team at Beijing Jiaotong University. In addition, we would like to thank Mr. Johannes Dommel (FhG-HHI) for the valuable review of the deliverable.

Executive Summary

This deliverable presents the findings of the spectrum usage analysis and two approaches to model the radio propagation for a system consisting of a terrestrial and a non-terrestrial network part. A hybrid system of satellites and base stations on the ground paves the way towards seamless worldwide connectivity. Unserved and underserved areas could be covered by an overlaying satellite constellation, whereas densely populated areas, such as cities, could be provided by a network of base stations on the ground. In addition, scenarios are envisioned where users could benefit from multi-connectivity towards both systems at the same time.

The 5G-ALLSTAR project aims at enabling this vision by developing new concepts to integrate a satellite overlay into the 5G ecosystem. Due to the limited resources in terms of frequency spectrum, the project investigates regulations and foreseen spectrum allocations to optimally utilize bands, possibly in a shared manner.

The radio propagation of terrestrial networks as well as of non-terrestrial networks has been studied for decades from their respective research groups. Since the 5G-ALLSTAR project envisions an integrated solution, jointly modelling both networks is of highest importance in order to evaluate mutual interference. Two conventional model approaches are considered in this work, i.e. a geometry-based stochastic model and a ray-tracing based model. The project benefits from the two models as both individual models have their respective advantages and disadvantages.

Contents

1	Introduction	1
2	Spectrum usage analysis	2
2.1	Spectrum bands	2
2.1.1	Overall 5G spectrum situation	2
2.1.2	Satellite frequency bands potentially eligible for 5G	4
2.2	Non-terrestrial networks deployment scenarios	8
2.2.1	Deployment scenarios selection	8
2.2.2	Beam size and service area	10
2.2.3	Space segment parameters	11
2.2.4	Gateway	13
2.3	Terrestrial networks deployment scenarios	13
2.3.1	Candidate scenarios	13
2.3.2	Radio unit deployment	14
2.3.3	RF and antenna characteristics	15
2.3.4	Terrestrial network model	16
2.4	Terminal deployment scenarios	17
2.4.1	Terminal types	17
2.4.2	Terminal distribution and movement	18
2.4.3	Vehicular terminal details	18
2.5	Parameters to characterize	20
3	Geometry-based stochastic channel model for cellular and satellite systems	21
3.1	Modelling objectives	21
3.2	Coordinate systems	22
3.3	Non-GSO satellite orbit model	23
3.4	Antenna models	30
3.4.1	Reflector antenna model	30
3.4.2	Model for terrestrial base station antennas	32
3.5	Spatially-consistent large-scale fading model	34
3.5.1	LOS probability model	35
3.5.2	Path loss and clutter loss	36
3.5.3	Atmospheric absorption	37
3.5.4	Shadow fading	38
3.5.5	Multipath parameters	41
3.5.6	Inter-parameter correlation model	44
3.6	Small-scale-fading model	45
4	Ray tracing-based channel model	48
4.1	Objective	48
4.2	CloudRT simulator	48
4.3	Excess propagation attenuation for a terrestrial link	49
4.3.1	Attenuation due to atmospheric gases	49
4.3.2	Attenuation due to rain	49
4.4	Excess propagation attenuation for a satellite link	50
4.4.1	Attenuation due to atmospheric gases	50
4.4.2	Attenuation due to rain	51
4.4.3	Attenuation due to clouds and fog	51
4.4.4	Attenuation due to tropospheric scintillation	52
4.4.5	Estimation of total attenuation due to multiple sources of simultaneously occurring atmospheric attenuation	52
4.5	Simulation configuration	52
4.5.1	Vehicle types	52
4.5.2	Antenna model	53
4.5.3	Scenario description	54
4.5.4	Configuration details	56

4.6	Key channel parameters	59
4.6.1	Path loss	60
4.6.2	RMS delay spread.....	62
4.6.3	Rician K -factor	64
4.6.4	Angular domain.....	67
5	Conclusions	69
References.....		71

List of Figures

Figure 2-1: S-band MSS allocation to satellite operators	4
Figure 2-2: Status and plans for the 3.3 – 4.2 GHz range all over the world (source: GSA).....	5
Figure 2-3: Potential allocation of 3.7-4.2 GHz band	6
Figure 2-4: FSS, MSS, BSS and FS allocations in Ka-band in the ITU radio regulations – Source: Global VSAT Forum, November 2011	7
Figure 2-5: 5G-ALLSTAR reference system architecture.....	8
Figure 2-6: Typical non-terrestrial network deployment	8
Figure 2-7: Satellite beam bore sight direction definition	10
Figure 2-8: KOREASAT-6 satellite coverage map	11
Figure 2-9: Highway deployment scenario.....	14
Figure 2-10: Urban grid deployment scenario.....	14
Figure 2-11: RU location at a road: a) beside a road; b) middle of a road.....	15
Figure 2-12: RU location at an intersection: a) corner of an intersection; b) center of an intersection.....	15
Figure 2-13: Beam radiation pattern of each array antenna.....	15
Figure 2-14: Frequency usage plan for terrestrial network.....	16
Figure 2-15: Terrestrial network UMi deployment example.....	17
Figure 2-16: Beam switching functionality at a vehicular terminal	19
Figure 2-17: RF and antenna structure of the vehicle terminal	19
Figure 2-18: Satellite terminal deployment at a vehicle.....	20
Figure 3-1: Diagram illustrating various terms in relation to satellite orbits [8].....	23
Figure 3-2: Definition of satellite in-plane angles [6]	24
Figure 3-3: QZSS orbit plot in the inertial frame (left) and rotating frame (right).....	28
Figure 3-4: QZSS ground track.....	29
Figure 3-5: QZSS track in local Cartesian (QuaDRiGa) coordinates.....	29
Figure 3-6: Reflector antenna model at 1 GHz and 17 GHz.....	32
Figure 3-7: Cross-polarized (linear $\pm 45^\circ$) panel array antenna model [5].....	33
Figure 3-8: Attenuation by atmospheric gases from Annex 2 in [11]	38
Figure 3-9: Dense urban PL and SF - 3GPP TR 38.811 vs. 5G-ALLSTAR.....	39
Figure 3-10: Urban PL and SF - 3GPP TR 38.811 vs. 5G-ALLSTAR.....	40
Figure 3-11: Suburban PL and SF - 3GPP TR 38.811 vs. 5G-ALLSTAR.....	40
Figure 3-12: Rural PL and SF - 3GPP TR 38.811 vs. 5G-ALLSTAR.....	40
Figure 4-1: Workflow of CloudRT	49
Figure 4-2: Modeling of a bus.....	53
Figure 4-3: Modeling of an SUV	53
Figure 4-4: Tx and Rx antenna pattern for a terrestrial link.....	54

Figure 4-5: Tx and Rx antenna patterns for a satellite link: Satellite antenna pattern (left); Satellite UE antenna pattern (right).	54
Figure 4-6: Seoul urban street model	55
Figure 4-7: Highway model.....	55
Figure 4-8: Traffic light model.....	56
Figure 4-9: Traffic signs model.....	56
Figure 4-10: Rx location at a bus for MN system	56
Figure 4-11: Rx location at an SUV for satellite service	57
Figure 4-12: Received power when the base station is transmitting	61
Figure 4-13: Received power when the satellite is transmitting.....	62
Figure 4-14: RMS delay spread for the urban scenarios.....	63
Figure 4-15: RMS delay spread for the highway scenarios.....	64
Figure 4-16: Rician K -factor for the urban scenarios.....	66
Figure 4-17: Rician K -factor for the highway scenarios.....	67

List of Tables

Table 2-1: Sequence of ITU deliverables for the successive IMT generations	2
Table 2-2: Frequency ranges defined by 3GPP for 5G NR	3
Table 2-3: 3GPP NR FR2 frequency bands.....	3
Table 2-4: 3GPP TR 38.811 (v15.0.0) NTN deployment cases	9
Table 2-5: Set-1 of satellite parameters for system-level simulations	11
Table 2-6: Set-2 of satellite parameters for system-level simulations	12
Table 2-7: KOREASAT-6 specification	13
Table 2-8: Terrestrial simulation assumptions	16
Table 2-9: UE characteristics for system level simulations	17
Table 3-1: Overview of the 5G-ALLSTAR channel model.....	21
Table 3-2: Non-GSO space station parameters (Keplerian elements)	24
Table 3-3: Constants required for orbit prediction	25
Table 3-4: Dependent parameters required for orbit prediction.....	25
Table 3-5: Keplerian elements of QZSS satellite	29
Table 3-6: LOS probability from [3].....	36
Table 3-7: Path-loss parameters	37
Table 3-8: Comparison of NLOS path-loss - 3GPP TR 38.811 vs. 5G-ALLSTAR	37
Table 3-9: Shadow-fading parameters.....	39
Table 3-10: Channel model parameters for dense urban scenario	42
Table 3-11: Channel model parameters for urban scenario	42
Table 3-12: Channel model parameters for suburban scenario	43
Table 3-13: Channel model parameters for rural scenario	43
Table 3-14: Inter-parameter correlations	44
Table 4-1: Locations and heights of each Tx and Rx	53
Table 4-2: Scenario configuration for terrestrial MN system	57
Table 4-3: Scenario configuration for satellite link	58
Table 4-4: Simulation setup.....	58
Table 4-5: EM parameters of different materials	58
Table 4-6: Propagation mechanisms	59
Table 4-7: Considered simulation scenarios	59
Table 4-8: Extracted parameters for the DS	62
Table 4-9: Extracted parameters for the K -factor	65
Table 4-10: Extracted parameters for the angular spreads	68

List of Abbreviations

2D	2 Dimensions / 2-Dimensional
3D	3 Dimensions / 3-Dimensional
3GPP	3 rd Generation Partnership Project
ACF	Autocorrelation Function
API	Advanced Programming Interface
AS	Angle Spread
ASA	Azimuth Spread of Arrival
ASD	Azimuth Spread of Departure
ASI	Adjacent Satellite Interference
BS	Base Station
CCIR	Comité Consultatif International des Radiocommunications
CDFs	Cumulative Distribution Function
CDL	Clustered Delay Line
C-RAN	Cloud Radio Access Network
DL	Downlink
D-RAN	Distributed Radio Access Network
DS	Delay Spread
EIRP	Effective Isotropically Radiated Power
EM	Electromagnetic
eMBB	enhanced Mobile Broadband
EPFD	Equivalent Power Flux Density
ESA	Elevation Spread of Arrival
ESD	Elevation Spread of Departure
FACS	Flexible Access Common Spectrum
FCC	Federal Communications Commission
FDD	Frequency-Division Duplexing
FR2	Frequency Range 2
FS	Fixed Service
FSB	first-bounce scatterer
FSS	Fixed-Satellite service
GEO	Geostationary Orbit
GPS	Global Positioning System
GSO	Geosynchronous Orbit
HAPS	High-Altitude Platform System
KF	Ricean K-Factor
LBS	last-bounce scatterer
LEO	Low-Earth Orbit
LHCP	Left-hand Circular Polarized
LOS	Line-of-sight
LSF	Large-scale fading
LSP	Large-scale parameter
MEO	Medium-Earth Orbit
MN	Moving Network

MNO	Mobile Network Operator
MPC	Multipath Components
MSS	Mobile-Satellite service
MT	Mobile Terminal
NLOS	Non-Line-of-Sight
NR	New-Radio
NTN	Non-Terrestrial Network
O2I	Outdoor to Indoor
OSM	Open Street Map
PC	Personal Computer
PFD	Power flux density
PL	Path-Loss
QoE	Quality of Experience
QZSS	Quasi-Zenith Satellite System
RAN	Radio Access Network
RF	Radio Frequency
RHCP	Right-hand Circular Polarized
RMa	Rural Macrocell
RMS	Root-Mean Square
RT	ray tracing
RU	Radio Unit
Rx	Receiver
S-DAB	satellite digital audio broadcasting
SDL	Supplemental Downlink
SF	shadow-fading
SIR	Signal-to-Interference Ratio
SNO	Satellite Network Operator
STD	Standard Deviation
SUV	Sport Utility Vehicle
TDL	Tapped Delay Line
TR	Technical Report
Tx	Transmitter
UAS	Unmanned Aerial System
UE	User equipment
UL	Uplink
UMa	Urban Macrocell
UMi	Urban Microcell
V2I	Vehicle to Infrastructure
V2V	Vehicle to Vehicle
VSAT	Very Small Aperture Terminal
WGS	World Geodetic System
WRC	World Radio Conference
XPR	Cross-polarization ratio

1 Introduction

In order to evaluate new concepts for a hybrid radio telecommunications network consisting of terrestrial access points that are located on-ground and access points aboard satellites located at altitudes from several hundred kilometers up to 35,786 km at geostationary orbit, this report analyses the spectrum usage and introduces radio propagation models.

This deliverable is the first outcome of work package 3 on spectrum sharing. It builds on the work that has been done in the 3GPP standardization so far and with that, it fits perfectly into the planned standardization activities of the project described in D6.5. The basis for the 5G-ALLSTAR architecture as proposed in D2.2 is considered for the spectrum usage analysis performed in this report. Multi-connectivity enablers as investigated in D4.1 require new concepts for interference analysis and management that are further objectives of WP3 and will be addressed in D3.2 and D3.3.

Within Task 3.1 of WP3, the spectrum usage for cellular and satellite systems has been analyzed by considering deployment scenarios, specifying key parameters and reviewing spectrum bands. The findings are presented in Chapter 2.

Developing a channel model usable for interference analysis of terrestrial and non-terrestrial systems at the same time was the second objective of Task 3.1. For that, two approaches were undertaken, i.e. using a geometry-based stochastic channel model as a basis and using a ray-tracing based channel simulator.

Both approaches required the specification of objectives, the definition of configuration parameters, such as antenna models and the considered scenarios. The model and simulator details are presented in Chapters 3 and 4.

The conclusions, summarizing the key findings, are given in Chapter 5.

2 Spectrum usage analysis

2.1 Spectrum bands

2.1.1 Overall 5G spectrum situation

In many countries, the 5G rollout will be initiated in diverse frequency ranges corresponding to distinct coverage/capacity objectives:

- low frequency bands (around 700 MHz) for large coverage
- mid frequency bands (around 3.5 GHz) for urban coverage/high capacity
- mm-wave range (26 GHz typically) for hot spots/very high capacity

On the medium term, all mobile bands currently used for 4G/LTE will be migrated to 5G/NR. In ITU, two distinct streams of discussion are under way:

- Definition of new interfaces for IMT-2020 (ITU name for 5G).
- Identification of new frequency bands for IMT-2020.

IMT-2020 interfaces definition process

In 2015, the ITU has released its vision document for IMT-2020. This has been followed by the definition of high-level requirements used by bodies such as the 3GPP to issue technical specifications for radio interfaces. The ITU has then defined an evaluation process (under way) to evaluate the proposed interfaces. When the outcome of the evaluation will be effected in 2020, the new interfaces will be published by ITU. The table below shows the sequence of ITU deliverables for 3G/IMT-2000, 4G/IMT-Advanced, 5G/IMT-2020 related to IMT interfaces for both the terrestrial and satellite component of IMT:

Table 2-1: Sequence of ITU deliverables for the successive IMT generations

	IMT-2000		IMT-Advanced		IMT-2020	
	Terrestrial	Satellite	Terrestrial	Satellite	Terrestrial	Satellite
Vision	Rec M.687&M.816 1992	Rec M.818 1994	Rec. M.1645 2003	Rep M.2176 2010	Rec M.2083 2015	?
Requirements	Rec M.1034 1997		Rep M.2134 2008		Rep M.2410 2017	
Submission	8/LCCE/47 1998		Rep M.2133 2008		Rep M.2411 2017	
Evaluation	Rec M.1225 1997		Rep M.2135 2009		Rep M.2412 2017	
Outcome			Rep M.2198 2010	Rep M.2279 2013	Rep M.[IMT-2020.OUTCOME] Expected 2020	
Specifications	Rec M.1457 2000 Last version 2017	Rec M.1850 2000 Last version 2014	Rec M.2012 2012 Last version 2018	Rec. M.2047 2013	Rep M.[IMT-2020.SPECS] Expected 2020	

As regards the satellite component of IMT-2020, no specific deliverable has been developed in ITU, unlike the previous generations 3G and 4G. This is consistent with the vision that satellite access may not be developed in parallel and independently to terrestrial means, but rather could fully be integrated within the IMT-2020 interfaces.

Identification of new bands for IMT-2020

The identification of new frequency bands for 5G is on the agenda of WRC-19 (Agenda Item 1.13). Candidate frequency bands range from 24.25 GHz to 86 GHz. It should be noted that the FSS spectrum 27.5 – 31 GHz is not part of the candidate bands for international identification,

despite the strong push by the mobile industry and certain administrations to identify part or all of the 27.5 – 29.5 GHz range for IMT.

For the purpose of the present study for a satellite access system capable to address smartphones, it is considered that the mmWave bands considered by WRC-19 are technically irrelevant. Hence, WRC-19 decisions have no impact on potential solutions for that market segment.

However, it is considered that satellites will play a role in backhauling and many other aspects of 5G connectivity that will be served by using Ka-band or Q/V-band high throughput satellite systems. This is the reason why the Ka-band in particular should be preserved from an IMT identification by ITU, despite steps taken by certain administrations (US, Japan, Korea in particular) for their own territory.

3GPP NR frequency ranges

The current 3GPP view on frequency bands is provided in Technical Specification TS 38.101, defining the different 5G NR frequency ranges.

Table 2-2: Frequency ranges defined by 3GPP for 5G NR

Frequency range	Corresponding frequency range	NR operating bands
FR1	450 MHz – 6000 MHz	n1 ... n86
FR2	24250 MHz – 52600 MHz	n257, n258, n260, n261

Table 2-3: 3GPP NR FR2 frequency bands

Operating Band	Uplink (UL) operating band BS receive UE transmit			Downlink (DL) operating band BS transmit UE receive			Duplex Mode
	F _{UL_low} – F _{UL_high}			F _{DL_low} – F _{DL_high}			
n257	26500 MHz	–	29500 MHz	26500 MHz	–	29500 MHz	TDD for cell, FDD for Sat
n258	24250 MHz	–	27500 MHz	24250 MHz	–	27500 MHz	TDD
n260	37000 MHz	–	40000 MHz	37000 MHz	–	40000 MHz	TDD
n261	27500 MHz	–	28350 MHz	27500 MHz	–	28350 MHz	TDD

Regulatory and licensing issues of 5G satellite system use in mobile bands

This case corresponds to the reuse of mobile frequency allocations identified for IMT for which no satellite service allocation exist. The interest is to benefit from the user terminal's native capabilities to communicate in those bands. No ITU regulatory framework is available yet for satellite operation in mobile bands. This would require new satellite allocations or substantial changes in existing allocations such as protection criteria (power flux densities limitations) on MSS downlink primary allocation with respect to terrestrial mobile systems operating in adjacent countries. This issue could be addressed at the WRC-23, if decided at the upcoming WRC-19. For this, a support of terrestrial mobile stakeholders would be crucial.

Besides the frequency allocation aspects, another difficulty to cope with is the geographical fragmentation of licenses in some frequency bands. This, from the satellite standpoint, can appear to be a real challenge in terms of satellite antenna implementation, due to the implied need

of isolation performance (i.e., license area scales, especially in Europe, can be quite small with respect to standard satellite beam footprint widths, so neighboring countries isolation may be really challenging). These aspects shall be further assessed on case-by-case basis.

For all of these reasons, satellite systems, when considering their use in terrestrial mobile frequency bands, could be either seem to be most likely positioned on large bandwidth systems with resource allocation flexibility or alternatively and rather targeting the least used bands of MNOs licenses, so that satellite may be used by most operators as a common resource.

2.1.2 Satellite frequency bands potentially eligible for 5G

Four different types of frequency bands are currently eligible for 5G by satellite and could thus be simultaneously used by both, terrestrial and non-terrestrial 5G systems, e.g. L-, S-, C- and Ka-bands.

L-band

This TDD band ranges from 1427 to 1518 MHz. Its use could mainly be foreseen for mobile supplemental downlink (SDL). Power flux density (PFD) limits in the 1452 – 1492 MHz sub-band may result from the WRC-19, which will address mobile communications compatibility conditions with S-DAB (satellite digital audio broadcasting). Currently, according to the ITU, this sub band is allocated to S-DAB for the whole world, except over North America. If such PFD limits are amended in the future, satellite could play a role in complementing terrestrial SDL.

S-band

The MSS S-band is harmonized globally at ITU level in the range 1980-2010 MHz for uplink and 2170-2200 MHz for downlink. In ITU Region 2 (Americas), the bands 2010-2025 MHz for uplink and 2160-2170 MHz for downlink are additionally allocated to MSS. This band provides a certain amount of flexibility for hybrid satellite-terrestrial systems as in Europe and North America (US/Canada). Here, the regulatory framework allows a complementary terrestrial component to satellite systems. In addition, the band is also allocated to terrestrial mobile services. Hence, an administration may decide to authorize either satellite or terrestrial services on its territory, or a combination of both (hybrid satellite + complementary terrestrial component). Echostar (in Europe and North America) and Inmarsat in Europe are the main users of the band as satellite services providers. The band allocation and the band splitting between both operators is illustrated in the figure below.

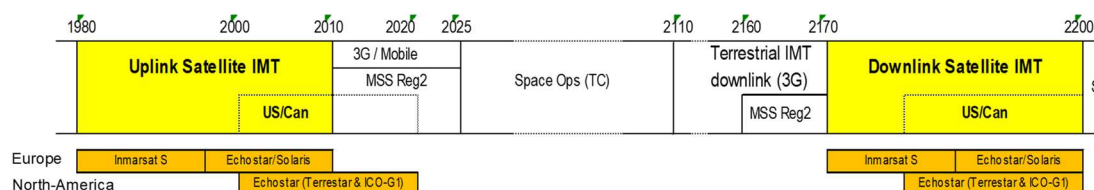


Figure 2-1: S-band MSS allocation to satellite operators

Over Asia, China is known to operate a domestic MSS system in the band. Over other regions (South East Asia and Pacific), priority spectrum rights are held by Omnispace and Helioswire. This company Omnispace operates a MEO satellite (former ICO-F2) and maintains the associated ITU spectrum rights. The coexistence of satellite and terrestrial mobiles in adjacent countries will be addressed at WRC-19 specifically in this MSS S-band. Two cases of interference shall actually be considered:

- Satellite reception interfered by ground UEs and base stations (gNBs in 5G).
- Ground UEs and base stations interfered by the satellite transmitted signals.

Preliminary results of ITU studies tend to show that, under certain deployment assumptions, in most parts of the world, satellite reception should not be impaired by UE transmissions. On the contrary, base station transmissions might reveal themselves incompatible with satellite operation in the same frequency band, even if some US satellite operators claim the contrary. These interference scenarios shall thus be further studied with finer network deployment assumptions in a 5G system context. Building then on consolidated results, the conclusions could be extrapolated to any frequency band in the 1 to 3 GHz range and especially terrestrial mobile frequency bands, where mobile network operators (MNOs) could operate a satellite layer in its licensed bands, provided a compatibility can be confirmed and adequate protection to its co-frequency neighbors is guaranteed. In addition, as part of the S-band range, the band 2483.5-2500 MHz may offer opportunities for combined satellite and terrestrial use, which shall be analyzed.

C-band

The communications C-band was the first frequency band that was allocated for commercial telecommunications via satellites. The satellite communications portion of the C-band is highly associated with television receive-only satellite reception systems, commonly called "big dish" systems, since small receiving antennas are not optimal for C-band systems and typical C-band dishes range from 2.5 to 3.5 meters. Satellite telecommunication networks are also implemented in C-band for corporate and government infrastructure networks. Slight variations in the identification assignments of C-band frequencies for IMT have been approved for use in various parts of the world, depending on their locations in the three ITU radio regions.

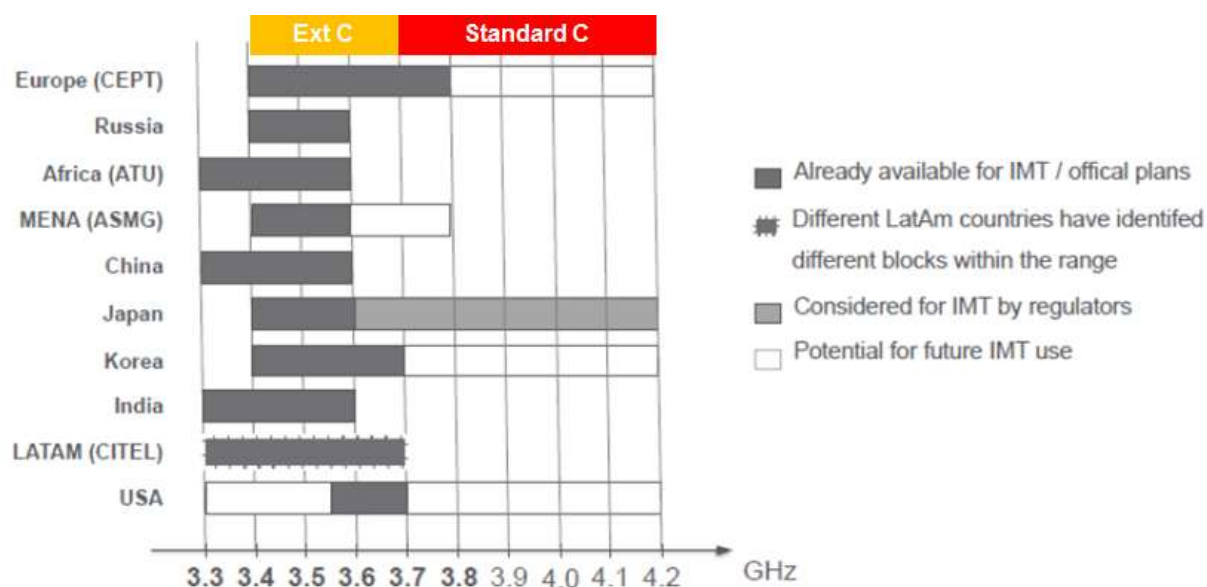


Figure 2-2: Status and plans for the 3.3 – 4.2 GHz range all over the world (source: GSA)

The IMT take up within 3.3 and 4.2 GHz frequency range is continuously increasing. The 3.4 – 3.6 GHz band is now almost globally available and a large number of countries in all regions of the world are taking actions in order to reach 200 – 400 MHz of continuous bandwidth in C-band.

C-band is the largest continuous bandwidth eligible for 5G below 6 GHz but ITU currently sets some limits in power flux densities (PFD) for satellite systems in order to protect terrestrial services. These limitations are too stringent to allow efficient 5G satellite services, but could be potentially exceeded over some countries under adequate agreements. Nonetheless, isolation

of the neighboring countries without the same agreements will drive the satellite's antenna isolation capability, and may require that the current PFD limitations be relaxed for a long-term use of this frequency range. For this, a WRC decision would be needed. On top of this, the use of C-band for 5G satellite systems will be restricted to areas where no C-band GSO System is operating, as their protection cannot be guaranteed with respect to the Equivalent Power Flux Density (EPFD) limitation currently set by the ITU.

The 3.7-4.2 GHz band has been exclusively used for fixed-satellite service (FSS) and fixed service (FS) in the United States. The link for the FSS is directed from the space to the Earth. The FS is used for point-to-point fixed microwave links. In the Notice of Proposed Rulemaking, the FCC proposed to allocate the 3.7-4.2 GHz band to the mobile services in addition to the conventional FSS and FS, as seen in Figure 2-3 [2]. In this situation, co-channel interference as well as adjacent channel interference can occur which may prevent the coexistence of the FSS/FS and mobile service in the same geographic area.

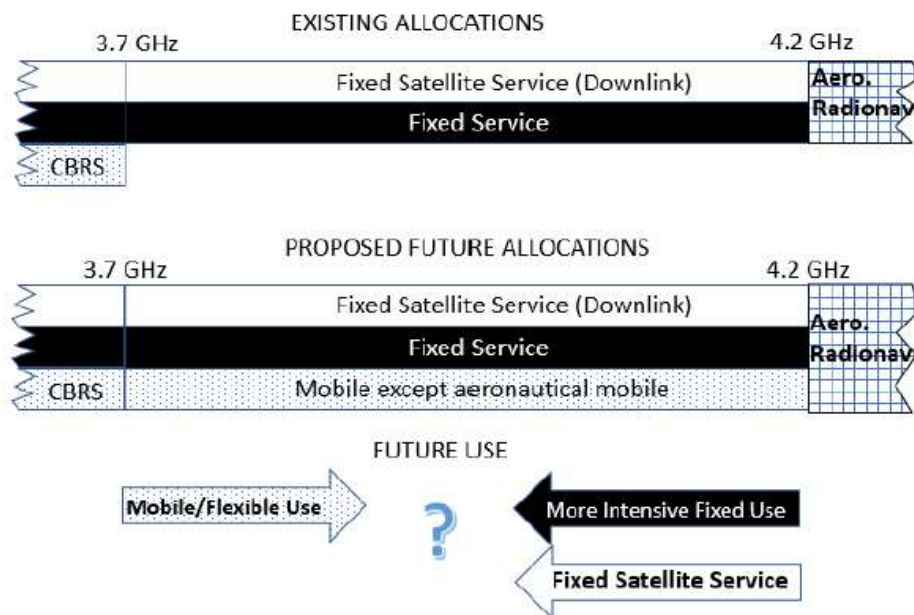


Figure 2-3: Potential allocation of 3.7-4.2 GHz band

FACS band

In Korea, 22-23.6 GHz band was designated as a flexible access common spectrum (FACS) band. In this band, any wireless service is possible while keeping the coexistence rules, as follows:

- Maximum transmit power = 100 mW
- Maximum power spectral density (PSD) = 6 dBm/MHz
- Maximum antenna gain = 16 dBi

The 5G-ALLSTAR project currently considers employing the FACS band for the terrestrial network. There is no identified deployment scenario related to the satellite communication. However, since there is no strict regulation on the use of the FACS band, this band is subject to sharing between different wireless services such as terrestrial and non-terrestrial networks at least for analysis and simulation of spectrum sharing.

Ka-band

Currently, the Ka-band is widely used by satellite networks operators (SNOs) to offer broadband services to their customers. These bands are not only interesting because the available technology is now very mature and cost effective, but also because these spectrum parts are still

less congested than the more traditional satellite C- and Ku-bands, while allowing the use of smaller dishes at ground terminal level. The 24.25 – 27.5 GHz band is the major Ka-band part targeted for 5G in its mmWave frequency range above 6 GHz, but the terrestrial mobile systems community is pushing strongly to impinge on the 27.5 – 29.5 GHz band, which is part of the core satellite Ka-band spectrum. Their main argument to shift their band upward is the need of protection of the passive scientific services at 24 GHz, but the satellite network operators seem to remain strongly opposed to the sharing of their Ka-band spectrum and the band 27.5-29.5 GHz is out of scope of the WRC-19.

The 28 GHz band is one of the main target bands for the mmWave (FR2) operation of the 5G NR specification. Accordingly, some national authorities completed spectrum auctions on the 28 GHz band for the mobile broadband services:

- In June 2018, Korea finished 28 GHz spectrum auctions for terrestrial 5G services. Spectrums with equal bandwidth of 800 MHz were allocated to three major telecom operators: KT (26.5-27.3 GHz), LG U+ (27.3-28.1 GHz), and SKT (28.1-28.9 GHz).
- In January 2019, the United States concluded the 5G 28 GHz spectrum auction. The auction was conducted by the FCC for two 425 MHz bands (27.500-27.925 GHz and 27.925-28.350 GHz) by geographic county.

With adequate coordination, the following fixed satellite services frequency bands could be foreseen for a common use of both MNOs and SNOs, even if no 3GPP specifications are considering these bands for the time being:

- 17.7 – 20.2 GHz for Downlink
- 29.5 – 30 GHz for Uplink

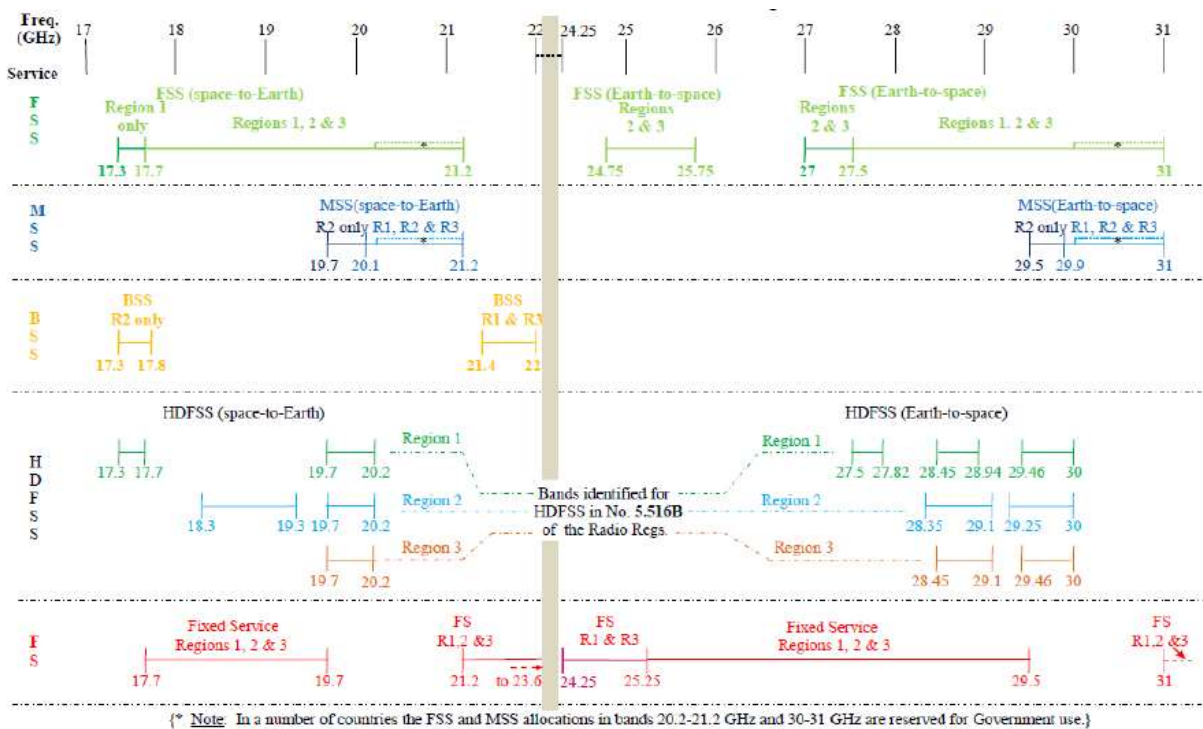


Figure 2-4: FSS, MSS, BSS and FS allocations in Ka-band in the ITU radio regulations – Source: Global VSAT Forum, November 2011

2.2 Non-terrestrial networks deployment scenarios

2.2.1 Deployment scenarios selection

The aim of the 5G-ALLSTAR project simulations is to prove key technical concepts efficiency for enabling user equipment's (UE) to access 5G services through hybrid terrestrial-satellite multi-connectivity. The reference system architecture implementing these solutions was designed in project deliverable D2.2 "Preliminary document of 5G-ALLSTAR architecture, API and interface specifications".

This multi-connectivity architecture, depicted in Figure 2-5, has been conceived to be in line with the current vision of distributed resource control and to maximize the whole user's experience by optimizing the radio performances. In this regard, the 5G-ALLSTAR project proposes to enrich the current entities, i.e., the core network, the cloud radio access network (C-RAN), and the distributed radio access networks (D-RAN), with elements (i.e., advanced functionalities) able to satisfy and control specific end-to-end services or applications by using both traffic flow control and quality of experience (QoE) control.

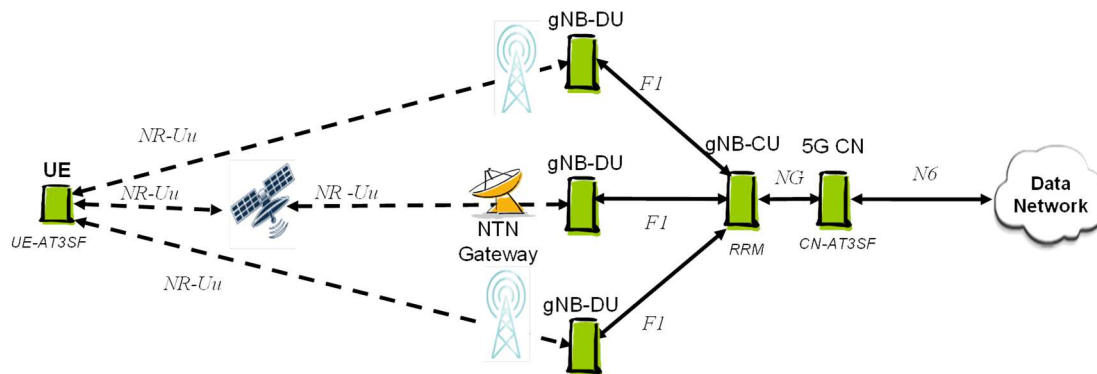


Figure 2-5: 5G-ALLSTAR reference system architecture

The non-terrestrial part in this distributed architecture, consisting of the active satellite and its gateway, can be considered as one of the D-RANs of the network and is managed by the same C-RAN as its terrestrial counterparts. The singularity of the non-terrestrial D-RAN is that, whatever the satellite orbit and its antenna pattern are, the satellite beams will always be much wider than terrestrial cells, so in any case its deployment scenario can be represented as shown in Figure 2-6. 3GPP defines a series of reference scenarios for 5G non-terrestrial networks. Their main features are presented in Table 2-4.

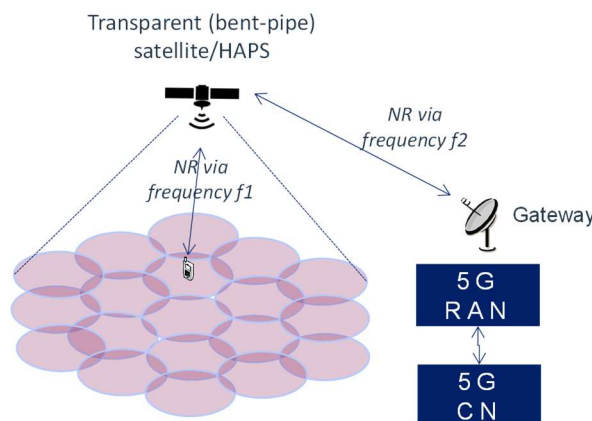


Figure 2-6: Typical non-terrestrial network deployment

Table 2-4: 3GPP TR 38.811 (v15.0.0) NTN deployment cases

Main attributes	Deployment-D1	Deployment-D2	Deployment-D3	Deployment-D4	Deployment-D5
Platform orbit and altitude	GEO at 35 786 km	GEO at 35 786 km	Non-GEO down to 600 km	Non-GEO down to 600 km	UAS between 8 km and 50 km including HAPS
Carrier Frequency on the link between platform and UE	Around 20 GHz for DL Around 30 GHz for UL (Ka-band)	Around 2 GHz for both DL and UL (S-band)	Around 2 GHz for both DL and UL (S-band)	Around 20 GHz for DL Around 30 GHz for UL (Ka-band)	Below and above 6 GHz
Beam pattern	Earth fixed beams	Earth fixed beams	Moving beams	Earth fixed beams	Earth fixed beams
Duplexing	FDD	FDD	FDD	FDD	FDD
Channel Bandwidth (DL + UL)	Up to 2 * 800 MHz	Up to 2 * 20 MHz	Up to 2 * 20MHz	Up to 2 * 800 MHz	Up to 2 * 80 MHz in mobile use and 2 * 1800 MHz in fixed use
NTN architecture options (See clause 4)	A3	A1	A2	A4	A2
NTN Terminal type	Very Small Aperture Terminal (fixed or mounted on Moving Platforms) implementing a relay node	Up to 3GPP class 3 UE [1]	Up to 3GPP class 3 UE [1]	Very Small Aperture Terminal (fixed or mounted on Moving Platforms) implementing a Relay node	Up to 3GPP class 3 UE [1] Also Very Small Aperture Terminal
NTN terminal Distribution	100% Outdoors	100% Outdoors	100% Outdoors	100% Outdoors	Indoor and Outdoor
NTN terminal Speed	up to 1000 km/h (e.g. aircraft)	up to 1000 km/h (e.g. aircraft)	up to 1000 km/h (e.g. aircraft)	up to 1000 km/h (e.g. aircraft)	up to 500 km/h (e.g. high speed trains)
Main rationales	GEO based indirect access via relay node	GEO based direct access	Non-GEO based direct access	Non-GEO based indirect access via relay node	Support of low latency services for 3GPP mobile UEs, both indoors and outdoors
Supported Uses cases, see clause 4	1/ eMBB: multi-connectivity, fixed cell connectivity, mobile cell connectivity, network resilience, Trunking, edge network delivery, Mobile cell hybrid connectivity, Direct To Node multicast/broadcast	1/eMBB: Regional area public safety, Wide area public safety, Direct to mobile broadcast, Wide area IoT service	1/eMBB: Regional area public safety, Wide area public safety, Wide area IoT service	1/ eMBB: multi-homing, fixed cell connectivity, mobile cell connectivity, network resilience, Trunking, Mobile cell hybrid connectivity	1/ eMBB: Hot spot on demand

Not all 3GPP deployment scenarios are relevant for 5G-ALLSTAR. Hence, we will focus on the following 3GPP TR 38.811 scenarios:

- GEO satellite deployment in Ka-band (D1): this deployment scenario will also be considered in WP5, with a channel emulator on the European testbed and a real Ka-band satellite (most likely Athena-Fidus) on the trial platform for displaying the project's achievements.
- LEO satellite deployment in S-band (D3): as it would better complement the first case by addressing the second frequency band and satellite orbit considered in the TR 38.811

5G-ALLSTAR will also consider the following additional scenario, which was not included in the 3GPP NTN deployment scenario but is of significance in understanding spectrum-sharing aspects of 5G-ALLSTAR project:

- GEO satellite deployment in Ku-band, which operates under FDD mode with frequency bands at around 12 GHz for the downlink and around 14 GHz for the uplink.

In the above scenarios, the satellites, LEO or GEO are considered transparent, as fully bent-pipe payload repeaters (analogue or digital), which currently depict the most widely used and ordered solutions by satellite network operators (SNOs). It's thus of a high interest to demonstrate whether such "classical" and cost-effective space segments can, when associated to the appropriate ground segment elements, be efficiently integrated into wider 5G terrestrial networks.

2.2.2 Beam size and service area

Up to 57 terrestrial cells are considered within the satellite beam, depending on simulator performance (processing capacity / available memory on the PC). Terrestrial cells are assumed adjacent to each other. Two distinct cases can be distinguished in the way the satellite beam covers the cluster of terrestrial cells depending on the relative positions of the satellite and the ground area containing the cluster of terrestrial cells. Note that in any case, within the beam footprint (the spot) UEs are under different elevation angles, from 10° to 90° (see UE distribution laws).

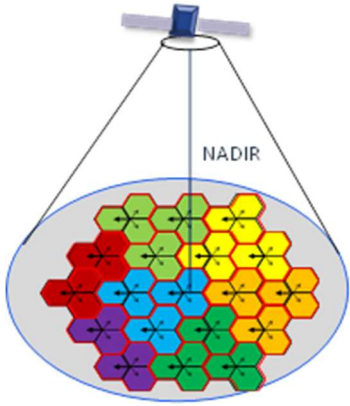
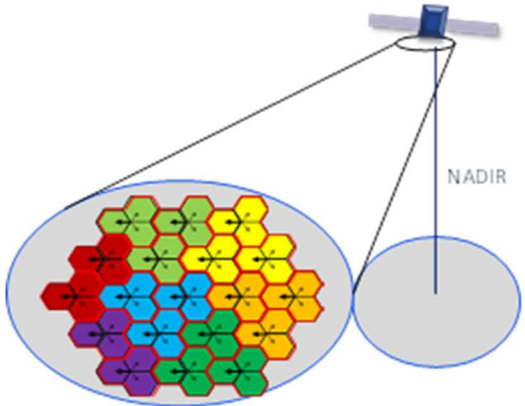
Case 1 : Central beam center is considered at nadir point	Case 2 : Central beam boresight direction computed based on elevation angle target
	
First priority for 5G-ALLSTAR simulations	Lower priority for 5G-ALLSTAR simulations

Figure 2-7: Satellite beam bore sight direction definition

The beam size and service area for the KOREASAT-6 satellite is depicted in Figure 2-8, where the coverage of the GEO satellite is expressed using contour lines. The beam intensity is the

highest at the center and becomes weaker at the beam boundary. The effective service area encompasses the entire landmass of South Korea, having a beam diameter of hundreds of kilometers.

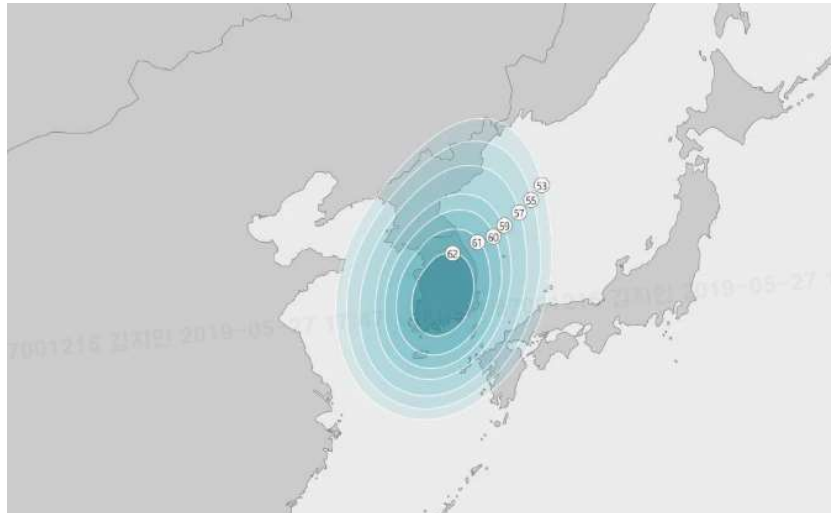


Figure 2-8: KOREASAT-6 satellite coverage map

2.2.3 Space segment parameters

According to the latest 3GPP RAN1 working group meeting on non-terrestrial network integration into 5G systems, the following tables present the two sets of satellite parameters that will be considered for 5G-ALLSTAR system-level simulations:

- Set-1 corresponds to satellites that are foreseen as being the potential standard for “5G-ready” satellites in a near future.
- Set-2 corresponds to standard values that can be encountered on the currently flying and produced telecommunication satellites.

Note: values in grey in both tables below mean that the associated deployment case is not considered on 5G-ALLSTAR.

Table 2-5: Set-1 of satellite parameters for system-level simulations

Satellite orbit		GEO	LEO-600
Satellite altitude		35,786 km	600 km
Payload characteristics for DL transmissions			
Equivalent satellite antenna aperture (Note 1)	S-band (i.e. 2 GHz)	22 m	2 m
Satellite EIRP density		59 dBW/MHz	34 dBW/MHz
Satellite Tx max Gain		51 dBi	30 dBi
Satellite beam diameter (Note 2)		250 km	50 km
Equivalent satellite antenna aperture (Note 1)	Ka-band (i.e. 20 GHz for DL)	5 m	0.5 m
Satellite EIRP density		40 dBW/MHz	4 dBW/MHz
Satellite Tx max Gain		58.5 dBi	38.5 dBi

Satellite beam diameter (Note 2)		110 km	20 km
Payload characteristics for UL transmissions			
Equivalent satellite antenna aperture (Note1)	S-band (i.e. 2 GHz)	22 m	2 m
G/T		19 dB K ⁻¹	1.1 dB K ⁻¹
Satellite Rx max Gain		51 dBi	30 dBi
Equivalent satellite antenna aperture (Note 1)	Ka-band (i.e. 30 GHz for UL)	5 m	0.5 m
G/T		28 dB K ⁻¹	13 dB K ⁻¹
Satellite RX max Gain		62 dBi	42 dBi
Note 1: This value is equivalent to the antenna diameter to be used in Sec. 6.4.1 of TR 38.811.			
Note 2: This beam size refers to the Nadir pointing of the satellite			

Table 2-6: Set-2 of satellite parameters for system-level simulations

Satellite orbit		GEO	LEO-600
Satellite altitude		35,786 km	600 km
Payload characteristics for DL transmissions			
Equivalent satellite antenna aperture (Note 1)	S-band (i.e. 2 GHz)	12 m	1 m
Satellite EIRP density		53.5 dBW/MHz	28 dBW/MHz
Satellite Tx max Gain		45.5 dBi	24 dBi
Satellite beam diameter (Note 2)		450 km	90 km
Equivalent satellite antenna aperture (Note 1)	Ka-band (i.e. 20 GHz for DL)	2 m	0.2 m
Satellite EIRP density		32 dBW/MHz	-4 dBW/MHz
Satellite Tx max Gain		50.5 dBi	30.5 dBi
Satellite beam diameter (Note 2)		280 km	50 km
Payload characteristics for UL transmissions			
Equivalent satellite antenna aperture (Note 1)	S-band (i.e. 2 GHz)	12 m	1 m
G/T		14 dB K ⁻¹	-4.9 dB K ⁻¹
Satellite Rx max Gain		45.5 dBi	24 dBi
Equivalent satellite antenna aperture (Note1)	Ka-band (i.e. 30 GHz for UL)	2 m	0.2 m
G/T		20 dB K ⁻¹	5 dB K ⁻¹
Satellite Rx max Gain		54 dBi	34 dBi
Note 1: This value is equivalent to the antenna diameter to be used in Sec. 6.4.1 of TR 38.811.			
Note 2: This beam size refers to the Nadir pointing of the satellite			

In addition, a set of parameters for the KOREASAT-6 satellite is described in Table 2-7, which will also be used for the spectrum sharing analysis and simulations. For providing data traffics from a satellite towards a UE aboard a moving vehicle, we use the KOREASAT-6, which is

equipped with Ku-band communication transponders on a geostationary orbit. KOREASAT-6 has 24 FSS Ku-band transponders and 6 BSS Ku-band transponders. The satellite generates 3.4 kilowatts of payload power and has a 15-year in-orbit mission life.

Table 2-7: KOREASAT-6 specification

Satellite Orbit / Altitude	GEO / 35,786 km
Number of Transponders	FSS : 24x36MHz / BSS : 6x27MHz
Uplink/Downlink Frequencies (GHz)	14.0 – 14.5 / 12.25 – 12.75 14.5 – 14.8 / 11.7 – 12.0
Polarization	Linear (Horizontal or Vertical)
Peak EIRP (dBW)	62
G/T (dB/K)	12-20
Orbital Location (Longitude)	116°E
Geographic Coverage	Korea
Equivalent satellite antenna aperture	2.3 m

2.2.4 Gateway

Only service links (between UEs and the satellite) will be considered for simulations as they are driving the end-to-end links performances in both, forward and return ways. Indeed, feeder links (between the gateway and the satellite) are using dedicated frequencies where the isolation from potential source of interference is guaranteed. Moreover, the very large dishes that are usually used at gateway level, lead to much better link budget performances as compared to the service links. In the latter case, common UE antennas lead to poorer performances and a worse interference environment especially considering frequency sharing. Hence, gateway parameters and settings are not needed in this document.

2.3 Terrestrial networks deployment scenarios

2.3.1 Candidate scenarios

For the terrestrial network deployment, the main service target considers vehicles connected both or either to the terrestrial network and/or non-terrestrial network. The reason for focusing on vehicle-type terminals is that vehicles typically have enough space to deploy satellite antenna and modem devices with large form factors.

There are two main deployment scenarios for vehicle communication: highway and urban grid. As seen in Figure 2-9, in the highway scenario, cars are driving with high speed, e.g., up to 140 km/h. In addition, the movements of vehicles tend to be straight lines along the highway. The LOS probability is quite high since obstacles between the base station and the vehicle are rare except of other vehicles. In non-LoS situations, relaying through other vehicle can be supported via V2V links between vehicles. It should be noted that the Doppler Effect and frequent handovers are probably significant given the high vehicle speeds.

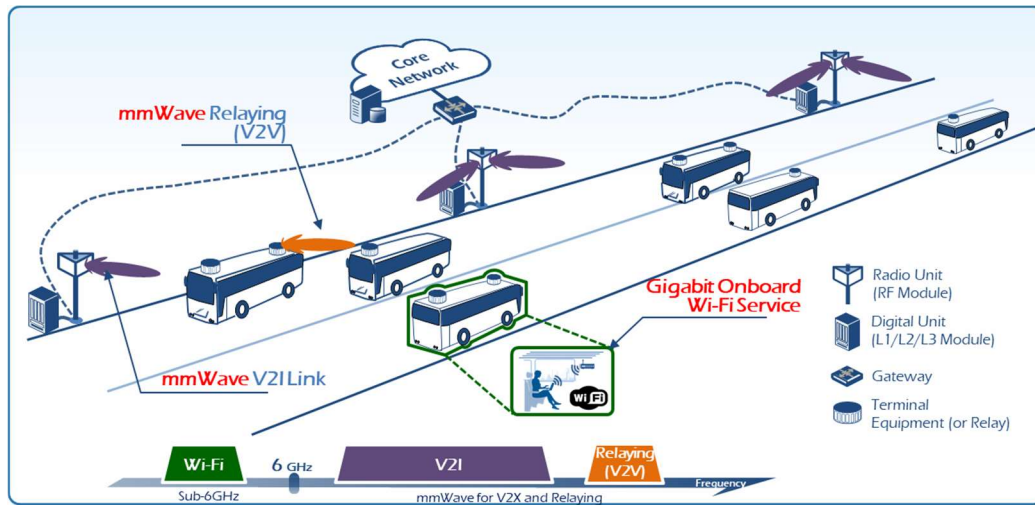


Figure 2-9: Highway deployment scenario

The urban grid scenario is depicted in Figure 2-10, where the speed of cars is not that high, e.g., 70 km/h, reducing the Doppler Effect. However, the LoS probability is much lower than in the highway scenario. The reason is the increased vehicle density on the road and the existence of fixed obstacles such as buildings, traffic lights, traffic signs, trees, and so on. The vehicles tend to move with less consistency, e.g. cars can turn at a street crossing or stop temporarily within a short distance.

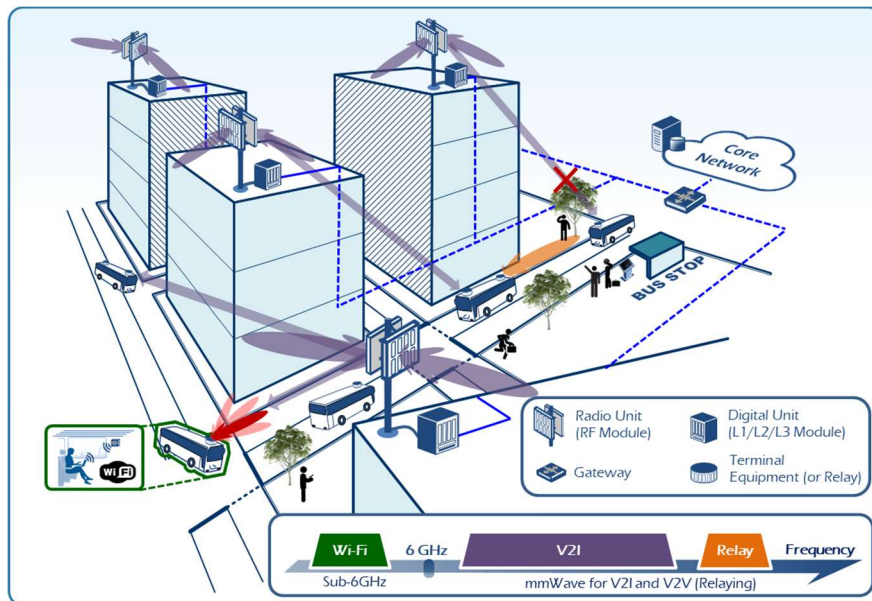


Figure 2-10: Urban grid deployment scenario

2.3.2 Radio unit deployment

RUs can be deployed along the road with a certain inter-RU distance (e.g., 500 m) between the RUs. A beamforming technique can be employed to generate a narrow beam along the road in order to provide a coverage to the vehicles on the road while reducing interference to other devices outside the road. Having a fixed beam along the road is sufficient to have enough coverage. As seen in Figure 2-11, there can be two alternatives regarding the location of the RU: beside a road and in the middle of a road. The RU location determination can be made considering practical site-dependent factors such as cell planning, optic fiber and power availability, and traffic/road regulations, and so on.

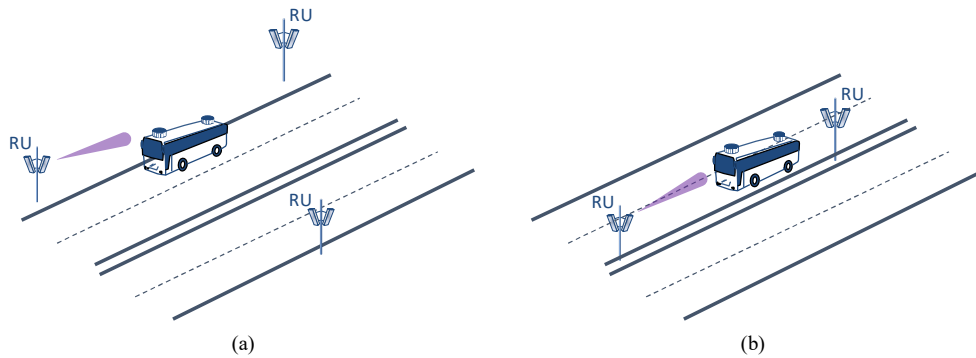


Figure 2-11: RU location at a road: a) beside a road; b) middle of a road

There are also two alternatives regarding the location of the RU at an intersection: RU at the corner of the intersection and RU at the center of the intersection, as depicted in Figure 2-12.

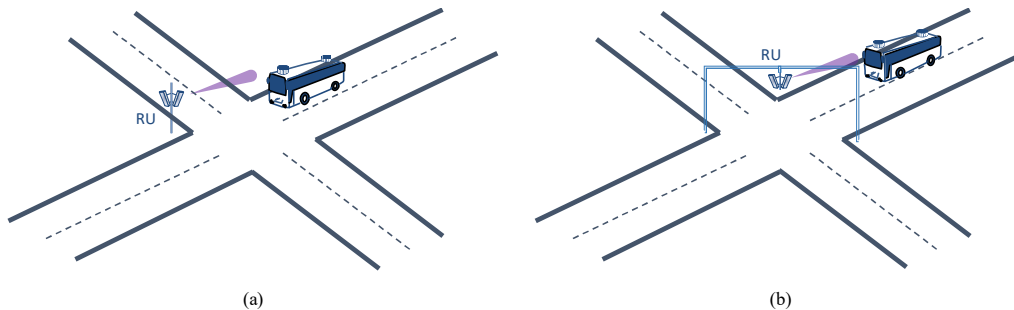


Figure 2-12: RU location at an intersection: a) corner of an intersection; b) center of an intersection

2.3.3 RF and antenna characteristics

In each RU, there will be two slotted waveguide array antennas with orthogonal polarizations each (e.g., vertically and horizontally linear polarizations). Each slotted waveguide antenna consists of 4x4 radiating elements and generates a beam with an array gain of around 19 dBi. As mentioned previously, fixed beamforming is used at the RU. The maximum RF output power is 17 dBm. Hence, the isotropically radiated power (EIRP) is 36 dBm. The beam radiation pattern of each array antenna is illustrated in Figure 2-13. The half-power beamwidth is around 18°.

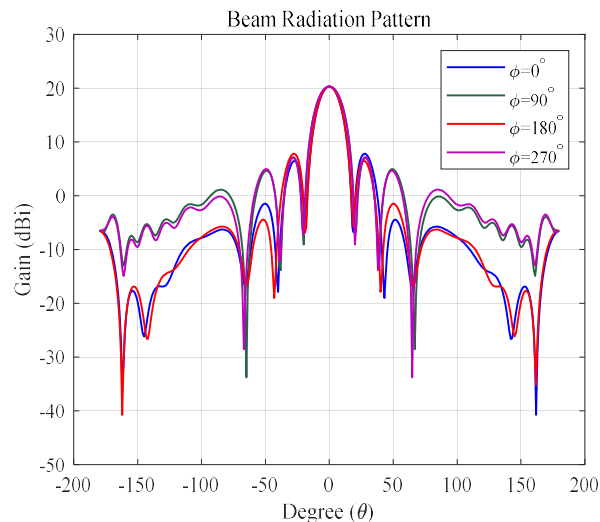


Figure 2-13: Beam radiation pattern of each array antenna

As depicted in Figure 2-14, the frequency band for the terrestrial network is 22-23.6 GHz, where some portion of the band is utilized for the V2I connectivity between the vehicle and RU and the other portion is utilized for the V2V connectivity between the vehicles for the relaying purposes.

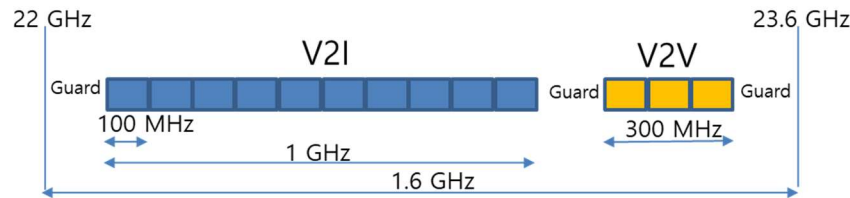


Figure 2-14: Frequency usage plan for terrestrial network

2.3.4 Terrestrial network model

The aim of the 5G-ALLSTAR channel model, besides implementing a radio propagation model for LEO and GEO satellites, is to support coexistence simulations between terrestrial and satellite systems. This is especially important for the 5G era, where the Ka-band (26.5 – 40 GHz) might be partially used by terrestrial mobile radio communication systems. Hence, it is important to study the impact that the terrestrial usage of this band has on the satellite systems and vice-versa. A comprehensive model for terrestrial communication channels has been provided by TR 38.901 “Study on channel model for frequencies from 0.5 to 100 GHz”. These modelling components are listed in Table 3-1. The common simulation assumptions are given by TR 38.901 and are summarized in Table 2-8.

Table 2-8: Terrestrial simulation assumptions

Parameters	UMi - street canyon	UMa	RMa
Cell layout	Hexagonal grid, 19 sites, 3 sectors per site		
Inter-site distance	200 m	500 m	1732 m or 5000 m
BS antenna height	10 m	25 m	35 m
Indoor MT ratio	80%	80%	50% indoor, 50% in car
MT mobility	3 km/h	3 km/h	3 km/h indoor, 50 km/h car
Carrier frequency	6 GHz, 30 GHz, 60GHz, 70GHz		max. 7 GHz
Bandwidth	20 MHz for 6 GHz, and 100 MHz for 30, 60 and 70 GHz		20 MHz
BS Tx power	44 dBm @ 6GHz, 35 dBm @ 30, 60, 70 GHz	49 dBm @ 6GHz, 35 dBm @ 30, 60, 70 GHz	49 dBm
BS antenna	see sec. 3.4.2		
MT antenna	Isotropic	Isotropic	Isotropic

The rationale behind the cell layout is the impact of the inter-cell interference. Terrestrial communication systems are inherently interference limited due to the isotropic antenna patterns at the MT. For this reason, beamforming techniques (either by tilted BS antennas or by precoding techniques at the BS) are used to minimize the interference caused by other BSs in the radio link. To capture and evaluate the impact of the interference, a cell layout consisting of a hexagonal grid with 19 sites is chosen. This is illustrated in Figure 2-15 for a typical urban-microcell (UMi) simulation. 18 BSs (red cross) are placed in 2 rings around a central BS (left subfigure). The MTs are placed only within the central area, which is covered by the first ring of BSs. The outer ring provides a realistic interference scenario. The BSs are at a height of 10 m above the street level (typical assumption for UMi). 80% of the MTs are indoors in buildings with up to eight stories (side view in the central subfigure).

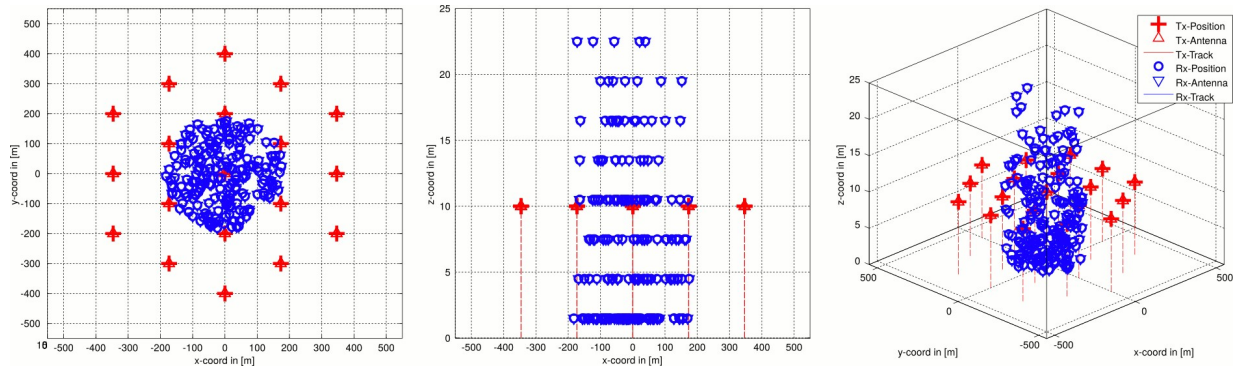


Figure 2-15: Terrestrial network UMi deployment example

When operating a satellite network at Ka-band (26.5 – 40 GHz) or in the S-band (2 – 4 GHz), the satellites might cause interference at the terrestrial BSs, thus decreasing the signal-to-interference ratio (SIR) in the uplink from the MT to the BS or they might cause interference directly at the MT. However, it is more likely that the terrestrial network will cause some significant interference to the (much weaker) signals from the satellite link. An interference analysis will be provided by D3.2 of the 5G-ALLSTAR project.

2.4 Terminal deployment scenarios

2.4.1 Terminal types

According to 3GPP RAN1, three terminal types are considered as reference for system-level simulations.

Table 2-9: UE characteristics for system level simulations

Characteristics	Fixed	Handheld	Vehicular
TR 38.811 deployment case	D1	D3	D1
Frequency band	Ka-band(i.e. 30 GHz UL and 20 GHz DL)	S-band (i.e. 2 GHz)	Ka-band(i.e. 30 GHz UL and 20 GHz DL)
Antenna type and configuration	Directional Section 6.4.1 of TR 38.811 with 60 cm equivalent aperture diameter	Dual-polarized omni-directional antenna elements	Directional (M,N,P,Mg,Ng) = (4,8,2,1,1); (dV,dH) = (0.5, 0.5) λ with directional antenna element (HPBW=65 deg)
Polarisation	Circular	Linear : +/-45°X-pol	Linear : +/-45°X-pol
Rx Antenna gain	39.7 dBi	0 dBi per element	8 dBi per element
Antenna temperature	150 K	290 K	290 K
Noise figure	1.2 dB	7 dB	9 dB
Tx transmit power	2 W (33 dBm)	200 mW (23 dBm)	20 W (43 dBm)
Tx antenna gain	43.2 dBi	0 dBi per element	8 dBi per element

2.4.2 Terminal distribution and movement

Fixed and handheld terminals

Handheld terminals, as well as fixed terminals, are considered not moving. At least three UEs of these types will be assumed in each terrestrial cell and therefore simultaneously under a satellite beam. Different distributions can be considered for example a uniform distribution. Indeed, the elevation angle is important to compute the slant range, the propagation delay and the different propagation loss (Path Loss, Shadows fading, Atmospheric absorption). Depending on intermediate simulation results and 5G-ALLSTAR project progress, some more specific distributions may be further defined.

Vehicular terminals

Two types of mobile terminals are considered in 5G-ALLSTAR

- High speed trains (up to 500 km/h) bridging cities along railways and crossing country where terrestrial coverage may be poor or even not available in some, so called “white spots”. This case is rather considered by the European partners of the consortium. For this kind of terminal, it can be assumed that, over a simulation window, only one is crossing the service area at a time.
- Urban busses in dense urban environment facing fast fading and screening effects due to the proximity of buildings. This case is rather considered by the Korean partners of the consortium.

Terminals traffic profiles

5G-ALLSTAR simulations will allow to study how the multi-access management entities of the network behave when traffic variations occur among the different cells, including the satellite beam, which can also be considered as a cell to some extent. These variations may have different origins:

- the movement of the UEs,
- the movement of the satellite, when LEO is considered,
- the evolution of each UE traffic need over time.

2.4.3 Vehicular terminal details

In a vehicle, a terrestrial terminal (including modem, RF, antenna, etc.) and a satellite terminal are independently equipped, while some higher layer functionalities are able to interact to both transceivers. So, the specification of both terminals are described separately in the following.

Terrestrial terminal specification

At the terrestrial terminal, beam switching functionality is supported as seen in Figure 2-16. At the vehicle, one of three beams can be selected and each beam can be generated with different beam directions. Since the half-power beamwidth of each beam is 18° , the covered area considering the three beams is around 54° . This is particularly advantageous to maintain connectivity when the vehicle direction changes due to the events such as changing lanes, turning at an intersection.

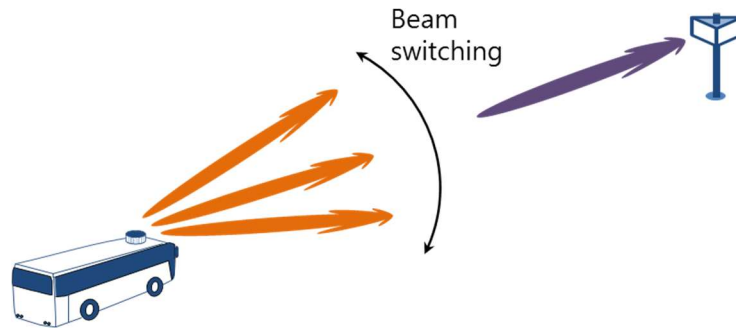


Figure 2-16: Beam switching functionality at a vehicular terminal

The other RF and antenna parameters are similar to the RU counterparts. Each beamforming array antenna consists of 4x4 elements. The EIRP of each array antenna is 36 dBm. The RF and antenna structure of the vehicle terminal is depicted in Figure 2-17.

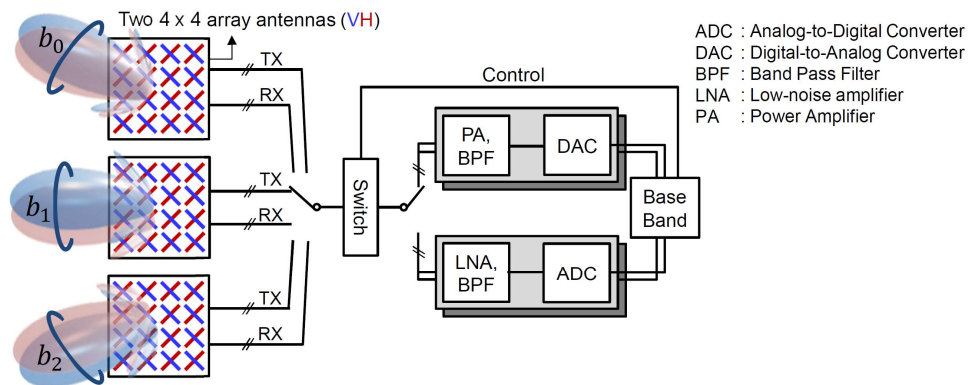


Figure 2-17: RF and antenna structure of the vehicle terminal

Satellite terminal specification

For connecting a UE on a moving vehicle via KOREASAT-6, we operate the flat panel array antenna, which is one of the latest mobile satellite terminals in the satellite industry. One of key features is that flat panel arrays consist of a single physical phased array to transmit and receive the RF signal.

Table 2-7: Satellite terminal antenna specification

Frequency Band	Ku-band
Antenna Type	Electronically scanned array
Polarization	Vertical and horizontal software defined
Rx Frequency Range	11.4 – 12.4 GHz
Rx Gain	33.0 dB
Rx G/T	9.5 dB/K
Tx Frequency Range	14.0 – 14.5 GHz
Tx Gain	32.5 dB

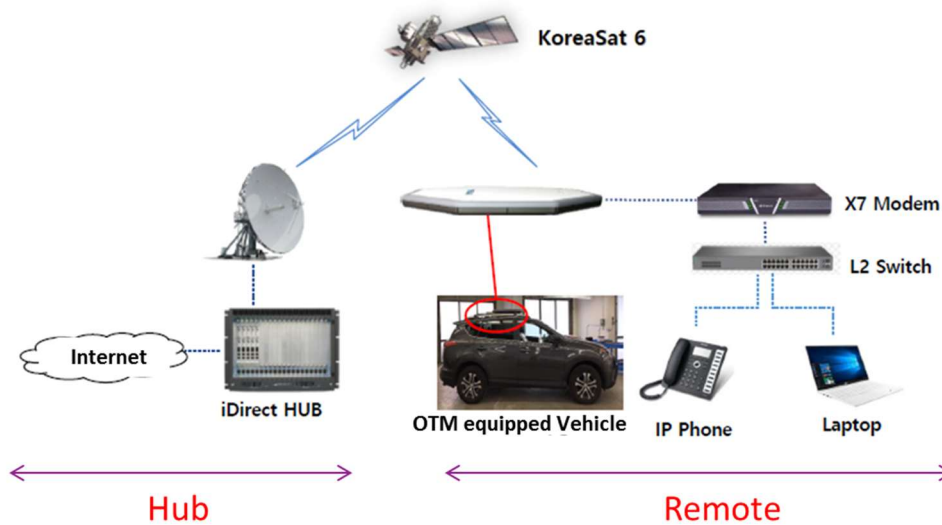


Figure 2-18: Satellite terminal deployment at a vehicle

2.5 Parameters to characterize

5G-ALLSTAR aims in particular at implementing radio-resource management techniques that will allow non-terrestrial and terrestrial networks to operate simultaneously within the same frequency bands. The non-terrestrial beams will be considered as additional cells in the terrestrial network and share the same time and frequency resources as its terrestrial counterparts (base stations). This resource management will be based on techniques that will try to mitigate at best the different types of interferences resulting from this sharing:

- On UE side:
 - Satellite transmissions on downlink will interfere with terrestrial base station transmissions.
 - In case of a constellation of satellites using the same frequency bands, the UE may also encounter some adjacent satellite interference (ASI).
- On the terrestrial base station side:
 - Satellite transmissions will interfere with all the terrestrial base stations almost equally, which differs from a terrestrial-only system in which the distance between base stations contributes to the interference isolation between them.
- On the satellite side (and subsequently on the non-terrestrial base station side):
 - The satellite will receive all transmissions between terrestrial base stations and UEs inside the satellite's beam, which will potentially cause interference. Some will be coordinated, when part of the same system, but some may be uncoordinated when the satellite beam covers also ground areas where other terrestrial networks are deployed (i.e., in neighboring countries).

3 Geometry-based stochastic channel model for cellular and satellite systems

3.1 Modelling objectives

The 5G-ALLSTAR channel model is based on 3GPP TR 38.811 v15.0.0 [3]. The work in 5G-ALLSTAR aims at providing an implementation and further extensions of this channel model within the QuaDRiGa channel simulator [4]. Only the satellite part of 3GPP TR 38.811 is considered here, whereas 3GPP considers also high-altitude platforms. Hence, only outdoor conditions are considered, since performance requirements are not expected to meet the available link budget for indoor communications. Besides the satellite channel model, 5G-ALLSTAR leverages all existing features of the QuaDRiGa channel simulator and the channel model for terrestrial communication systems specified in 3GPP TR 38.901 v15.0.0 (2018-06) [5]. A list of modelling objectives in comparison with the 3GPP model is given in Table 3-1.

Table 3-1: Overview of the 5G-ALLSTAR channel model

Feature	3GPP TR 38.811 v15.0.0	3GPP TR 38.901 v15.0.0	5G-ALLSTAR QuaDRiGa v2.4
Supported scenarios	Satellite and HAPS model for dense urban, urban, sub-urban and rural scenarios	Terrestrial model for urban macrocell (UMa), urban microcell street canyon (UMi), rural macrocell (RMa) and indoor office (InH)	Supports various scenarios, including those from TR 38.811 and TR 38.901
Frequency range	S-band (2 – 4 GHz) Ka-band (26.5 – 40 GHz)	Scalable from 0.5 – 100 GHz	Satellite model scalable from 2 – 40 GHz, terrestrial model scalable from 0.5 – 100 GHz
Simultaneous multi-frequency Simulations	Not supported, single-frequency simulations only	Supported as optional feature, partially incompatible with other model components, see TR 38.901 sec. 7.6.5, pp. 58	Support for simultaneous multi-frequency simulations including terrestrial base stations and satellites, fully compatible with all other model components
Channel observation time	Only Doppler-shift, no update of statistical channel parameters within a communication link	Only Doppler-shift, no update of statistical channel parameters within a communication link	Satellite links observable for up to 30 seconds, including deterministic orbit tracking and multipath tracking; terrestrial links have unlimited observation time
Coordinate system	Simplified approach, “Earth centered Earth fixed” coordinate system, see TR 38.811 sec. 6.3, pp. 45	Metric local Cartesian coordinates, spherical coordinates for angles and antenna patterns, see TR 38.901 sec. 7.1, pp. 14	Supports orbit tracking of LEO satellites in accordance with ITU-R S.1503-3 [6], transformation into local Cartesian coordinates in order to support coexistence studies between terrestrial and satellite systems
Antenna modelling	Model for reflector antennas at the satellite and 3 UE antenna models, see TR 38.811 sec. 6.4, pp. 45	Rectangular panel array antenna, see TR 38.901 sec. 7.3, pp. 22	Reflector antennas and beam-steering antennas, support for wide range of antenna types, see sec. 3.4
Drop-based system-level simulations	See TR 38.811 sec. 6.5.1, pp. 46	Supported by default	Supported by default

Feature	3GPP TR 38.811 v15.0.0	3GPP TR 38.901 v15.0.0	5G-ALLSTAR QuaDRiGa v2.4
Link-level simulations based on TDLs and CDLs	See TR 38.811 sec. 6.9, pp. 81	See TR 38.901 sec. 7.7, pp. 64	Not in scope
LOS probability model	Based on satellite elevation only, see TR 38.811 sec. 6.6.1, pp. 47	Based on BS-MT distance, see TR 38.901 sec. 7.4.2, pp. 27; optional spatial consistency model, see TR 38.901 sec. 7.6.3, pp. 46	Based on satellite elevation or BS-MT distance, support for spatial consistency based on MT and satellite positions, see sec. 3.5.1
Path loss and Shadow fading	Model for distance and frequency-dependence, attenuation due to atmospheric gases, attenuation due to either ionospheric or tropospheric scintillation, building entry loss, shadow fading for selected frequencies, see TR 38.811 sec. 6.6.2, pp. 48	Model for distance, frequency, and height-dependence, see TR 38.901 sec. 7.4, pp. 24	Model for distance and frequency-dependence, attenuation due to atmospheric gases, shadow fading scalable for whole frequency range from 2 – 40 GHz, see sec. 3.5
O2I penetration loss	Defined for airborne vehicle up to 20 km height, see TR 38.811 sec. 6.6.3, pp. 50	Defined for buildings and cars, see TR 38.901 sec. 7.4.2, pp. 27	Supported for terrestrial links; optional for satellite links (same as in TR 38.811)
ITU two-state model for flat fading	See TR 38.811 sec. 6.7.1, pp. 57	Not in scope	Not in scope, flat fading channels are a special case of multipath fading and therefore not treated differently
Frequency selective fading	See TR 38.811 sec. 6.7.2, pp. 59	Supported by default	Supported by default, see sec. [7]
Spatial Consistency	Not supported	Supported as optional feature, partially incompatible with other model components, see TR 38.901 sec. 7.6.3, pp. 46	Supported, see [4]
Dual-Mobility	Not supported	Not supported	Supported, see [4]

3.2 Coordinate systems

The QuaDRiGa channel model [4], which forms the baseline of the 5G-ALLSTAR channel model, uses a local Cartesian metric coordinate system. The positive x-axis points eastwards and the positive y-axis points north. The positive z-axis point upwards. Hence, when considering the whole planet Earth, the local QuaDRiGa coordinate system is defined by a tangential plane with respect to a reference position on Earth (given by its longitude and latitude coordinates). The curvature of the Earth is not considered in QuaDRiGa. Hence, MTs can only be placed within a relatively confined area where the Earth's curvature can be neglected (roughly 20 km diameter). This limitation does not apply to the satellites, which can be placed at any orbital position. The transformation from a global orbit model to local Cartesian coordinates is described in sec. 3.3.

In addition to the absolute positions of mobile transceivers (BSs, satellites or MTs), each device has an orientation with respect to the origin of the local Cartesian coordinates. The orientation is defined by three angles:

- The first value describes the "*bank angle*", i.e. the orientation around an axis drawn through the body of the vehicle (e.g. the satellite) from tail to nose in the normal direction of movement. Positive rotation is clockwise (seen from a pilot/drivers perspective).
- The second value describes the "*tilt angle*", i.e. the vertical angle relative to the horizontal plane; positive values point upwards.
- The third value describes the bearing or "*heading angle*", in mathematic sense. Heading is used to describe the direction an object is pointing. In contrast, the course angle refers to the direction an object is actually moving. East corresponds to 0, and the angles increase counter-clockwise, so North is 90 degrees, South is -90 degrees, and West is 180 degrees.

Note that by default (bank = 0°, tilt = 0°, heading = 0°), QuaDRiGa devices face eastwards and the "nose" points to the horizon.

3.3 Non-GSO satellite orbit model

The satellite orbit description is based on the ITU Recommendation ITU-R S.1503-3 (01/2018) "Functional description to be used in developing software tools for determining conformity of non-geostationary-satellite orbit fixed-satellite service systems or networks with limits contained in Article 22 of the Radio Regulations". [6]

The force of the Earth attraction is the main factor to define a satellite orbital motion. Additional factors include:

- orbit variations due to the Earth's oblateness and its mass distribution irregularities
- solar and lunar attraction
- medium atmospheric drag for satellites in low orbits
- solar radiation pressure, etc.

Orbit perturbations are considered to be only due to the Earth's oblateness. This is motivated by the fact that other factors have a significantly smaller effect. The Earth's oblateness causes secular and periodic perturbations of ascending node longitude and orbit perigee argument. The orbits of some repeating ground tracks can be very sensitive to the exact orbit model.

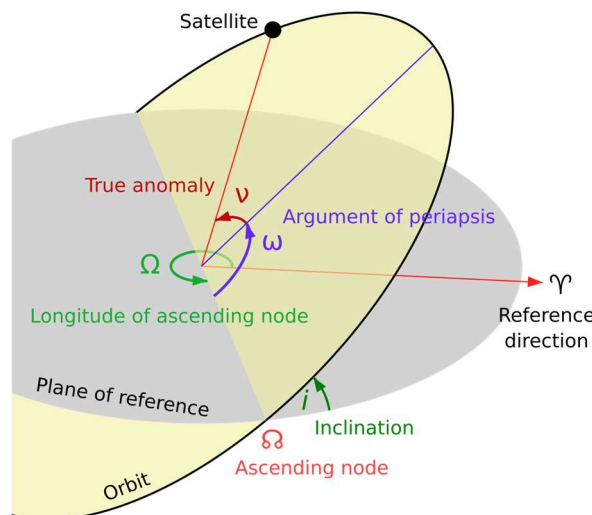


Figure 3-1: Diagram illustrating various terms in relation to satellite orbits [8]

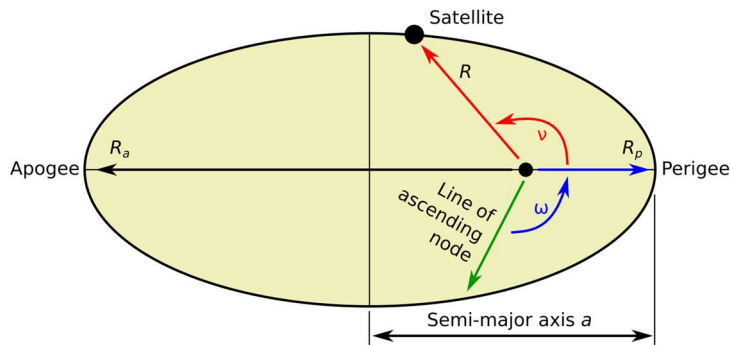


Figure 3-2: Definition of satellite in-plane angles [6]

For each of the non-GSO satellites, the following parameters (Keplerian elements) define the constellation at the start of the simulation (or at a given reference time, the “epoch”).

Table 3-2: Non-GSO space station parameters (Keplerian elements)

Parameter	Notation	Description	Unit
Semi major axis	a	The semi major axis is equal to the sum of the periapsis distance R_p and apoapsis distances R_a divided by two. For circular orbits, the semi major axis is the distance between the centers of the bodies, not the distance of the bodies from the center of mass.	km
Eccentricity	e	The orbital eccentricity of a satellite is the parameter that determines the amount by which its orbit around the Earth deviates from a perfect circle. An eccentricity of 0 yields a circular orbit, $0 < \text{eccentricity} < 1$ yields an elliptical orbit.	-
Inclination	i	The inclination measures the tilt of a satellites orbit around the earth. It is expressed as the angle between Earths equatorial plane and the orbital plane or axis of direction of the satellite.	deg
Longitude of the ascending node	Ω_0	Horizontally orients the ascending node of the ellipse (where the orbit passes upward through the equatorial plane) with respect to the reference frame’s vernal point. As the orbit is fixed in inertial space while the Earth rotates, a time reference for which this angle is valid must be given. This is either the start of the simulation or a given “epoch”.	deg
Argument of periapsis	ω_0	Defines the orientation of the ellipse in the orbital plane, as an angle measured from the ascending node to the periapsis (the closest point the satellite comes to the Earth).	deg
True anomaly	ν_0	Defines the position of the satellite along the ellipse at the start of the simulation or a given “epoch”.	deg

Given these orbital elements, standard orbit mechanics can be used to predict the position of the satellite at future times. However, there are minor launch errors and orbit perturbations that would make the orbit drift unless station keeping was used to ensure the ground track repeats. An important aspect to station keeping is to simulate multiple passes of the non-GSO satellite through an earth station’s main beam with slightly different crossing directions. As changing the position within the orbital plane does not affect this, the main parameter to vary is the longitude of the ascending node. The following Table 3-3 lists the constants and their values used for the orbital calculations. Table 3-4 then lists the parameters that are derived from the orbital elements. The last three parameters \bar{n} , Ω_r , and ω_r describe the orbit drift due to the Earth’s oblateness.

Table 3-3: Constants required for orbit prediction

Parameter	Notation	Value	Unit
Radius of the Earth	R_e	6378.137	km
Radius of geostationary orbit	R_{geo}	42164.1964	km
Gravitational constant	μ	$6.67408 \cdot 10^{-20}$	$\text{km}^3 / \text{s}^2 / \text{kg}$
Mass of Earth	M_e	$5.9722 \cdot 10^{24}$	kg
Speed of light	c	$2.99792458 \cdot 10^5$	km / s
Angular rate of rotation of the Earth	ω_e	$4.17807462185047 \cdot 10^3$	degree / s
Earth rotation period	T_e	86164.09054	seconds
Factor of the Earth non-sphericity	J_2	0.001082636	-

Table 3-4: Dependent parameters required for orbit prediction

Parameter	Notation	Formula	Unit
Distance from the centre of the Earth to the satellite at apogee	R_a	$a = (R_a + R_p)/2$	km
Distance from the centre of the Earth to the satellite at perigee.	R_p	$e = (R_a - R_p)/(R_a + R_p)$	km
Focal parameter	p	$p = a \cdot (1 - e^2)$	km
Mean anomaly at simulation start	M_0	$M_0 = E_0 - e \cdot \sin E_0$	degree
Eccentric anomaly at simulation start	E_0		
Orbital period	T	$T = 2\pi \cdot \sqrt{\frac{a^3}{\mu \cdot M_e}} \approx \frac{360}{\Omega_r + \bar{n}}$	seconds
Mean angular motion	n_0	$n_0 = \frac{180}{\pi} \cdot \sqrt{\frac{\mu \cdot M_e}{a^3}}$	degrees / s
Line of nodes	\bar{n}	$\bar{n} = n_0 \left(1 + \frac{3J_2 R_e^2}{2p^2} \cdot \left(1 - \frac{3}{2} \sin^2 i \right) \cdot \sqrt{1 - e^2} \right)$	degrees / s
Ascending node longitude precession rate	Ω_r	$\Omega_r = -\frac{3J_2 R_e^2}{2p^2} \cdot \bar{n} \cdot \cos i$	degrees / s
Perigee argument precession rate	ω_r	$\omega_r = \frac{3J_2 R_e^2}{2p^2} \cdot \bar{n} \cdot \left(2 - \frac{5}{2} \sin^2 i \right)$	degrees / s

Polar orbits have zero precession rate in ascending node longitude Ω_r and equatorial ones have a maximum precession rate. With prograde satellite motion (an orbit in the same direction as the planet rotates) the ascending node shifts to the West. With retrograde satellite motion, it shifts to the East. The precession rate of the perigee argument ω_r at inclinations of 0 and 180° is maximum. For inclinations of 63.4° and 116.6°, the precession rate is zero. These inclinations are called critical inclination.

Orbit prediction

For a given time point t (in seconds) relative to the reference time (either the start of the simulation or a given “epoch”), the position of the satellite is calculated as follows:

1. Calculate the values of the precessing terms at time point t :

$$\Omega(t) = \Omega_0 + \Omega_r \cdot t \quad (3-1)$$

$$\omega(t) = \omega_0 + \omega_r \cdot t \quad (3-2)$$

$$M(t) = M_0 + \bar{n} \cdot t \quad (3-3)$$

2. Calculate the eccentric anomaly E for elliptical orbits by using an iterative numeric method (e.g. bisection).

$$M(t) = E(t) - e \cdot \sin E(t) \quad (3-4)$$

For circular orbits ($e = 0$), this step can be omitted since $E(t) = M(t)$.

3. Calculate the true anomaly

$$v(t) = 2 \cdot \arctan \sqrt{\frac{1+e}{1-e}} \cdot \tan \frac{E(t)}{2} \quad (3-5)$$

4. Calculate the distance R between the center of the Earth and the satellite.

$$R(t) = \frac{p}{1 + e \cdot \cos v(t)} = \frac{a \cdot (1 - e^2)}{1 + e \cdot \cos v(t)} \quad (3-6)$$

5. Transform the satellite orbital coordinates to inertial Cartesian (x_I, y_I, z_I) coordinates. Inertial coordinates do not consider the Earth's rotation.

$$x_I(t) = R(t) \cdot \{\cos(\omega(t) + v(t)) \cdot \cos \Omega(t) - \sin \Omega(t) \cdot \cos i \cdot \sin(\omega(t) + v(t))\} \quad (3-7)$$

$$y_I(t) = R(t) \cdot \{\cos(\omega(t) + v(t)) \cdot \sin \Omega(t) - \cos \Omega(t) \cdot \cos i \cdot \sin(\omega(t) + v(t))\} \quad (3-8)$$

$$z_I(t) = R(t) \cdot \sin(\omega(t) + v(t)) \cdot \sin i \quad (3-9)$$

6. Calculate the latitude and longitude coordinates of the satellite. Earth's rotation is taken into account and the satellite coordinates are calculated as seen by a fixed observer on Earth (rotating reference frame).

$$\text{lat}(t) = \arctan \frac{z_I(t)}{\sqrt{x_I^2(t) + y_I^2(t)}} \quad (3-10)$$

$$\text{lon}(t) = \arctan_2\{y_I(t), x_I(t)\} - \omega_e \cdot t \quad (3-11)$$

The function $\arctan_2(y, x)$ is the four quadrant inverse tangent of the elements y and x having values between -180° and 180° . The angular rotation rate of the Earth ω_e is given in Table 3-3.

7. Calculate the satellite coordinates in rotating Cartesian (x_R, y_R, z_R) coordinates. The rotating reference frame does consider Earth's rotation.

$$x_R(t) = R(t) \cdot \cos\{\text{lon}(t)\} \cdot \cos\{\text{lat}(t)\} \quad (3-12)$$

$$y_R(t) = R(t) \cdot \sin\{\text{lon}(t)\} \cdot \cos\{\text{lat}(t)\} \quad (3-13)$$

$$z_R(t) = R(t) \cdot \sin\{\text{lat}(t)\} \quad (3-14)$$

MT perspective

This paragraph introduces the transformation from the global perspective to a local, user-centric perspective. The mobile terminals (MTs) need to be placed on a tangential plane on the Earth's surface. For this, a reference position must be given by the latitude lat_{MT} and longitude lon_{MT} where the tangential plane touches the surface of the Earth. The further away a MT is from this reference position, the more the calculations will be distorted by the curvature of the Earth (e.g. the height relative to ground changes with distance to the reference point). As a general rule of thumb, MTs should not be more than 10 km away from the reference position.

1. Transform the MT reference coordinates into the rotating Cartesian reference frame.

$$x_{MT} = R_e \cdot \cos(\text{lon}_{MT}) \cdot \cos(\text{lat}_{MT}) \quad (3-15)$$

$$y_{MT} = R_e \cdot \sin(\text{lon}_{MT}) \cdot \cos(\text{lat}_{MT}) \quad (3-16)$$

$$z_{MT} = R_e \cdot \sin(\text{lat}_{MT}) \quad (3-17)$$

2. Generate a transformation matrix that aligns the rotating Cartesian reference frame with the local Cartesian (QuaDRiGa) frame, i.e. place the reference MT coordinates at the north pole and align the coordinate-system with the QuaDRiGa coordinates (East = 0°, angles increasing counter-clockwise).

$$\mathbf{R}_Q = \begin{bmatrix} -\sin(\text{lon}_{MT}) & \cos(\text{lon}_{MT}) & 0 \\ -\sin(\text{lat}_{MT}) \cdot \cos(\text{lon}_{MT}) & -\sin(\text{lat}_{MT}) \cdot \sin(\text{lon}_{MT}) & \cos(\text{lat}_{MT}) \\ \cos(\text{lat}_{MT}) \cdot \cos(\text{lon}_{MT}) & \cos(\text{lat}_{MT}) \cdot \sin(\text{lon}_{MT}) & \sin(\text{lat}_{MT}) \end{bmatrix} \quad (3-18)$$

3. Calculate the satellite position in local Cartesian (QuaDRiGa) coordinates.

$$\begin{bmatrix} x_Q(t) \\ y_Q(t) \\ z_Q(t) \end{bmatrix} = \mathbf{R}_Q \cdot \begin{bmatrix} x_R(t) - x_{MT} \\ y_R(t) - y_{MT} \\ z_R(t) - z_{MT} \end{bmatrix} \quad (3-19)$$

The satellite is visible (i.e. above the horizon), when $z_Q > 0$. The elevation angle of the satellite has a strong influence on the radio parameters. It is calculated as

$$\alpha(t) = \arctan \frac{z_Q(t)}{\sqrt{x_Q^2(t) + y_Q^2(t)}} \quad (3-20)$$

4. The following steps calculate the satellite orientation. This is important to orient the antenna on the spacecraft with respect to the MT position. It assumes that the spacecraft is 3-axis stabilized, spinning at one revolution per orbit. Hence, for circular orbits, the same side of the satellite always faces the Earth. This general assumption might not be true for elliptical orbits. The first step is to calculate the direction of travel of the satellite in the rotating reference frame. This can be done by

$$\mathbf{D}(t) = \begin{bmatrix} x_R(t + \Delta t) - x_R(t) \\ y_R(t + \Delta t) - y_R(t) \\ z_R(t + \Delta t) - z_R(t) \end{bmatrix}, \text{ and } \hat{\mathbf{D}}(t) = \frac{\mathbf{D}(t)}{|\mathbf{D}(t)|} \quad (3-21)$$

where the orbital position is calculated at time points t and $t + \Delta t$. Δt must be small enough such that the travelling direction does not change, e.g. 100 ms. The resulting distance vector $\hat{\mathbf{D}}(t)$ is normalized to unit length. Furthermore, we need the unit-length vectors $\hat{\mathbf{R}}(t)$ and $\hat{\mathbf{M}}$ as

$$\mathbf{R}(t) = \begin{bmatrix} x_R(t) \\ y_R(t) \\ z_R(t) \end{bmatrix}, \hat{\mathbf{R}}(t) = \frac{\mathbf{R}(t)}{|\mathbf{R}(t)|}, \mathbf{M} = \begin{bmatrix} x_{MT} \\ y_{MT} \\ z_{MT} \end{bmatrix}, \text{ and } \hat{\mathbf{M}} = \frac{\mathbf{M}}{|\mathbf{M}|} \quad (3-22)$$

5. Calculate the bank angle in local Cartesian (QuaDRiGa) coordinates, i.e. the orientation around an axis drawn through the body of the satellite from tail to nose in the normal direction of movement as seen from the MT reference position on Earth.

$$\text{bank}(t) = \arcsin\{\hat{\mathbf{M}}^T \cdot (\hat{\mathbf{R}}(t) \times \hat{\mathbf{D}}(t))\} \quad (3-23)$$

6. Calculate the heading angle in local Cartesian (QuaDRiGa) coordinates, i.e. the direction in which the satellite is pointing.

$$\hat{\mathbf{D}}_Q(t) = \begin{bmatrix} x_{DQ}(t) \\ y_{DQ}(t) \\ z_{DQ}(t) \end{bmatrix} = \mathbf{R}_Q \cdot \hat{\mathbf{D}}(t) \quad (3-24)$$

$$\text{heading}(t) = \arctan_2\{y_{DQ}(t), x_{DQ}(t)\} \quad (3-25)$$

Equation (3-24) transforms the direction of travel of the satellite into the local Cartesian (QuaDRiGa) coordinates.

7. Calculate the tilt angle in local Cartesian (QuaDRiGa) coordinates, i.e. the vertical angle relative to the horizontal plane.

$$\text{tilt}(t) = \arctan_2\left\{z_{DQ}(t), \sqrt{x_{DQ}^2(t) + y_{DQ}^2(t)}\right\} \quad (3-26)$$

Example

The following example visualizes the Quasi-Zenith Satellite System (QZSS), a project of the Japanese government to augment Global Positioning System (GPS) in the Asia-Oceania regions. Three satellites are placed in highly inclined, slightly elliptical, geosynchronous orbits. The Keplerian elements are shown in Table 3-5.

Figure 3-3 shows the satellite orbit for one full orbital period (24 hours). On the left-hand side, the orbit is shown in the inertial, non-rotating, frame. The Earth is shown as a blue sphere and the equatorial plane as a green rectangle. The colors along the orbit ellipse indicate the relative orbital speed, where blue is the slowest and yellow is the fastest speed. On the right-hand side, the orbit is shown for the rotating reference frame that considers the Earth's rotation. Figure 3-4 shows the ground track of the satellite orbit, i.e. the positions on Earth, where the satellite elevation reaches 90°. Finally, Figure 3-5 shows the satellite orbit in the local Cartesian (QuaDRiGa) reference frame. As a reference position, the city of Seoul, Korea, at $\text{lon}_{MT} = 127^\circ$ and $\text{lat}_{MT} = 37.5^\circ$ was chosen. As seen from Seoul, the satellite is visible above the horizon 95% of the time and is almost directly overhead (elevation 60° or more) for 10 hours and 22 minutes each day.

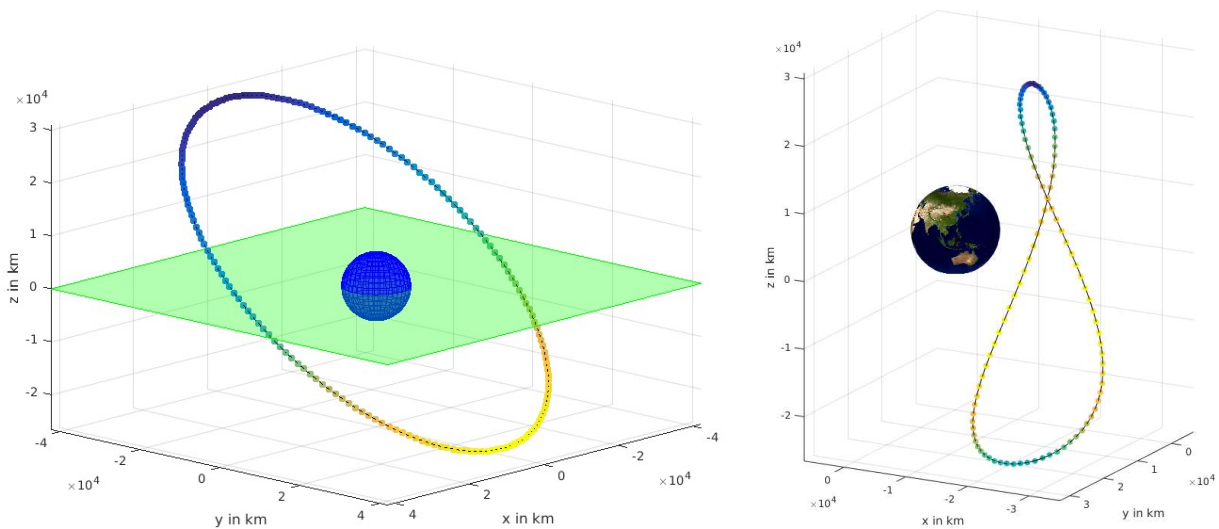


Figure 3-3: QZSS orbit plot in the inertial frame (left) and rotating frame (right)

Table 3-5: Keplerian elements of QZSS satellite

Parameter	Notation	Value	Unit
Semimajor axis	a	42,164	km
Eccentricity	e	0.075	-
Inclination	i	43	deg
Longitude of the ascending node	Ω_0	195	deg
Argument of periapsis	ω_0	270	deg
True anomaly	ν_0	35	deg

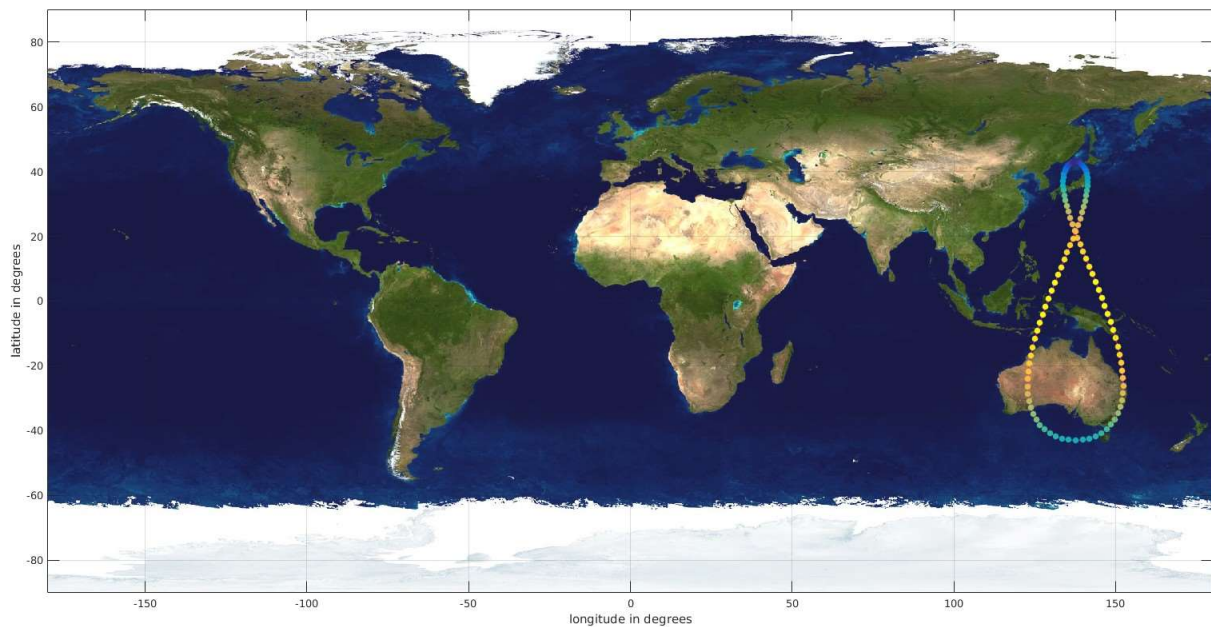


Figure 3-4: QZSS ground track

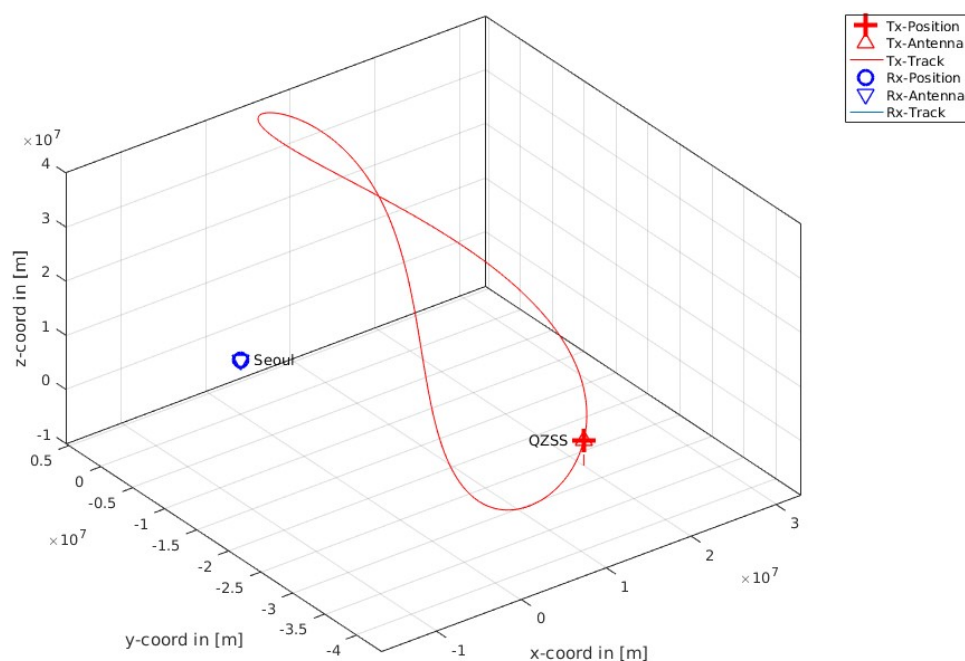


Figure 3-5: QZSS track in local Cartesian (QuaDRiGa) coordinates

3.4 Antenna models

This section provides models for three different antenna types: (1) a typical reflector antenna with a circular aperture providing a single high-gain beam; (2) a simplified model of an advanced phased array beam-forming antenna that can be used either at the spacecraft or at the MT; and (3) a model for terrestrial BS antennas as defined in 3GPP TR 38.901. These antenna types will be used to analyze the interference characteristics in D3.2 of the 5G-ALLSTAR project. In addition, the QuaDRiGa channel simulator allows the import of simulated or measured antenna patterns and array configurations. With that flexibility, it is possible to test and evaluate a huge variety of possible configurations, both at the terrestrial side and at the satellite side.

The channel model separates the propagation and antenna effects. Therefore, it is essential to have a description of the antenna that captures all relevant effects in order to calculate the channel coefficients in the model with a high accuracy. The antennas are defined by their directional response also known as radiation pattern. In addition, the antenna model must consider polarization. The QuaDRiGa channel model uses the polar spherical polarization basis. In the polar spherical basis, the antenna coordinate system has two angles and two poles. The elevation angle θ is measured relative to the pole axis. A complete circle will go through each of the two poles, similar to the longitude coordinate in the world geodetic system (WGS). The azimuth angle ϕ moves around the pole, similar to the latitude in WGS. Thus, the antenna is defined in geographic coordinates.

The electric field is resolved onto three vectors which are aligned to each of the three spherical unit vectors \hat{e}_θ , \hat{e}_ϕ and \hat{e}_r of the antenna coordinate system. In this representation, \hat{e}_r is aligned with the propagation direction of a path. In the far-field of an antenna, there is no field in this direction. Thus, the radiation pattern consists of two components, one is aligned with \hat{e}_θ and another is aligned with \hat{e}_ϕ . It is described by a 2-element vector

$$\mathbf{F}(\theta, \phi) = \begin{bmatrix} F^\theta(\theta, \phi) \\ F^\phi(\theta, \phi) \end{bmatrix}. \quad (3-27)$$

The elements $F^\theta(\theta, \phi)$ and $F^\phi(\theta, \phi)$ are generally complex-valued, consisting of an amplitude and a phase. The directional power of the antenna is given as

$$P(\theta, \phi) = |F^\theta(\theta, \phi)|^2 + |F^\phi(\theta, \phi)|^2. \quad (3-28)$$

3.4.1 Reflector antenna model

A reflector antenna is an antenna that uses a reflector to direct the radio waves. Reflector antennas are used as high-gain antennas for point-to-point communications, e.g. at the satellite to serve a specific region on Earth or at the ground station to connect the satellite with the terrestrial telecommunication infrastructure. It might also be used by MTs (especially in fixed installations for GEO satellites). However, for LEO constellations, the antenna must track the satellite when it passes overhead. With reflector antennas, virtually all the radiated power is concentrated in a narrow main lobe. The residual power is radiated in much smaller sidelobes.

The radiation pattern of the reflector antenna model requires four input variables:

- (1) the radius of the antenna aperture r_A in meters;
- (2) the center frequency f_A in Hz;
- (3) the minimum side lobe power relative to directivity p_{Amin} in dB; and
- (4) the desired polarization which can be either vertical (aligned with \hat{e}_θ), horizontal (aligned with \hat{e}_ϕ), left-hand circular polarized (LHCP), or right-hand circular polarized (RHCP).

The channel model needs the radiation pattern (3-27) sampled at discrete angles. These angles do not need to be equidistant nor do they need to cover the whole sphere. However, interpolating the antenna patterns for each multipath component is a crucial step in the channel generation procedure. Hence, it is desirable to keep the number of sample points low. In addition, reflector antennas have some of the highest gains, meaning that they can produce the narrowest beamwidths of any antenna type. This means that they require a very narrow angular sampling grid in order to capture the beam shape accurately. The following procedure calculates the sampled radiation pattern of an ideal reflector antenna at a reasonable sampling rate.

1. Calculate the antenna pattern $F^\theta(\phi)$ for the vertical polarization (aligned with \hat{e}_θ), assuming that $\theta = 0^\circ$ and $0^\circ \leq \phi \leq 90^\circ$.

$$F^\theta(\phi) = 2 \cdot \frac{J_1(k \cdot \sin \phi)}{k \cdot \sin \phi}, \quad F^\theta(0) = 1 \quad (3-29)$$

The function $J_1(x)$ is the first-order Bessel function and

$$k = \frac{2\pi \cdot r_A \cdot f_A}{c} \quad (3-30)$$

c is the speed of light given in Table 3-3.

2. Find the angle ϕ_{\max} of the smallest side lobe whose maximum power exceeds p_{Amin} and where the next zero-crossing $F^\theta(\phi)$ occurs (i.e. $|F^\theta(\phi)|^2 = 0$). This requires an iterative search to find the angle ϕ where (3-29) becomes 0 after exceeding the power threshold given by p_{Amin} for the last time.
3. Calculate the discrete azimuth angles ϕ_n for the sampled antenna pattern.

$$\phi_n = -\phi_{\max} + n \cdot \Delta\phi \quad (3-31)$$

$$\Delta\phi = \frac{\phi_{\max}}{\text{round}(0.1 \cdot k \cdot \phi_{\max})} \quad (3-32)$$

$$n = 0 \dots N, \quad N = \frac{2 \cdot \phi_{\max}}{\Delta\phi} \quad (3-33)$$

Since the parabolic reflector antenna has a symmetric pattern in azimuth and elevation direction, the same sampling grid is used for the elevation angles θ_m .

4. Calculate the sampled 2D antenna pattern $\bar{F}^\theta(\theta_m, \phi_n)$ for vertical polarization (aligned with \hat{e}_θ) at the discrete elevation angles θ_m and azimuth angles ϕ_n . This is done by calculating a sampling angle

$$\varphi^* = \arccos\{\cos \theta_m \cdot \cos \phi_n\}, \quad \varphi = \begin{cases} \varphi^* & \text{for } \varphi^* < \phi_{\max} \\ 0 & \text{otherwise} \end{cases} \quad (3-34)$$

and solving (3-29) using φ instead of ϕ .

5. Normalize the antenna by its gain $G = k^2$ (i.e. by the ratio of the power received by the antenna along its beam axis to the power received by a hypothetical isotropic antenna).

$$F^\theta(\theta_m, \phi_n) = \bar{F}^\theta(\theta_m, \phi_n) \cdot k \quad (3-35)$$

The two-component radiation pattern for the vertically polarized reflector antenna in the polar-spheric basis then follows as:

$$\mathbf{F}_V(\theta, \phi) = \begin{bmatrix} F^\theta(\theta, \phi) \\ 0 \end{bmatrix} \quad (3-36)$$

6. Calculate the sampled 2-D antenna pattern $F_H(\theta, \phi)$ for horizontal polarization by rotating the 2-D antenna pattern for vertical polarization (3-36) by 90° around the x-axis of the corresponding Cartesian antenna coordinate system. The procedure for polarimetric antenna rotations is given in [4] or [9]. This step is only needed when polarization types other than vertical polarization are required.
7. For circular polarization (LHCP or RHCP), combine the radiation pattern for vertical polarization from step 5 and the pattern for horizontal polarization from step 6 as follows

$$F_{\text{LHCP}}(\theta, \phi) = \frac{F_V(\theta, \phi)}{\sqrt{2}} + j \cdot \frac{F_H(\theta, \phi)}{\sqrt{2}} \quad (3-37)$$

$$F_{\text{RHCP}}(\theta, \phi) = \frac{F_V(\theta, \phi)}{\sqrt{2}} - j \cdot \frac{F_H(\theta, \phi)}{\sqrt{2}} \quad (3-38)$$

Two examples for the directional power radiated by a parabolic antenna are shown in Figure 3-6. On the left-hand side, the pattern is shown for antenna aperture of 0.5 m at 1 GHz carrier frequency. On the right-hand side, the pattern is shown for a 1 m aperture at 17 GHz. One can see that for the higher frequency, significant side lobes are only expected within 10° offset from the main lobe.

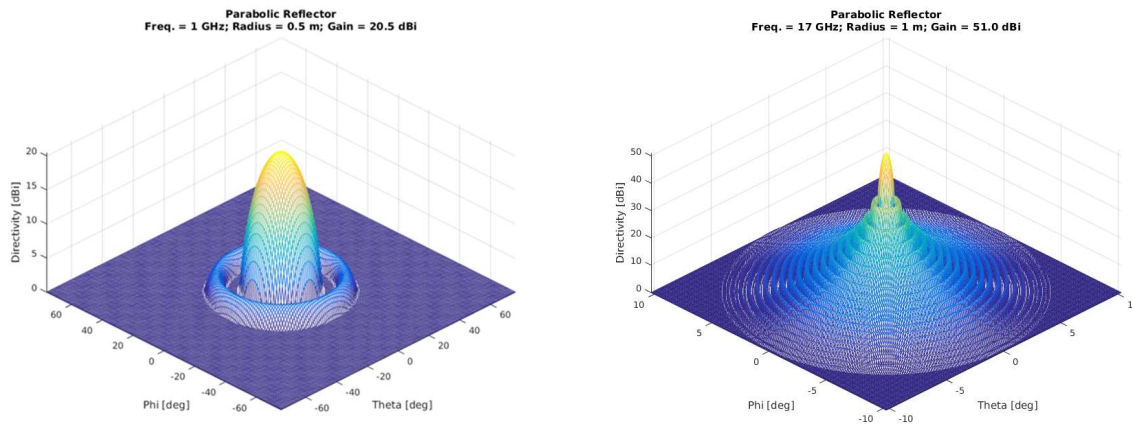


Figure 3-6: Reflector antenna model at 1 GHz and 17 GHz

3.4.2 Model for terrestrial base station antennas

A model for terrestrial BS antennas has been specified by [5]. The antenna model is illustrated in Figure 3-7. The complete list of parameters for the antenna array structures is:

- (1) Number of vertical antenna elements (M) for one nested panel
- (2) Number of horizontal elements (N) for one nested panel
- (3) The center frequency in [Hz]
- (4) The desired polarization which can be either
 - a. vertical (aligned with \hat{e}_θ),
 - b. dual-polarized with linear vertical/horizontal (aligned with \hat{e}_θ and \hat{e}_ϕ)
 - c. dual-polarized with linear $\pm 45^\circ$ orientation
 - d. dual-polarized with LHCP and RHCP
- (5) Element spacing in multiples of the carrier wavelength $[\lambda]$

- (6) Number of nested panels in a column (M_g)
- (7) Number of nested panels in a row (N_g)
- (8) Nested panel spacing in vertical direction ($d_{g,v}$) in multiples of the wavelength $[\lambda]$
- (9) Nested panel spacing in horizontal direction ($d_{g,h}$) in multiples of the wavelength $[\lambda]$

The BS antenna is modelled by a uniform rectangular panel array, comprising $M_g \cdot N_g$ sub-panels. Antenna panels are uniformly spaced in the horizontal direction with a spacing of $d_{g,h}$ and in the vertical direction with a spacing of $d_{g,v}$. On each nested antenna panel, antenna elements are placed in the vertical and horizontal direction, where N and M are the numbers of antenna elements with the same polarization in each column and row, respectively. The element numbering is illustrated in Figure 3-7 assuming viewing the array antenna from the front.

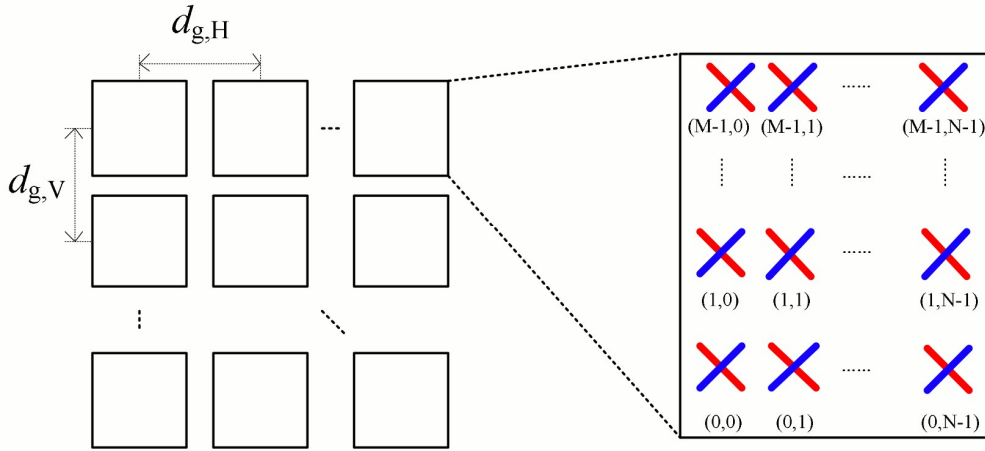


Figure 3-7: Cross-polarized (linear $\pm 45^\circ$) panel array antenna model [5]

The radiation power pattern of a single antenna element is constructed by combining the vertical cut A_v and the horizontal cut A_h of the radiation power pattern (in dB) as follows:

$$F_{v,\text{dB}}^\theta(\theta, 0) = -\min\left\{12 \cdot \left(\frac{\theta}{65^\circ}\right)^2, 30 \text{ dB}\right\}, \quad (3-39)$$

$$F_{h,\text{dB}}^\theta(0, \phi) = -\min\left\{12 \cdot \left(\frac{\phi}{65^\circ}\right)^2, 30 \text{ dB}\right\}, \quad (3-40)$$

$$F_{\text{dB}}^\theta(\theta, \phi) = -\min\{-F_{v,\text{dB}}^\theta(\theta, 0) - F_{h,\text{dB}}^\theta(0, \phi), 30 \text{ dB}\}, \quad (3-41)$$

$$F^\theta(\theta, \phi) = \sqrt{10^{0.1 \cdot F_{\text{dB}}^\theta(\theta, \phi)}}, \quad (3-42)$$

where the θ is the elevation angle ranging from -90° to 90° and ϕ is the azimuth angle ranging from -180° to 180° . The 3 dB beamwidth is set to 65° . The two-component radiation pattern $F_V(\theta, \phi)$ for the vertically polarized patch antenna element in the polar-spheric polarization basis is obtained by eq. (3-36). The 2-D antenna pattern $F_H(\theta, \phi)$ for horizontal polarization is obtained by rotating the 2-D antenna pattern for vertical polarization by 90° around the x-axis of the corresponding Cartesian antenna coordinate system. Likewise, the $\pm 45^\circ$ linear polarization is obtained by rotating the 2-D vertical pattern by 45° either clockwise or counter-clockwise around the x-axis. The procedure for polarimetric antenna rotations is given in [4] or [9]. This step is only needed when polarization types other than vertical polarization are required. Circular polarization (LHCP or RHCP) is obtained by applying eqns. (3-37) and (3-38).

3.5 Spatially-consistent large-scale fading model

Large-scale fading (LSF) describes a set of channel properties that vary slowly over time and space. An example is the shadow-fading (SF) which is caused by buildings or trees blocking a significant part of the signal. The so-called decorrelation distance of the SF, i.e., the distance a MT must move to experience a significant change in the SF, is in the same order of magnitude as the size of the objects causing it. Thus, if a MT travels along a trajectory or if multiple MTs are closely spaced together, their LSPs are correlated. Large-scale parameters can be distinguished into two categories: parameters that determine the overall received signal strength and parameters that determine the properties of the frequency-selective fading caused by multipath-propagation, i.e., reflections of the signal from a satellite at objects around the MT on the ground.

Parameters that determine the overall received signal strength:

- (1) **LOS probability**
i.e. the likelihood that there are no objects between the satellite (or BS) and the MT
- (2) **Path loss and clutter loss**
i.e. the free-space signal attenuation and the average attenuation of the signal power caused by surrounding buildings and objects on the ground
- (3) **Shadow fading**
i.e. random slow variations in signal strength due to shadowing or blocking

Parameters that determine the properties of the frequency-selective fading caused by multipath-propagation:

- (4) **RMS delay spread**
i.e. the temporal spread of the signal due to multipath-propagation
- (5) **Ricean K-factor**
i.e. the power ratio of the direct (LOS) path vs. the sum-power of all other multipath components
- (6) **Cross-polarization ratio**
i.e. the change in polarization due to multipath-propagation
- (7) **Azimuth angular spread of arrival**
i.e. the spread of signal power in the MTs azimuth plane due to multipath-propagation
- (8) **Elevation angular spread of arrival**
i.e. the spread of signal power in elevation (seen from the MT) due to multipath-propagation
- (9) *Azimuth angular spread of departure*
i.e. the spread of signal power in the azimuth plane at the transmitter due to multipath-propagation (this parameter only applies to airborne vehicles and terrestrial BSs)
- (10) *Elevation angular spread of departure*
i.e. the spread of signal power in elevation at the transmitter due to multipath-propagation (this parameter only applies to airborne vehicles and terrestrial BSs)

The following sections describe how these parameters are modelled in 5G-ALLSTAR. The main focus lies on the satellite link. The model shall be usable also for airborne vehicles and seamlessly integrate with existing model for terrestrial mobile communication. The values of large-scale parameters are taken from 3GPP TR 38.811. However, the aim in the 5G-ALLSTAR model is to extend the 3GPP by new features such as spatial consistency and multi-frequency simulations. This requires some modifications to the modelling approach and the parameters.

The communication scenario consists of multiple transmitters (TXs), e.g. satellites, airborne vehicles or terrestrial base-stations, and multiple receivers (RXs) such as fixed terminal, trucks,

cars or phones. Each TX-RX pair can simultaneously operate at one or more carrier frequencies (i.e. multi-band operation) and each RX can be served by multiple TXs (i.e., the model supports multi-connectivity simulations). TX and RX locations are given in 3-D metric Cartesian coordinates respectively. The formulation of the LSF model is done for the dual-mobility case, where both ends of the link are mobile. For any two realizations of a channel, the TX can be in a different position with d_t describing the distance between the two positions. Likewise, the RX can be displaced by a distance d_r . Single-mobility is a special case where either d_t or d_r is zero.

3.5.1 LOS probability model

Line-Of-Sight (LOS) probability depends on the UE's environment and the elevation angle. Reference values for satellites and airborne vehicles have been provided by 3GPP TR 38.811 sec. 6.61 pp. 47. However, this model does not consider spatial consistency. This means that the LOS probability is independently determined for each satellite in the sky and for each MT on the ground. This may lead to unrealistic results for constellations where many satellites are visible at the same time (e.g. for navigation systems using GPS, GLONASS and GALILEO). Objects in the environment such as buildings block the visibility of large connected patches of the sky. Hence, either two satellites that are seen at similar azimuth and elevation angles have a high probability to be both visible or both blocked. A typical example is a street canyon with access to the GPS satellite directly overhead and along the patch of sky that runs parallel to the street, but the sky left and right of the street canyon is blocked by buildings. Spatial consistency must therefore be considered on both sides of the communication link: the satellite side and the MT side (e.g., two cars waiting side by side at a crossing will also see the same satellites).

In order to obtain the LOS state of a communication link between satellite and MT in a spatially consistent way, the coordinates of all potentially visible satellites are needed (i.e. all the satellites that are above the horizon for a given MT reference position on Earth). These coordinates in local Cartesian (QuaDRiGa) coordinates are denoted by (x_s, y_s, z_s) and are obtained using the procedures outlined in Section 3.3. In addition, the coordinates of all mobile terminals (x_m, y_m, z_m) are required in the same local reference frame. Two independent spatially correlated normal distributed random variables $X^S(x_s, y_s, z_s)$ and $X^M(x_m, y_m, z_m)$ are then generated. The first variable depends on the satellite location and the second variable depends on the MT location. If two MTs are at the same location, X^M is identical for the two MTs. The procedure for generating these variables is given by [10].

One important property of these spatially consistent random variables is the autocorrelation function (ACF). The ACF describes how fast the local mean of $X(x, y, z)$ evolves as a terminal or satellite moves. It is modelled as a combination of a Gaussian and an exponential ACF

$$\rho(d, d_\lambda) = \begin{cases} \exp\left(-\frac{d^2}{d_\lambda^2}\right) & \text{for } d < d_\lambda \\ \exp\left(-\frac{d}{d_\lambda}\right) & \text{for } d \geq d_\lambda \end{cases}, \quad (3-43)$$

where d is the distance between two positions (either d_t or d_r) and d_λ is the decorrelation distance, i.e., the distance at which the correlation falls below $\exp(-1) \approx 0.37$. Unlike in terrestrial communication systems, the random number generator for the satellite side X^S has a different decorrelation distance d_λ^S than the generator for the MT side. The decorrelation distance d_λ^M for the MT side is set to 50 m for all scenarios as suggested by [5]. The parameter d_λ^S for the satellite motion, however, depends on the size of the objects that block visibility to the sky, e.g. the size of the buildings at the side of the street. We assume here that the decorrelation distance d_λ^S is equal to 10% of the visible orbit section when the satellite passes directly over the MT. For example, a satellite at 550 km orbit height travels 43,527 km for one full orbit. When it passes directly over the MT, from horizon to horizon, the distance between the two points where its

orbital path intersects the tangential plane when rising above and falling below the horizon is 5,407 km. The decorrelation distance d_{λ}^S is set to 10% of this distance or 541 km.

Now, the two random variables $X^S(x_s, y_s, z_s)$ and $X^M(x_m, y_m, z_m)$ are combined such that the resulting random process depends on both, the satellite and the MT mobility. In order to apply the elevation-dependent probabilities, the resulting random process needs to approach a uniform distribution (i.e., having values between 0 and 1). Given a standard Gaussian stochastic process $k \sim \mathcal{N}(0, 1)$, then remapping the probability density to a Uniform distribution $u \sim \mathcal{U}(0, 1)$ is done using the complementary error function as $u = 0.5 \cdot \text{erfc}(-k/\sqrt{2})$. The combination is done by

$$X(x_s, y_s, z_s, x_m, y_m, z_m) = \frac{1}{2} \cdot \text{erfc}\left(-\frac{X^S(x_s, y_s, z_s) + X^M(x_m, y_m, z_m)}{2}\right). \quad (3-44)$$

For each satellite and MT position, there is an elevation angle α (3-20) and the value of X (3-44) which determine the LOS state (having values true or false) of the link as

$$\text{LOS} = X(x_s, y_s, z_s, x_m, y_m, z_m) > \text{Pr}_{\text{LOS}}(\alpha), \quad (3-45)$$

with $\text{Pr}_{\text{LOS}}(\alpha)$ the elevation-dependent LOS probability from 3GPP TR 38.811 given in Table 3-6. The LOS probability is taken from the linear interpolation between the two nearest reference angles.

Table 3-6: LOS probability from [3]

Elevation	Dense urban	Urban	Suburban and Rural
0°	0 %	0 %	0 %
10°	28.2 %	24.6 %	78.2 %
20°	33.1 %	38.6 %	86.9 %
30°	39.8 %	49.3 %	91.9 %
40°	46.8 %	61.3 %	92.9 %
50°	53.7 %	72.6 %	93.5 %
60°	61.2 %	80.5 %	94.0 %
70°	73.8 %	91.9 %	94.9 %
80°	82.0 %	96.8 %	95.2 %
90°	98.1 %	99.2 %	99.8 %

3.5.2 Path loss and clutter loss

In this section, the free-space loss and the clutter loss models from [3] are combined into a path-loss model that depends on the 3-D distance R in meters between MT and satellite given by eq. (3-6), the carrier frequency f_c in GHz, and the elevation angle α in radians given by eq. (3-20). The parameter $\text{PL}_A(f_c, \alpha)$ is the additional attenuation by atmospheric gases (see Sec. 3.5.3).

$$\text{PL}_{\text{dB}} = A \cdot \log_{10}(R[\text{m}]) + B + C \cdot \log_{10}(f_c[\text{GHz}]) + D \cdot \log_{10}(\alpha[\text{rad}]) + \text{PL}_A(f_c, \alpha) \quad (3-46)$$

The clutter loss (CL) models the average attenuation of signal power caused by surrounding buildings and objects on the ground. It depends on the elevation angle, the carrier frequency, and the environment. The values of CL are given in 3GPP TR 38.811 at reference elevation angles for different scenarios. These values are included in the parameters B , C and D of eq. (3-46). This approach allows a seamless scaling of the PL for the whole frequency range from 2 GHz to 40 GHz as opposed to 3GPP TR 38.811, where only the S or Ka-band are supported. The parameters are listed for the dense urban, urban, suburban and rural scenarios in Table 3-7. Table 3-8 then compares the results from [3] with the outputs of the modified model to ensure that deviations are within reasonable limits.

Table 3-7: Path-loss parameters

Scenario	LOS state	A	B	C	D
Dense Urban and Urban	LOS	20	32.45	20	0
	NLOS	20	54.97	27.93	-11.05
Suburban and Rural	LOS	20	32.45	20	0
	NLOS	20	47.52	22.84	-8.39

Table 3-8: Comparison of NLOS path-loss - 3GPP TR 38.811 vs. 5G-ALLSTAR

Scenario		Freq. Band	Elevation angle							
			10°	20°	30°	40°	50°	60°	70°	80°
Dense Urban and Urban	3GPP TR 38.811	S-band	76.3	72.9	71.0	69.7	68.8	68.2	67.8	67.5
		Ka-band	107.2	102.8	100.4	98.7	97.5	96.7	96.2	95.9
	5G-ALL-STAR	S-band	76.6	73.3	71.3	70.0	68.9	68.0	67.3	66.7
		Ka-band	105.8	102.4	100.5	99.1	98.1	97.2	96.4	95.8
Suburban and Rural	3GPP TR 38.811	S-band	61.5	60.2	60.4	60.3	60.6	59.7	58.5	58.3
		Ka-band	92.4	87.5	84.8	82.9	81.6	80.7	80.1	79.8
	5G-ALL-STAR	S-band	64.8	62.2	60.8	59.7	58.9	58.2	57.7	57.2
		Ka-band	88.6	86.1	84.6	83.6	82.8	82.1	81.6	81.6

3.5.3 Atmospheric absorption

Attenuation by atmospheric gases depends mainly on frequency, elevation angle, altitude above sea level and water vapour density (absolute humidity). Annex 2 of Recommendation ITU-R P.676 [11] gives an approximate method for calculating gaseous attenuation for frequencies up to 350 GHz, which is considered for the 5G-ALLSTAR model as well. This approximate method makes the following assumptions:

- All MTs are located at sea level.
- Ambient temperature is 288.15 Kelvin, or 15° Celsius.
- Air pressure, water-vapour density, and water vapour partial pressure correspond to the mean annual global reference atmosphere given in [12].

For these assumptions, the atmospheric absorption at zenith angle (i.e., when the satellite is directly overhead) is given by Figure 3-8. For an elevation angle α , the corresponding attenuation is given as

$$PL_A(f_c, \alpha) = \frac{PL_A(f_c, 90^\circ)}{\sin \alpha}. \quad (3-47)$$

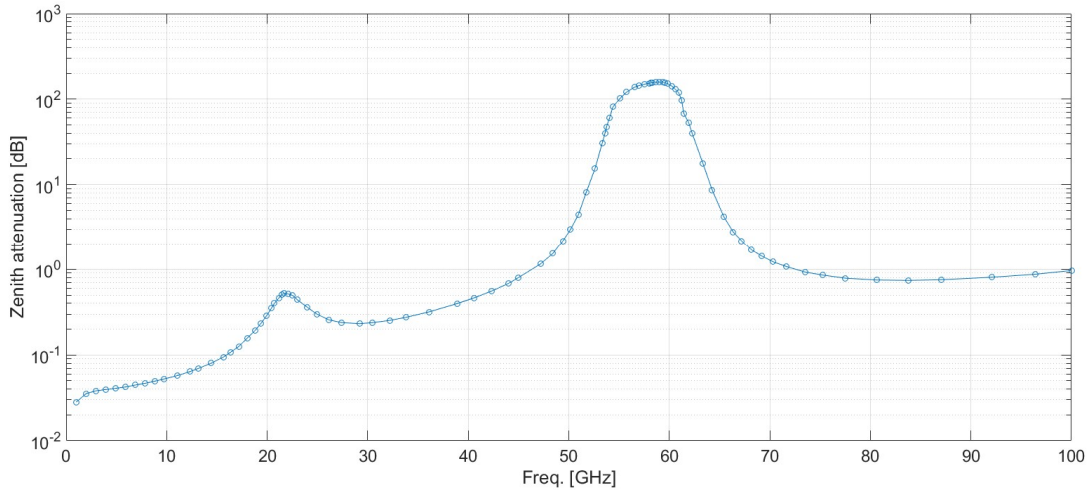


Figure 3-8: Attenuation by atmospheric gases from Annex 2 in [11]

3.5.4 Shadow fading

Shadow fading (SF) occurs when an obstacle is positioned between the wireless device and the signal transmitter, e.g., the satellite. This interference causes a random variation in signal strength because the wave is shadowed or blocked by the obstacle. The average signal attenuation is included as clutter-loss in Table 3-7. The random variation, i.e. the SF, is modeled as a normally distributed power value in dB, above or below the distance dependent PL (3-46) with four parameters:

- (1) the reference standard deviation SF_{σ} (SF-sigma) defines the width of the distribution at a reference frequency of 1 GHz and an elevation angle α of 1 rad or 57.3°;
- (2) the frequency-dependence SF_{δ} (SF-delta) of the reference STD;
- (3) the elevation-dependence SF_{β} (SF-beta) of the reference STD; and
- (4) the decorrelation distance SF_{λ} (SF-lambda) in meters.

The last parameter defines how fast the SF varies when the terminal moves through the environment. E.g., a value of 50 means that when the terminal moves 50 m in any given direction, then the correlation of the SF values at this distance with the value at the initial position is equal to $\exp(-1) \approx 0.37$. The SF is then calculated as

$$SF_{dB} = X_{SF}(x_s, y_s, z_s, x_m, y_m, z_m) \cdot \{SF_{\sigma} + SF_{\delta} \cdot \log_{10}(f_c[\text{GHz}]) + SF_{\beta} \cdot \log_{10}(\alpha[\text{rad}])\}, \quad (3-48)$$

where X_{SF} is a spatially correlated normally distributed random variable that depends on both, the satellite position (x_s, y_s, z_s) and the MT position (x_m, y_m, z_m) . It is constructed by generating two independent spatially correlated normally distributed random variables $X_{SF}^S(x_s, y_s, z_s)$ and $X_{SF}^M(x_m, y_m, z_m)$, which are then combined to

$$X_{SF}(x_s, y_s, z_s, x_m, y_m, z_m) = \frac{X_{SF}^S(x_s, y_s, z_s) + X_{SF}^M(x_m, y_m, z_m)}{2}. \quad (3-49)$$

The autocorrelation function (ACF) of X_{SF}^S and X_{SF}^M is given by eq. (3-43). The decorrelation distance of X_{SF}^M is equal to SF_{λ} , whereas the decorrelation distance of X_{SF}^S is equal to 10% of the visible orbit section when the satellite passes directly over the MT. The SF values are given in 3GPP TR 38.811 at reference elevation angles for different scenarios. These values are mapped to the parameters of eq. (3-48), which are listed in Table 3-9.

Table 3-9: Shadow-fading parameters

Scenario	LOS state	SF_{σ}	SF_{δ}	SF_{β}	SF_{λ}
Dense Urban	LOS	2.95	-0.31	-0.69	37
	NLOS	9.54	2.57	-5.96	50
Urban	LOS	4	0	0	37
	NLOS	6	0	0	50
Suburban	LOS	0.8	1.2	0	37
	NLOS	10.03	0.85	0.99	50
Rural	LOS	4	0	0	37
	NLOS	8	0	0	120

A comparison of the combined PL and SF models from [3] and the 5G-ALLSTAR model is given in Figure 3-9. The figures do not contain the distance-dependence, but only the dependence in the elevation angle and carrier frequency. The magenta dots are samples generated as proposed by the 3GPP model. This model is only valid for two distinct frequency bands: S-band and Ka-band and does not support spatial consistency. The 2D surface in the figures was generated by the values given in Table 3-7 and Table 3-9. It is based on the 3GPP parameters but is seamlessly scalable for the whole frequency range.

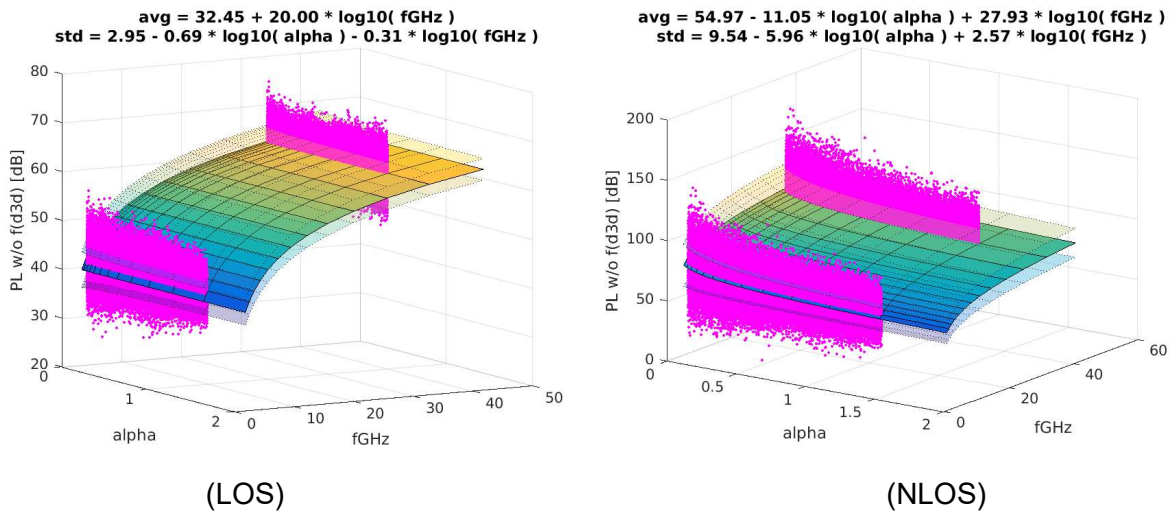


Figure 3-9: Dense urban PL and SF - 3GPP TR 38.811 vs. 5G-ALLSTAR

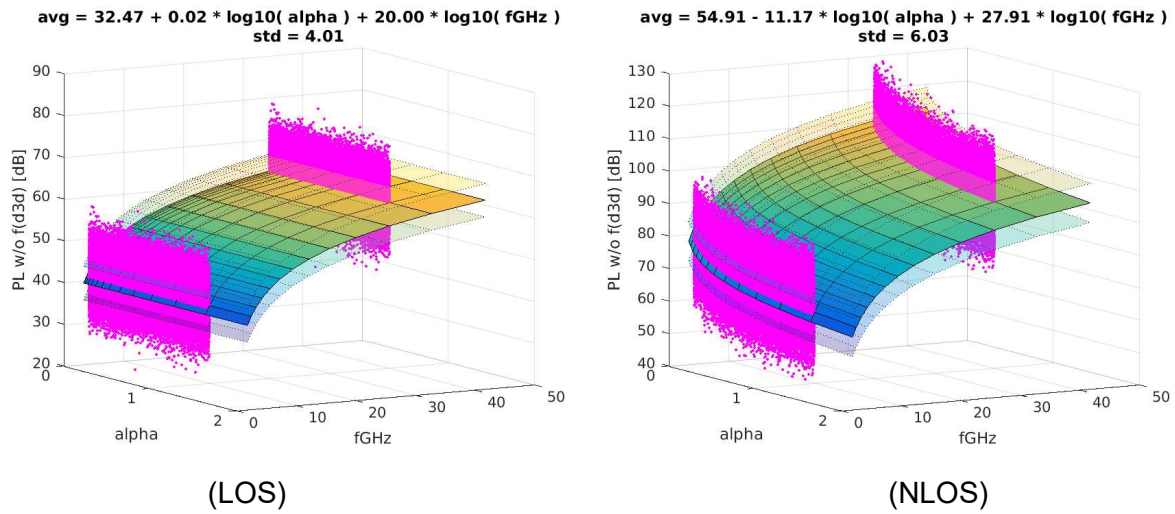


Figure 3-10: Urban PL and SF - 3GPP TR 38.811 vs. 5G-ALLSTAR

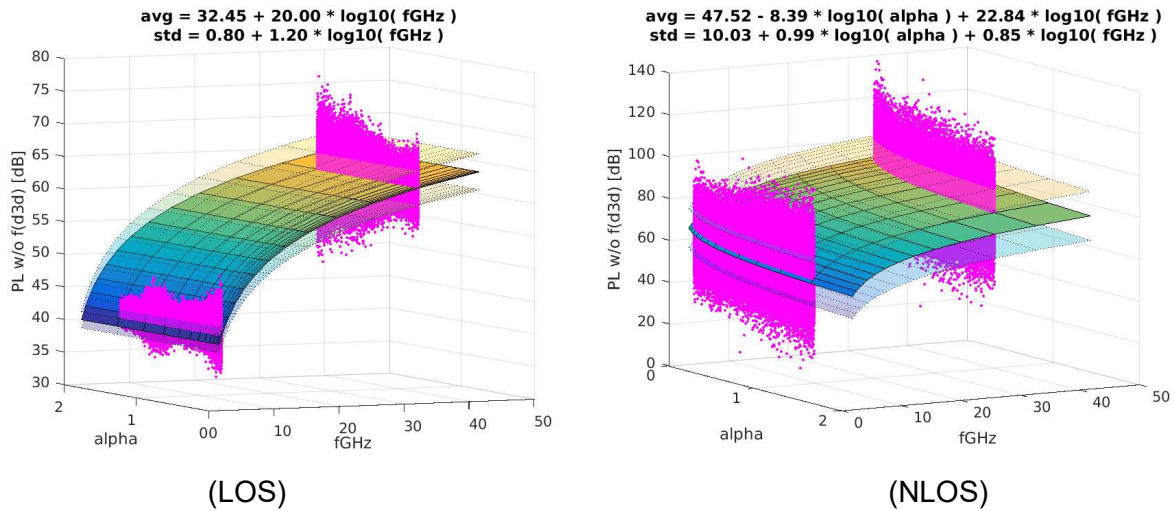


Figure 3-11: Suburban PL and SF - 3GPP TR 38.811 vs. 5G-ALLSTAR

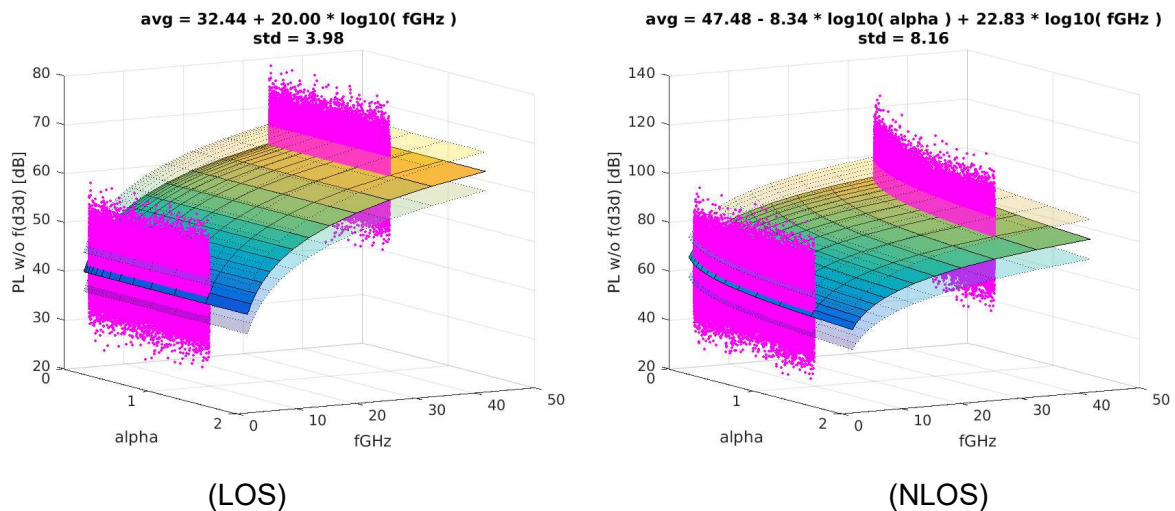


Figure 3-12: Rural PL and SF - 3GPP TR 38.811 vs. 5G-ALLSTAR

3.5.5 Multipath parameters

The remaining large-scale parameters determine the properties of the frequency-selective fast-fading model. Those are the delay-spread (DS), the Ricean K-Factor (KF), the four values of the angular spread and the cross-polarization ratio (XPR). They are part of the LSF model because the parameters themselves are relatively constant over time and location. However, they provide the input to the small-scale-fading model in section 3.6, which creates the multipath-scattering clusters. Multipath fading (or fast-fading, small-scale-fading) results from the constructive or destructive superposition of multiple copies of the same signal. This kind of fading happens on the scale of the carrier wavelength. Multipath effects are uncritical for fixed-satellite services at Ku- and Ka-band that use high-gain beam-steering antennas. However, they have a significant impact at lower frequencies used for mobile satellite and positioning services.

Each of the five multipath parameters depends on up to seven variables that describe the random fluctuations of a parameter:

- (1) the reference value μ (mu) at a carrier frequency of 1 GHz, a TX-RX distance of 1 m and an elevation angle of 57.3° (1 rad);
- (2) the reference standard deviation σ (sigma) defines the width of the distribution at a reference frequency of 1 GHz and an elevation angle of 57.3° ;
- (3) the decorrelation distance λ (lambda) in meters;
- (4) the frequency-dependence γ (gamma) of the reference value;
- (5) the elevation-dependence α (alpha) of the reference value;
- (6) the frequency-dependence δ (delta) of the reference STD; and
- (7) the elevation-dependence β (beta) of the reference STD.

The first three parameters, i.e., the reference value μ , the reference STD σ and the decorrelation distance λ must be specified for each LSP. Parameters that are not specified are set to zero. Given the positions of the TX and the RX as $\mathbf{p} = (x_s, y_s, z_s, x_m, y_m, z_m)$, the initial value of the delay spread (DS) follows from

$$DS(\mathbf{p}) = DS_\mu + DS_\lambda \cdot \log_{10}(f_c[\text{GHz}]) + DS_\alpha \cdot \log_{10}(\alpha[\text{rad}]) + X_{DS}(\mathbf{p}) \cdot \{DS_\sigma + DS_\delta \cdot \log_{10}(f_c[\text{GHz}]) + DS_\beta \cdot \log_{10}(\alpha[\text{rad}])\}, \quad (3-50)$$

where $X_{DS}(\mathbf{p})$ is a spatially correlated normally distributed random variable having zero-mean, unit variance and an ACF which is a combination of a Gaussian and an exponential ACF given by eq. (3-43). The method for generating this variable is identical to the procedure used for the shadow fading in Section 3.5.4. The same procedure applies to the KF, the XPR and the four angular spreads.

The values of each parameter are given in [3] at reference elevation angles for different scenarios. These values are mapped to the parameters in Table 3-10 for the dense urban scenario, Table 3-11 for the urban scenario, Table 3-12 for the suburban scenario, and Table 3-13 for the rural scenario.

Table 3-10: Channel model parameters for dense urban scenario

Parameter		LOS	NLOS
No. Clusters	L	4 (incl. 1 for LOS)	5
No. sub-paths	M	20	20
Delay Spread	μ	$-7.89 - 0.22 \log_{10}(f) - 1.23 \log_{10}(\alpha)$	$-7.44 - 0.11 \log_{10}(f) - 1.21 \log_{10}(\alpha)$
(log ₁₀ s)	σ	$0.53 - 0.51 \log_{10}(\alpha)$	$0.5 - 0.43 \log_{10}(\alpha)$
Decorr. dist (m)	λ	30	40
Delay factor	r_T	2.5	2.3
Per-Cluster DS (ns)		$4.95 - 2.2 \log_{10}(f)$	$4.95 - 2.2 \log_{10}(f_c)$
K-Factor	μ	$6.36 + 2.05 \log_{10}(f) + 0.58 \log_{10}(\alpha)$	N / A
(db)	σ	$3.35 + 0.15 \log_{10}(f) - 3.6 \log_{10}(\alpha)$	N / A
Decorr. dist (m)	λ	12	N / A
ASA	μ	$0.85 - 0.35 \log_{10}(f) - 0.45 \log_{10}(\alpha)$	$1.49 - 0.12 \log_{10}(f) + 0.2 \log_{10}(\alpha)$
(log ₁₀ °)	σ	$0.55 + 0.16 \log_{10}(f)$	$0.59 + 0.11 \log_{10}(f) - 0.9 \log_{10}(\alpha)$
Decorr. dist (m)	λ	15	50
Per-Cluster ASA (°)		11	15
ESA / ZSA	μ	$1.44 + 1.18 \log_{10}(\alpha)$	$1.48 + 0.78 \log_{10}(\alpha)$
(log ₁₀ °)	σ	$0.11 - 0.45 \log_{10}(\alpha)$	$0.28 - 0.51 \log_{10}(\alpha)$
Decorr. dist (m)	λ	15	50
Per-Cluster ESA (°)		7	7
ASD	μ	$-1.92 - 0.44 \log_{10}(f) + 1.21 \log_{10}(\alpha)$	$-1.28 - 0.11 \log_{10}(f) + 0.85 \log_{10}(\alpha)$
(log ₁₀ °)	σ	$0.35 + 0.12 \log_{10}(f)$	$0.55 + 0.08 \log_{10}(f) - 0.29 \log_{10}(\alpha)$
Decorr. dist (m)	λ	18	50
Per-Cluster ASD (°)		0	0
ESD / ZSD	μ	$-2.3 - 0.26 \log_{10}(f)$	$-1.62 - 0.09 \log_{10}(f) + 0.17 \log_{10}(\alpha)$
(log ₁₀ °)	σ	$0.47 + 0.05 \log_{10}(f)$	$0.46 + 0.1 \log_{10}(f)$
Decorr. dist (m)	λ	15	50
Per-Cluster ESD (°)		0	0
XPR	μ	$19.78 + 1.9 \log_{10}(f) - 4.82 \log_{10}(\alpha)$	$13.9 + 0.45 \log_{10}(f) - 14.38 \log_{10}(\alpha)$
(dB)	σ	$9 - 2.62 \log_{10}(f) + 6.49 \log_{10}(\alpha)$	$13.61 - 0.38 \log_{10}(f) + 13.79 \log_{10}(\alpha)$
Decorr. dist (m)	λ	20	50

Table 3-11: Channel model parameters for urban scenario

Parameter		LOS	NLOS
No. Clusters	L	12	20
No. sub-paths	M	20	20
Delay Spread	μ	$-8.27 - 0.12 \log_{10}(f) - 0.06 \log_{10}(\alpha)$	$-8.09 - 0.73 \log_{10}(\alpha)$
(log ₁₀ s)	σ	$0.29 - 1.04 \log_{10}(\alpha)$	$0.77 - 0.67 \log_{10}(\alpha)$
Decorr. dist (m)	λ	30	40
Delay factor	r_T	2	2.3
Per-Cluster DS (ns)		$4.95 - 2.2 \log_{10}(f)$	$4.95 - 2.2 \log_{10}(f)$
K-Factor	μ	9	-100
(db)	σ	3.5	0
Decorr. dist (m)	λ	12	50
ASA	μ	$-1.36 - 0.38 \log_{10}(f) - 1.48 \log_{10}(\alpha)$	$0.54 + 0.73 \log_{10}(\alpha)$
(log ₁₀ °)	σ	$4.45 + 1.43 \log_{10}(\alpha)$	$1.92 - 2.33 \log_{10}(\alpha)$
Decorr. dist (m)	λ	15	50
Per-Cluster ASA (°)		11	15
ESA / ZSA	μ	$1.64 + 4.08 \log_{10}(\alpha)$	$1.34 + 2.2 \log_{10}(\alpha)$
(log ₁₀ °)	σ	$0.44 - 1.78 \log_{10}(\alpha)$	$0.77 - 0.91 \log_{10}(\alpha)$
Decorr. dist (m)	λ	15	50
Per-Cluster ESA (°)		7	7
ASD	μ	$-3.9 - 0.37 \log_{10}(f) - 0.97 \log_{10}(\alpha)$	$-2.33 + 0.66 \log_{10}(\alpha)$
(log ₁₀ °)	σ	$3.66 + 1.52 \log_{10}(\alpha)$	$2.02 - 2.34 \log_{10}(\alpha)$
Decorr. dist (m)	λ	18	50
Per-Cluster ASD (°)		0	0
ESD / ZSD	μ	$-2.63 + 0.73 \log_{10}(\alpha)$	$-2.72 - 0.55 \log_{10}(\alpha)$
(log ₁₀ °)	σ	$0.5 - 0.66 \log_{10}(\alpha)$	$2.71 + 2.56 \log_{10}(\alpha)$
Decorr. dist (m)	λ	15	50
Per-Cluster ESD (°)		0	0
XPR	μ	8	7
(dB)	σ	4	3
Decorr. dist (m)	λ	15	50

Table 3-12: Channel model parameters for suburban scenario

Parameter		LOS	NLOS
No. Clusters	L	8	5
No. sub-paths	M	20	20
Delay Spread	μ	$-8.54 + 0.05 \log_{10}(f)$	$-9.15 + 0.59 \log_{10}(f) - 1.22 \log_{10}(\alpha)$
(log ₁₀ s)	σ	$1.27 - 0.59 \log_{10}(f)$	$1.83 - 0.82 \log_{10}(f)$
Decorr. dist (m)	λ	30	40
Delay factor	r_T	2.3	2.3
Per-Cluster DS (ns)		1.6	1.6
K-Factor	μ	$21.32 - 8.42 \log_{10}(f)$	-100
(db)	σ	$17.75 - 8.49 \log_{10}(f)$	0
Decorr. dist (m)	λ	12	50
ASA	μ	$-0.69 + 0.31 \log_{10}(f) - 0.9 \log_{10}(\alpha)$	$-0.05 + 0.46 \log_{10}(f) - 1.12 \log_{10}(\alpha)$
(log ₁₀ °)	σ	$2.2 - 0.96 \log_{10}(f) - 0.37 \log_{10}(\alpha)$	$1.68 - 0.49 \log_{10}(f)$
Decorr. dist (m)	λ	15	50
Per-Cluster ASA (°)		11	15
ESA / ZSA	μ	$-2.69 + 2.76 \log_{10}(f) + 0.97 \log_{10}(\alpha)$	$-2.88 + 2.74 \log_{10}(f) + 0.56 \log_{10}(\alpha)$
(log ₁₀ °)	σ	$1.15 - 0.54 \log_{10}(f)$	$2 - 1.05 \log_{10}(f) - 0.22 \log_{10}(\alpha)$
Decorr. dist (m)	λ	15	50
Per-Cluster ESA (°)		7	7
ASD	μ	$-3.29 + 0.12 \log_{10}(f) + 0.86 \log_{10}(\alpha)$	$-3.74 + 0.86 \log_{10}(f) + 0.6 \log_{10}(\alpha)$
(log ₁₀ °)	σ	$2.14 - 1.11 \log_{10}(f) - 0.41 \log_{10}(\alpha)$	$2.22 - 1.04 \log_{10}(f)$
Decorr. dist (m)	λ	18	50
Per-Cluster ASD (°)		0	0
ESD / ZSD	μ	$-0.42 - 1.73 \log_{10}(f)$	$-1 - 1.25 \log_{10}(f) + 0.27 \log_{10}(\alpha)$
(log ₁₀ °)	σ	$1.2 - 0.57 \log_{10}(f)$	$1.83 - 0.87 \log_{10}(f)$
Decorr. dist (m)	λ	15	50
Per-Cluster ESD (°)		0	0
XPR	μ	$19.6 + 2.47 \log_{10}(f)$	$9.27 + 2.29 \log_{10}(f) - 12.08 \log_{10}(\alpha)$
(dB)	σ	$11.69 - 3.9 \log_{10}(f)$	$14.05 - 2.68 \log_{10}(f) + 3.86 \log_{10}(\alpha)$
Decorr. dist (m)	λ	20	50

Table 3-13: Channel model parameters for rural scenario

Parameter		LOS	NLOS
No. Clusters	L	11	11
No. sub-paths	M	20	20
Delay Spread	μ	$-8.3 + 1.52 \log_{10}(\alpha)$	$-8.12 + 1.1 \log_{10}(\alpha)$
(log ₁₀ s)	σ	$0.12 - 0.59 \log_{10}(\alpha)$	$1.11 - 0.73 \log_{10}(\alpha)$
Decorr. dist (m)	λ	50	36
Delay factor	r_T	3.8	1.7
Per-Cluster DS (ns)		0	0
K-Factor	μ	7	-100
(db)	σ	4	0
Decorr. dist (m)	λ	40	40
ASA	μ	$-1.31 - 0.7 \log_{10}(f) + 5.83 \log_{10}(\alpha)$	$0.45 + 3.07 \log_{10}(\alpha)$
(log ₁₀ °)	σ	$3.81 - 4.31 \log_{10}(\alpha)$	$1.62 - 5.13 \log_{10}(\alpha)$
Decorr. dist (m)	λ	35	40
Per-Cluster ASA (°)		4	3
ESA / ZSA	μ	$1.7 + 2.06 \log_{10}(\alpha)$	$1 + 1.33 \log_{10}(\alpha)$
(log ₁₀ °)	σ	$0.18 - 0.73 \log_{10}(\alpha)$	$1.06 - 0.4 \log_{10}(\alpha)$
Decorr. dist (m)	λ	15	50
Per-Cluster ESA (°)		4	3
ASD	μ	$-3.67 - 0.69 \log_{10}(f) + 6.92 \log_{10}(\alpha)$	$-2.28 + 5.61 \log_{10}(\alpha)$
(log ₁₀ °)	σ	$3.69 - 3.97 \log_{10}(\alpha)$	$1.6 - 6.6 \log_{10}(\alpha)$
Decorr. dist (m)	λ	25	30
Per-Cluster ASD (°)		2	2
ESD / ZSD	μ	$-2.53 + 1.06 \log_{10}(\alpha)$	$-2.64 + 1.5 \log_{10}(\alpha)$
(log ₁₀ °)	σ	$0.36 - 0.14 \log_{10}(\alpha)$	$2.51 - 0.25 \log_{10}(\alpha)$
Decorr. dist (m)	λ	15	50
Per-Cluster ESD (°)		2	2
XPR	μ	12	7
(dB)	σ	4	3
Decorr. dist (m)	λ	25	40

3.5.6 Inter-parameter correlation model

The LSPs are correlated with each other. For example, a high K-Factor means that a large fraction of the received power is carried by the direct LOS-path. This leads to low values for the delay-spread and the angular spreads. Hence, the KF is negatively correlated with these parameters. On the other hand, the existence of a free LOS also means that the overall received power is often much higher, leading to a positive correlation between KF and SF.

The generation of correlated LSPs is then done in four steps:

- (1) generation of spatially correlated random variables X_{SF} , X_{DS} , X_{KF} , X_{ASD} , X_{ASA} , X_{ESD} , X_{ESA} , and X_{XPR} in the logarithmic domain,
- (2) application of the inter-parameter correlations in the logarithmic domain,
- (3) application of parameter-dependent averages and STDs, e.g. by equations (3-47) or (3-50), and
- (4) transformation to the linear domain.

In order to account for the inter-LSP correlation, a 8×8 matrix \mathbf{R} is assembled containing all cross-correlation values ρ between each two LSPs. Cross-correlation values for the different scenarios are given in Table 3-14. Then, the square root matrix $\mathbf{R}^{0.5}$ is calculated such that $\mathbf{R}^{0.5} \cdot \mathbf{R}^{0.5} = \mathbf{R}$ [13]. In order to calculate the square root matrix, \mathbf{R} must be positive definite to get a unique, real-valued solution. This is not always the case for the parameters given in 3GPP TR 38.811. Hence, minor adjustments were necessary to fulfil this requirement.

Table 3-14: Inter-parameter correlations

Cross-Correlations		LOS							
		DS	KF	SF	ASD	ASA	ESD	ESA	XPR
N L O S	DS Dense Urb.	1	-0.4	0	0.4	0.6	-0.2	0	0
	Urban	1	-0.4	-0.4	0.4	0.52	-0.2	0	0
	Suburban	1	-0.4	-0.4	0.4	0.8	-0.2	0	0
	Rural	1	-0.5	0	0	0	0	0.27	0
	KF Dense Urb.	0	1	0	0	-0.2	0	0	0
	Urban	0	1	0	0	-0.2	0	0	0
	Suburban	0	1	0	0	-0.2	0	0	0
	Rural	0	1	0	0	0	0	0	0
	SF Dense Urb.	-0.4	0	1	-0.3	-0.5	0	-0.7	0
	Urban	-0.4	0	1	-0.5	-0.5	0	-0.8	0
	Suburban	-0.4	0	1	-0.5	-0.5	0	-0.8	0
	Rural	-0.5	0	1	0	0	0	-0.17	0
	ASD Dense Urb.	0.4	0	-0.6	1	0	0.5	0	0
	Urban	0.4	0	-0.6	1	0	0.5	0	0
	Suburban	0.4	0	-0.6	1	0	0.5	0	0
	Rural	-0.4	0	0.6	1	0	0.73	-0.14	0
	ASA Dense Urb.	0.6	0	-0.5	0	1	-0.3	0.4	0
	Urban	0.6	0	0	0.4	1	0	0.4	0
	Suburban	0.6	0	0	0.4	1	-0.3	0.4	0
	Rural	0	0	0	0	1	-0.2	0.24	0
	ESD Dense Urb.	-0.5	0	0	0.5	-0.3	1	0	0
	Urban	-0.5	0	0	0.5	0	1	-0.3	0
	Suburban	-0.5	0	0	0.5	0	1	0	0
	Rural	-0.1	0	0	0.42	-0.18	1	-0.07	0
	ESA Dense Urb.	0	0	-0.4	-0.1	0.4	0	1	0
	Urban	0	0	-0.4	-0.1	0	0	1	0
	Suburban	0	0	-0.4	-0.1	0	0	1	0
	Rural	-0.4	0	-0.25	-0.27	0.26	-0.27	1	0
	XPR Dense Urb.	0	0	0	0	0	0	0	1
	Urban	0	0	0	0	0	0	0	1
	Suburban	0	0	0	0	0	0	0	1
	Rural	0	0	0	0	0	0	0	1

3.6 Small-scale-fading model

The small-scale-fading (SSF) model generates the multipath components, which are responsible for the fast fading of a received signal. Multipath fading results from the constructive or destructive superposition of multiple copies of the same signal. This kind of fading happens on the scale of the carrier wavelength. A transmitted signal is reflected and scattered by objects in the environment such that multiple copies of that signal are received by the RX. Each signal path consists of a departure direction at the TX, a first-bounce scatterer (FBS), a last-bounce scatterer (LBS), and an arrival direction at the RX. Departure and arrival directions are given in geographic coordinates consisting of an azimuth angle ϕ and an elevation angle θ . The azimuth angle ϕ is defined in mathematic sense, i.e., seen from above, a value of zero points to the east and the angles increase counter-clockwise. The elevation angle θ is oriented relative to the horizontal plane. Positive angles point upwards.

Initial delays for the NLOS paths are drawn randomly from a single-sided exponential distribution with unit mean and unit variance as

$$\tilde{\tau}_l(\mathbf{p}) = -\ln\{X_l^\tau(\mathbf{p})\}, \quad (3-51)$$

where the index l denotes the path number and $X_l^\tau \sim \mathcal{U}(0,1)$ is a spatially correlated uniformly distributed random variable having values between 0 and 1. The position vector $\mathbf{p} = (x_s, y_s, z_s, x_m, y_m, z_m)$ describes the satellite and terminal positions. The line of sight (LOS) delay, i.e., the delay of the first path, is set to zero. The initial delays are not scaled by the DS nor are the angles scaled by the AS. The ACF of X_l^τ is given by eq. (3-43). If TX and RX are swapped, path delays must be identical. This is known as channel reciprocity and can be modelled by generating random variables X_l^τ in (3-51) as

$$X_l^\tau(\mathbf{p}) = \frac{1}{2} \cdot \operatorname{erfc}\left(-\frac{\tilde{X}_l^\tau(x_s, y_s, z_s) + \tilde{X}_l^\tau(x_m, y_m, z_m)}{2}\right), \quad (3-52)$$

where the complementary error function maps the spatially correlated normally distributed random variables $\tilde{X}_l^\tau \sim \mathcal{N}(0,1)$ to a uniform distribution required by (3-51). As for the delays, the initial values for the angles are generated spatially consistent, having the same ACF and decorrelation distance. The NR model [5] proposes to obtain the azimuth angles from a wrapped Gaussian distribution, the elevation angles from a wrapped Laplacian distribution, and the path power from a single slope exponential power delay profile (PDP). However, this leads to large angle offsets when the power values are small and the AS is large. Due to the wrapping operation, the achievable AS is limited. In order to have a larger range of possible angular spreads, we propose to draw all initial NLOS angles from a uniform distribution and apply the desired AS by a subsequent scaling operation. The initial arrival azimuth angles are calculated by generating two independent spatially correlated normally distributed random variables \tilde{X}_l^A and \tilde{X}_l^B and combining them to

$$\tilde{\phi}_l^a(\mathbf{p}) = \frac{\pi}{2} \cdot \operatorname{erfc}\left(-\frac{\tilde{X}_l^B(x_s, y_s, z_s) + \tilde{X}_l^A(x_m, y_m, z_m)}{2}\right) - \frac{\pi}{2}, \quad (3-53)$$

where the complementary error function maps the resulting values to $\mathcal{U}(-\pi/2, \pi/2)$. The same procedure is repeated for the initial elevation angles $\tilde{\theta}_l^a(\mathbf{p})$. The initial angles for the LOS path are set to zero. In a satellite communication mode with typical orbit heights of 400 km or more, it is assumed that multipath propagation can only happen due to objects close to the receiver. Hence, the angular spread at the satellite is negligible.

The initial delays $\tilde{\tau}_l$ and the initial angles $\tilde{\phi}_l^a$ and $\tilde{\theta}_l^a$ are assumed to be frequency-independent, i.e., a MT sees the same scattering clusters at different frequencies and therefore, the same angles and delays are used. However, DS and AS are generally frequency-dependent [14]. For example, the DS at a carrier frequency of 24 GHz is generally shorter than at 3 GHz. The NR model [5] proposes an optional method that can adjust the path powers such that different delay and angular spreads can be achieved. The power values are calculated as

$$\tilde{P}_{l,f} = \exp\{-\tilde{\tau}_l \cdot g_f^{\text{DS}}\} \cdot \exp\{-(\tilde{\phi}_l^a)^2 \cdot g_f^{\text{AS}}\} \cdot \exp\{-|\tilde{\theta}_l^a| \cdot g_f^{\text{ES}}\} \quad (3-54)$$

where the index f refers to the $f = 1 \dots F$ carrier frequencies. The scaling coefficients g_f^{DS} , g_f^{AS} , and g_f^{ES} need to be calculated such that the frequency-dependent differences in the spreads are reflected in the powers. The DS scaling coefficient g_f^{DS} is calculated by fitting a logarithmic function to the delays in eq. (3-51), assuming that the powers are obtained from $\tilde{P}_{l,f} = \exp\{-\tilde{\tau}_l \cdot g_f^{\text{DS}}\}$.

$$g_f^{\text{DS}} = -1.5 \cdot \ln\{1.2 \cdot \overline{\text{DS}}_f - 0.15\} \quad (3-55)$$

If there is no frequency dependency of the DS (e.g., when simulations are done for a single frequency only), then g_f^{DS} will have a value of 1.2. For multi-frequency simulations, the delay-spread values from eq. (3-50) must be normalized to obtain a value $\overline{\text{DS}}_f$ for each frequency.

$$\overline{\text{DS}}_f^* = \frac{\text{DS}_f}{\max_{\forall f}(\text{DS}_f) + \min_{\forall f}(\text{DS}_f)}, \quad \overline{\text{DS}}_f = \max\{\min(\overline{\text{DS}}_f^*, 0.15), 0.85\} \quad (3-56)$$

The initial angles (3-53) are uniformly distributed having values in between $-\pi/2$ and $\pi/2$. As for the DS, the scaling coefficients for the angular spreads g_f^{AS} and g_f^{ES} are obtained by

$$g_f^{\text{AS}} = -2.2 \cdot \ln\{1.5 \cdot \overline{\text{AS}}_f - 0.35\}, \quad (3-57)$$

$$g_f^{\text{ES}} = -3.4 \cdot \ln\{1.2 \cdot \overline{\text{AS}}_f - 0.10\}, \quad (3-58)$$

$$\overline{\text{AS}}_f = \min\left(\frac{0.75 \cdot \text{AS}_f}{\max_{\forall f}(\text{AS}_f)}, 0.25\right). \quad (3-59)$$

If there is no frequency dependency, then g_f^{AS} will have a value of 0.56, which corresponds to an initial azimuth spread of 42° . The scaling coefficient g_f^{ES} will have a value of 0.76, which corresponds to an initial elevation spread of 44° . Both can be scaled down to 14° at a different frequency.

Next, the absolute values of the KF, the DS and the four ASs are applied. These values were generated by the LSF model in Section 3.5.5. The KF is the ratio between the power of the direct path and the sum-power of all other paths. It is applied by scaling the power of the first path and normalizing the PDP to unit power. This is done independently for each frequency.

$$\tilde{P}_{1,f} = \text{KF}_f \cdot \sum_{l=2}^L \tilde{P}_{l,f}, \quad P_{l,f} = \tilde{P}_{1,f} / \sum_{l=1}^L \tilde{P}_{l,f} \quad (3-60)$$

The DS measures how the multipath power is spread out over time. Given the cluster-powers (3-60) initial delays (3-51), the initial DS is calculated as

$$\widetilde{\text{DS}}_f(\mathbf{p}) = \sqrt{\sum_{l=1}^L P_{l,f} \cdot \{\tilde{\tau}_l\}^2 - \left(\sum_{l=1}^L P_{l,f} \cdot \tilde{\tau}_l\right)^2} \quad (3-61)$$

The values $\widetilde{\text{DS}}_f(\mathbf{p})$ are frequency-dependent due to the scaling of the path powers in (3-54), but do not contain the correct DS values from the LSF model. Hence, the delays need to be scaled such that the correct DS can be calculated from the generated path-delays and path-powers. This is done by

$$\tau_l = \tilde{\tau}_l \cdot \frac{1}{F} \sum_{f=1}^F \frac{DS_f}{\overline{DS}_f} \quad (3-62)$$

The AS measures how the multipath power is spread out in the spatial domain. The AS is ambiguous since the angles are distributed on a sphere and the resulting value depends on the reference angle, i.e., the definition of where 0° is. A linear shift of the angles $\phi_l + \Delta\phi$ leads to the AS being a function of $\Delta\phi$. We therefore normalize the angles such that the combined power-angular spectrum (PAS) of all paths and sub-paths points to $\phi = \theta = 0$. The AS is calculated by

$$\Delta\phi_f = \arg \left(\sum_{l=1}^L P_{l,f} \cdot \exp(j\tilde{\phi}_l^a) \right) \quad (3-63)$$

$$\hat{\phi}_{l,f}^a = \arg \left(\exp \left(j(\tilde{\phi}_l^a - \Delta\phi_f) \right) \right) \quad (3-64)$$

$$\widetilde{AS}_f(\mathbf{p}) = \sqrt{\sum_{l=1}^L P_{l,f} \cdot \{\hat{\phi}_{l,f}^a\}^2 - \left(\sum_{l=1}^L P_{l,f} \cdot \hat{\phi}_{l,f}^a \right)^2} \quad (3-65)$$

With AS_f being the initial AS from the LSF model, the initial angles $\tilde{\phi}_l^a$ (3-53) are scaled to

$$\phi_l^a = \arg \exp \{ j \cdot \tilde{\phi}_l^a \cdot s \}, \quad s = \frac{1}{F} \sum_{f=1}^F \frac{AS_f}{\widetilde{AS}_f}, \quad s < \begin{cases} 3.0 & \text{for azimuth angles} \\ 1.5 & \text{for elevation angles} \end{cases} \quad (3-66)$$

The $\arg \exp$ function wraps the angles around the unit circle. The scaling coefficient s is limited to a maximum value of 3 for the scaling of the azimuth angles and 1.5 for the elevation angles. This is motivated by the distribution of the initial angles in (3-53). More power is assigned to the angles having values close to zero than to those having values close to $\pm\pi/2$. For this reason, $s = 3$ achieves the maximum azimuth AS of around 80° and $s = 1.5$ achieves the maximum elevation AS of around 45° . Larger values of s tend to decrease the AS again due to the wrapping around the unit circle.

The last step is to apply the direction of the LOS path. The initial values of the LOS angles in (3-53) were set to zero. However, the correct angles need to take the positions of the TX and the RX into account. The LOS angles are

$$\phi_1^d = \arctan_2 \{ y_m - y_s, x_m - x_s \} \quad (3-67)$$

$$\phi_1^a = \phi_1^d + \pi \quad (3-68)$$

$$\theta_1^d = \arctan_2 \left\{ z_m - z_s, \sqrt{(x_m - x_s)^2 + (y_m - y_s)^2} \right\} \quad (3-69)$$

$$\theta_1^a = -\theta_1^d \quad (3-70)$$

where $\arctan_2 \{ y, x \}$ is the four quadrant inverse tangent of the elements y and x having values between $-\pi$ and π . Those angles are applied by two 3-D rotations in Cartesian coordinates, one for the TX and one for the RX.

$$\begin{pmatrix} c_{l,x} \\ c_{l,y} \\ c_{l,z} \end{pmatrix} = \begin{pmatrix} \cos \theta_1 \cdot \cos \phi_1 & -\sin \phi_1 & -\sin \theta_1 \cdot \cos \phi_1 \\ \cos \theta_1 \cdot \sin \phi_1 & \cos \phi_1 & -\sin \theta_1 \cdot \sin \phi_1 \\ \sin \theta_1 & 0 & \cos \theta_1 \end{pmatrix} \cdot \begin{pmatrix} \cos \theta_l \cdot \cos \phi_l \\ \cos \theta_l \cdot \sin \phi_l \\ \sin \theta_l \end{pmatrix} \quad (3-71)$$

$$\phi_l = \arctan_2 \{ c_{l,y}, c_{l,x} \} \quad (3-72)$$

$$\theta_l = \arctan_2 \left\{ c_{l,z}, \sqrt{c_{l,x}^2 + c_{l,y}^2} \right\} \quad (3-73)$$

4 Ray tracing-based channel model

In this chapter, a ray tracing (RT) simulation is conducted in order to investigate the channel characteristics for a scenario where both the terrestrial moving network (MN) and satellite systems provide connectivity to a vehicle. Several channel parameters including path loss and RMS delay spread are provided by the ray tracing simulation.

4.1 Objective

The objectives of the RT-based channel modelling for the terrestrial and satellite links are as follows:

- Develop the RT simulation for millimeter wave (mmWave) wireless communication in a typical urban scenario and a highway scenario, respectively.
- Characterize the target channel with consideration of the terrestrial communication link from base station (BS) to vehicle user equipment (UE) and the satellite-terrestrial communication link from a transmitter (Tx) on a satellite, called Koreasat 6, to a satellite UE carried by an SUV.
- Consider the propagation attenuation for each link.
- Study the interference between a terrestrial MN system and a satellite-terrestrial communication link.

4.2 CloudRT simulator

In this section, mmWave networks in typical urban and highway scenarios have been developed by an RT simulator, which models wave propagation and calculates all possible rays between the transmitter and the receiver by using the principles of geometric optics [15]. Once all the rays are traced, the amplitude and the phase of each ray can be calculated by coupling with the antenna patterns and polarizations. Because of the deterministic map-based channel modeling approach, RT requires precise 3-dimensional (3D) environment model indicating the geometry of the objects and the corresponding material. It also requires an accurate propagation mechanism model. The most time consuming part of RT simulations is the tracing of rays, especially when the reflection order is higher or propagation constitution becomes complex. As a result, more accurate simulation tasks bring more complexity in tracing rays and electromagnetic (EM) calculations.

In recent years, cloud computing has become a highly demanded service or utility due to the advantages of high computing power, cheap cost of services, high performance, scalability, accessibility as well as availability [16]. Developing RT over high performance computing (HPC) platform can significantly improve the efficiency of RT without sacrificing the accuracy. Such a publicly available high-performance RT platform (CloudRT) has been developed in Beijing Jiaotong University and is open access to the community via <http://raytracer.cloud>.

The architecture design of the CloudRT simulator platform is shown in Figure 4-1. The CloudRT is composed of UEs, the HPC, and the data server. All the components are connected via internet to exchange commands and data. The HPC server, in which the RT engine is implemented, contains 600 CPU cores, 5 GPUs, and 44 TB storage. It can monitor and manage the simulation tasks, and realize parallel computing via Message Passing Interface (MPI). The data server of CloudRT contains three libraries (environment, antenna and material libraries) and two databases (user database and task database).

- **Environment library** manages the 3D environment models for various communication scenarios.
- **Antenna library** manages radiation patterns for various types of single antennas and arrays.

- **Material library** stores material parameters.

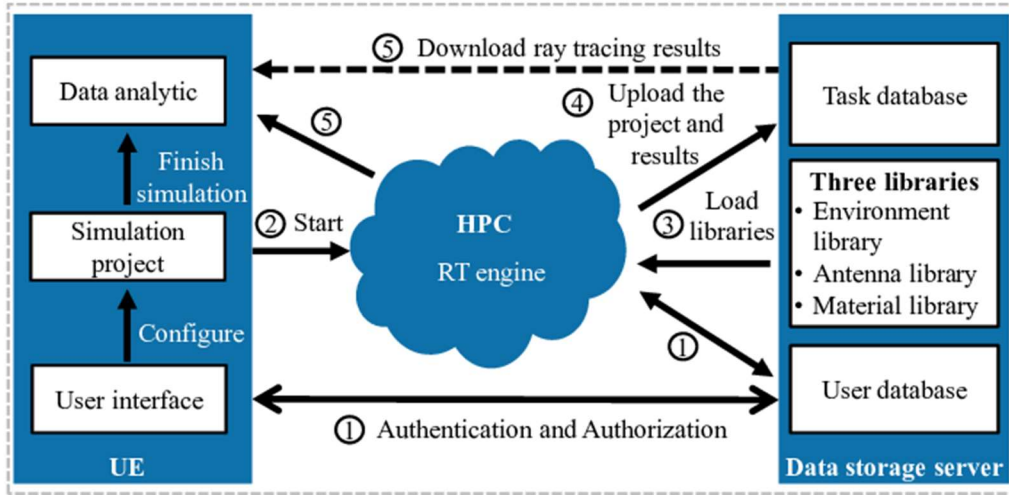


Figure 4-1: Workflow of CloudRT

4.3 Excess propagation attenuation for a terrestrial link

Gaseous attenuation and rain attenuation are significant for mmWave link, and therefore, are added into the CloudRT simulation.

4.3.1 Attenuation due to atmospheric gases

The attenuation due to absorption by oxygen and water vapour is always present, and should be included in the calculation of total propagation attenuation at frequencies above about 10 GHz.

The attenuation due to atmospheric gases (A_α) on a path of length d (km) is given in Recommendation ITU-R P.530-17 [17] by:

$$A_\alpha = \gamma_\alpha d \quad \text{dB} \quad (4-1)$$

where the specific attenuation γ_α (dB/km) can be obtained from Recommendation ITU-R P.676-11 [18]. It is clear that the attenuation due to atmospheric gases is distance dependent, and therefore, should be calculated according to the concrete distance.

In the case of MN system, the γ_α is 0.2 dB/km for a frequency of 22.6 GHz. Assuming that the (designed) maximum link length of MN system is 0.6 km, then the maximum value of attenuation by atmospheric gases in this case is around 0.12 dB.

4.3.2 Attenuation due to rain

Although rain attenuation can be ignored at frequencies below about 5 GHz, it must be included in the design for higher frequencies, where its importance increases rapidly. A technique for estimating long-term statistics of rain attenuation is given in Recommendation ITU-R P.530-17 [17]. The following simple technique may be used for estimating the long-term statistics of rain attenuation:

- Step 1: Obtain the rain rate $R_{0.01}$ exceeded for 0.01% of the time (with an integration time of 1 min). If this information is not available from local sources of long-term measurements, an estimate can be obtained from the information given in Recommendation ITU-R P.837-7 [19].

$$R_{0.01} = 60.724 \quad \text{mm/hr} \quad (4-2)$$

- Step 2: Compute the specific attenuation, γ_R (dB/km) for the frequency, polarization and rain rate of interest using Recommendation ITU-R P.838-3 [20].

$$\gamma_R = k(R_{0.01})^\alpha = 7.0954 \quad \text{dB/km} \quad (4-3)$$

- Step 3: Compute the effective path length d_{eff} of the link by multiplying the actual path length d by a distance factor r . An estimate of this factor is given by:

$$r = \frac{1}{0.477d^{0.633}R_{0.01}^{0.073\alpha}f^{0.123} - 10.579(1 - \exp(-0.024d))} = 1.9044 \quad (4-4)$$

where f (GHz) is the frequency and α is the exponent in the specific attenuation model from Step 2. Note that the maximum recommended r is 2.5, so if the denominator of the equation above is less than 0.4, use $r = 2.5$.

- Step 4: An estimate of a given path (here still assuming 0.6 km as the maximum designed MN system link length) attenuation exceeded for 0.01% of the time is given by:

$$A_{0.01} = \gamma_R \cdot d_{\text{eff}} = \gamma_R \cdot d \cdot r = 7.0954 \cdot 0.6 \cdot 1.9044 = 8.1074 \quad \text{dB} \quad (4-5)$$

It is clear that the attenuation due to rain is distance dependent, and therefore, should be calculated according to the concrete distance. However, in general, we should have the concept that the maximum value of attenuation by rain for a MN system (assuming 0.6 km as the maximum designed link length) is not larger than 8.1074 dB.

4.4 Excess propagation attenuation for a satellite link

The excess propagation attenuation on a satellite-terrestrial communication link is the sum of different contributions as follows:

- Attenuation due to atmospheric gases
- Attenuation due to rain, other precipitation and clouds
- Attenuation due to tropospheric scintillation
- Clear-air effects
- Focusing and defocusing
- Decrease in antenna gain due to wave-front incoherence
- Scintillation and multipath effects
- Attenuation by sand and dust storms

Each of these contributions has its own characteristics as a function of frequency, geographic location and elevation angle. Depending on propagation conditions, generally at elevation angles above 10° , only gaseous attenuation, rain and cloud attenuation and possible scintillation will be significant.

4.4.1 Attenuation due to atmospheric gases

Atmospheric absorption attenuation refers to the attenuation of radio waves when passing through the earth's atmosphere, which is caused by the absorption of EM wave energy by atmospheric molecules. In microwave and mmWave bands, oxygen and water vapour are the main components of atmospheric gas absorption. An oxygen molecule has a magnetic dipole moment and a water molecule has a residual electric dipole moment. Under the action of an electromagnetic field, when the frequency of the electromagnetic wave is consistent with the transition frequency of the molecular rotational energy level, the molecule absorbs the energy of the electromagnetic wave, and its rotational energy level transits from low to high, forming resonance absorption.

Attenuation by atmospheric gases, which is entirely caused by absorption, depends mainly on frequency, elevation angle, altitude above sea level and water vapour density (absolute humidity). At frequencies below 10 GHz, it may normally be neglected. However, for elevation angles below 10 degrees it is recommended that the calculation is performed for any frequency above 1 GHz.

A typical value for the elevation angle from the satellite Koreasat 6 to Seoul is about 45° (The accurate elevation angle should be obtained by ray-tracing). The technical report of ITU-R P.676-11 [18] details the corresponding zenith attenuation $A_{\text{zenith}}(f)$ for frequencies between 1 and 350 GHz. We can get $A_{\text{zenith}}(f)$ as 0.5 dB when the frequency is 22.6 GHz according to ITU-R P.676-11. In our work, we only consider the mentioned frequency and elevation angle. For an elevation angle α , the corresponding attenuation $PL_A(\alpha, f)$ is given by:

$$PL_A(\alpha, f) = \frac{A_{\text{zenith}}(f)}{\sin \alpha} = \frac{0.5 \text{ dB}}{\sin 45^\circ} = 0.7071 \text{ dB} \quad (4-6)$$

Therefore, the typical value of attenuation due to atmospheric gases is 0.7071 dB.

4.4.2 Attenuation due to rain

Rain attenuation refers to the attenuation of radio waves when passing through the rainy area. The higher the frequency of radio waves, the shorter the wavelength. The wavelengths of Ku-band and Ka-band microwaves with frequencies above 10 GHz are only 10 to 30 mm, which are comparable to raindrops of several millimeters in diameter. Therefore, dense raindrops will cause serious transmission loss for high-frequency radio waves above Ku-band when passing through the rainy area.

Due to the uncertainty of the occurrence time and region of rainfall, it is impossible to calculate the attenuation by rain accurately. After decades of observation and research, ITU-R and its predecessor CCIR have summarized the methods of estimating the maximum rain attenuation statistics for different time probabilities. The calculation of long-term rain attenuation statistics from point rainfall rate is given in Recommendation ITU-R P.618-13 [21]. By using it, the long-term statistics of the slant-path rain attenuation at a given location for frequencies up to 55 GHz can be estimated. The typical value of attenuation by rain is calculated by 30.0162 dB (for the case that the typical value of elevation angle from the satellite Koreasat 6 to Seoul is about 45°).

4.4.3 Attenuation due to clouds and fog

Clouds and fog are important condensates of water vapour in nature. The attenuation due to clouds and fog has great influence on millimeter wave transmission such that the influence on radio waves of a satellite communication link cannot be ignored. In general, when the frequency of radio waves is higher than 10 GHz, it is necessary to consider the attenuation by clouds and fog, but only when the frequency is higher than 50 GHz, the attenuation is important.

Clouds and fogs have smaller particles, which are suspended in the air. The number of particles per cubic centimeter ranges from 100 to 500 and the size of particles is much smaller than the wavelength of millimeter waves. The density of particles is not uniform, and the types of clouds and fog are diverse, which makes it difficult to calculate the attenuation accurately. The attenuation due to clouds and fog can be calculated by the total columnar content of cloud liquid water in Recommendation ITU R P.840-7 [22]. A mathematical model based on Rayleigh scattering, which uses a double-Debye model for the dielectric permittivity of water, can be used to approximately calculate the attenuation for frequencies up to 200 GHz. Using the above model, a typical value of attenuation by clouds and fog is 2.1677 dB (assuming an elevation angle of 45°).

4.4.4 Attenuation due to tropospheric scintillation

Tropospheric scintillation is a phenomenon that causes rapid fluctuation of signal amplitude and phase in satellite communication systems. Unlike ionospheric scintillation, the effect of tropospheric scintillation on signals increases with an increasing carrier frequency, especially above 10 GHz. In this case, the sudden change of refractive index caused by the change of temperature, vapour content and air pressure result in the fluctuation of the signal.

The amplitude of tropospheric scintillations depends on the magnitude and structure of the refractive index variations along the propagation path. Amplitude scintillations increase with frequency and with the path length, and decrease as the antenna beamwidth decreases due to aperture averaging. Measured data shows the monthly-averaged RMS fluctuations are well correlated with the wet term of the radio refractivity N_{wet} , which depends on the water vapour content of the atmosphere.

A general technique for predicting the cumulative distribution of tropospheric scintillation at elevation angles greater than or equal to 5 degrees is given in Recommendation ITU-R P.618-13 [21]. The model described therein, reflects the specific climatic conditions of the site as based on monthly or longer averages of temperature and relative humidity. Since the average surface temperature and average surface relative humidity vary with season, the distribution of the scintillation fade depths varies with season. The seasonal variation may be predicted by using seasonal average surface temperature and seasonal average surface relative humidity. This information may be obtained from weather information for the site of interest.

Although the procedure has only been tested at frequencies between 7 and 14 GHz, it is recommended for applications for up to at least 20 GHz. Using the above method, a typical value of attenuation by tropospheric scintillation is 0.7638 dB (assuming an elevation angle of 45°).

4.4.5 Estimation of total attenuation due to multiple sources of simultaneously occurring atmospheric attenuation

For systems operating at frequencies above about 18 GHz, and especially those operating with low elevation angles and/or margins, the effect of multiple sources of simultaneously occurring atmospheric attenuation must be considered [21].

The total attenuation, i.e. the combined effect of rain, gas, clouds and scintillation, adds up to 32.9001 dB for rainy day and 3.0054 dB for sunny day, respectively.

4.5 Simulation configuration

The simulation scenarios of typical urban and highway are defined and reconstructed. In total, 16 cases are simulated (sampling interval: 1.38 m in urban scenario and 1.17 m in highway scenario, respectively). We consider the impact of different weather conditions by differentiating between rainy and sunny days. In addition, we consider not only the target links, but also the interference between them.

4.5.1 Vehicle types

In this work, two different vehicle types are considered in both urban and highway scenarios. Referring to the considered terrestrial MN system and the satellite-terrestrial communication link, a bus and an SUV are defined in the simulations, respectively. The vehicle types and the antenna location are detailed as follows:

- Bus for MN system: length 13 meters, width 2.6 meters, height 3 meters, antenna height 0.2 meters over the top of the bus (Figure 4-2).

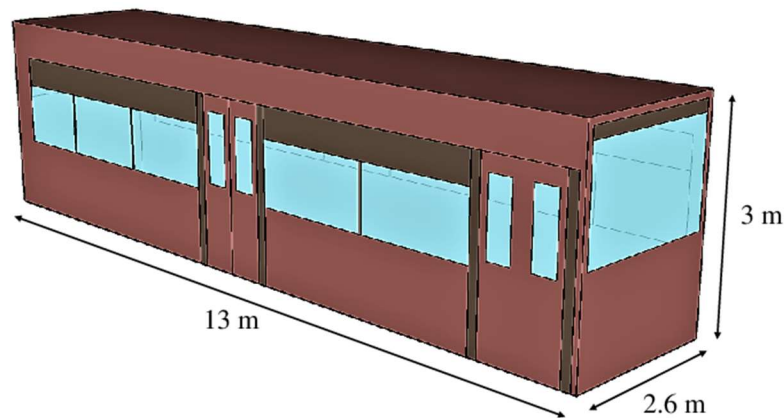


Figure 4-2: Modeling of a bus

- SUV for satellite-terrestrial communication link: length 5 meters, width 2.0 meters, height 1.75 meters, antenna height 0.65 meters over the top of the SUV (Figure 4-3).

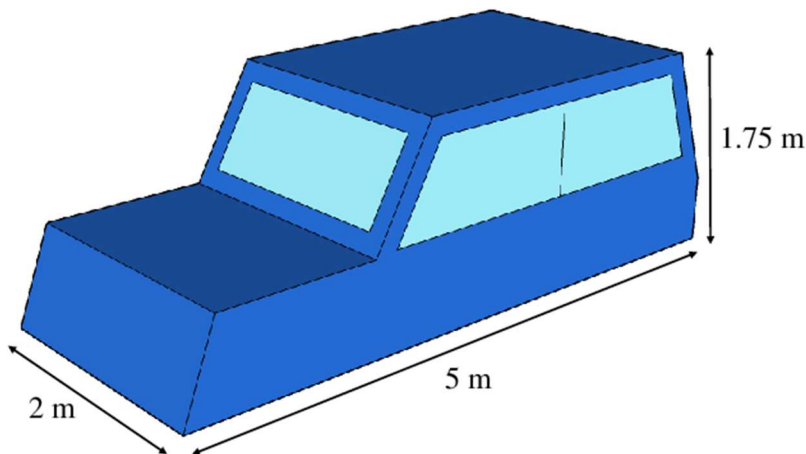


Figure 4-3: Modeling of an SUV

4.5.2 Antenna model

The antennas' configurations for terrestrial MN systems and satellite-terrestrial communication links are different. For terrestrial MN systems, Tx and Rx antennas are merged into one single antenna. For satellite-terrestrial link, the Tx antenna called APSMLA609V01 on the satellite is provided by ITU and the Rx antenna is modelled according to ITU-R S.456-6 [23]. The locations and heights of each Tx and Rx are shown in Table 4-1, while the antenna patterns are shown in Figure 4-4 and Figure 4-5, respectively.

Table 4-1: Locations and heights of each Tx and Rx

Communication link	Parameters	Urban	Highway
*Terrestrial MN system	BS VeUE	Top of the building: 25 m Top of the bus: 3.2 m	On the traffic light: 10 m Top of the bus: 3.2 m
*Satellite-terrestrial link	SA SaUE	GEO position: 116° E Top of the SUV: 2.4 m	GEO position: 116° E Top of the SUV 2.4 m

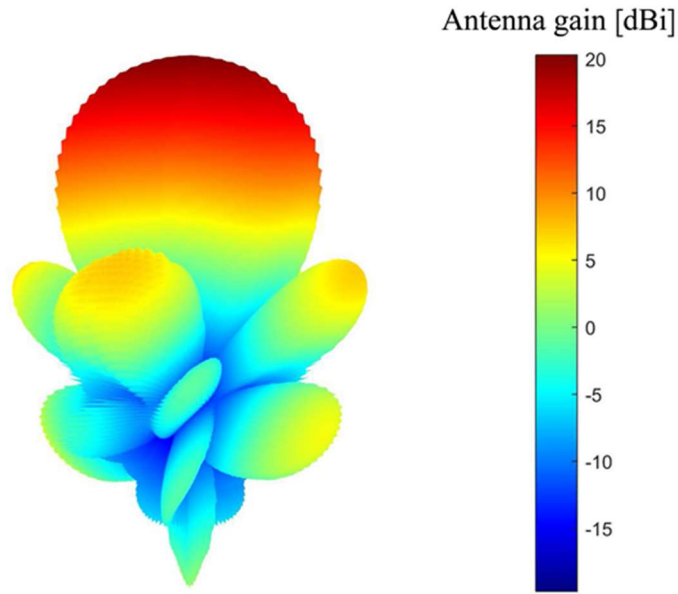


Figure 4-4: Tx and Rx antenna pattern for a terrestrial link

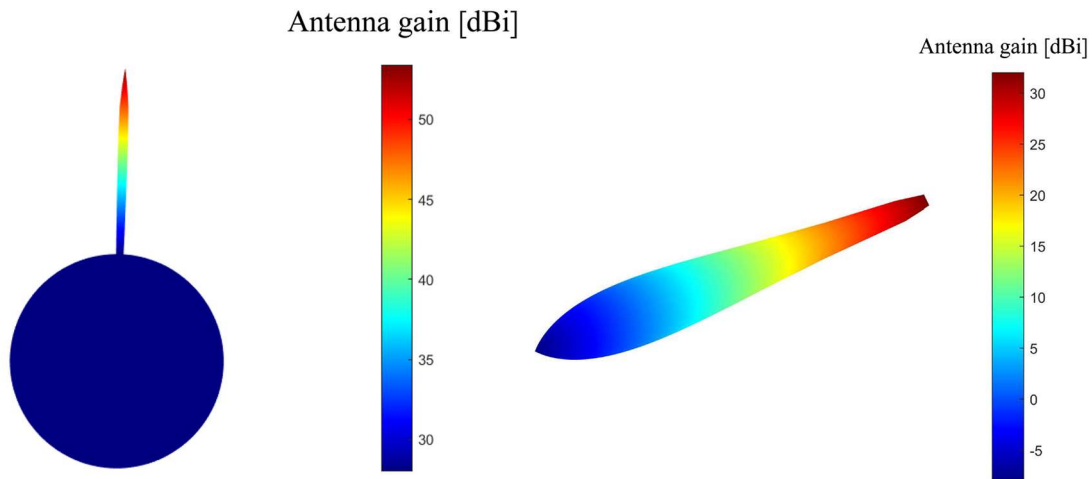


Figure 4-5: Tx and Rx antenna patterns for a satellite link: Satellite antenna pattern (left); Satellite UE antenna pattern (right).

4.5.3 Scenario description

Two scenarios are investigated namely urban and highway scenarios. For the urban scenario, the reconstructed 3D environment model is used with calibrated electromagnetic (EM) parameters. Urban signal propagation data for 22.1 – 23.1 GHz is measured in Seoul in Korea, and the EM parameters are calibrated in our previous work. What's more, the 3D details of the considered environment are rebuilt based on OpenStreetMap (OSM). The urban street for Seoul is reconstructed as in Figure 4-6, where the street has 4 lanes.

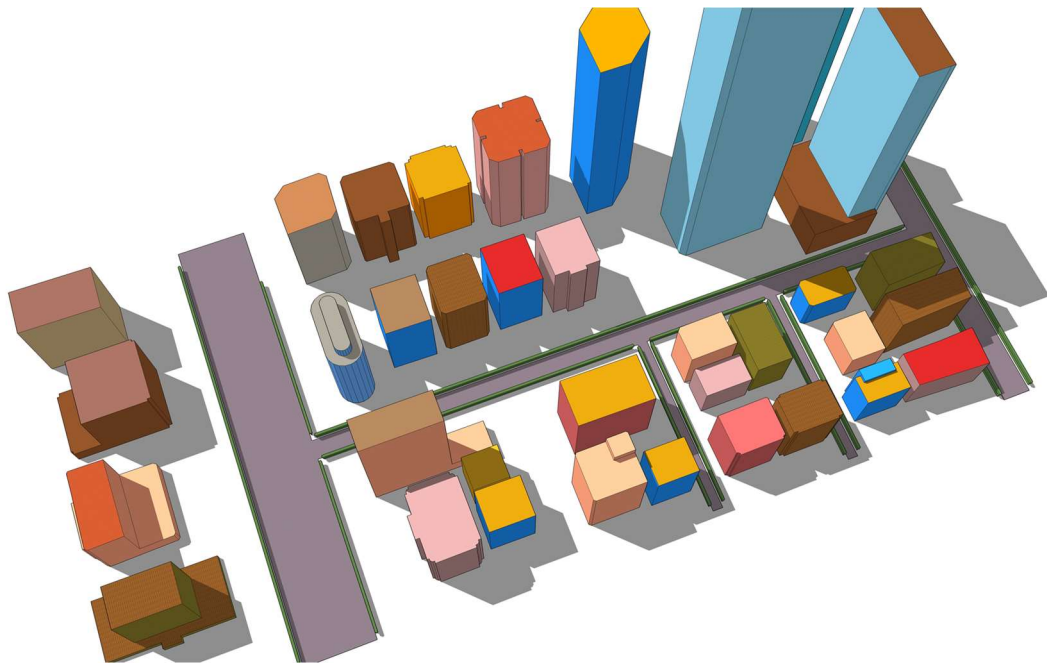


Figure 4-6: Seoul urban street model

For the highway scenario, a reconstructed model is provided in Figure 4-7 assuming 8-lane highway with a metal noise barrier in the middle of the highway.

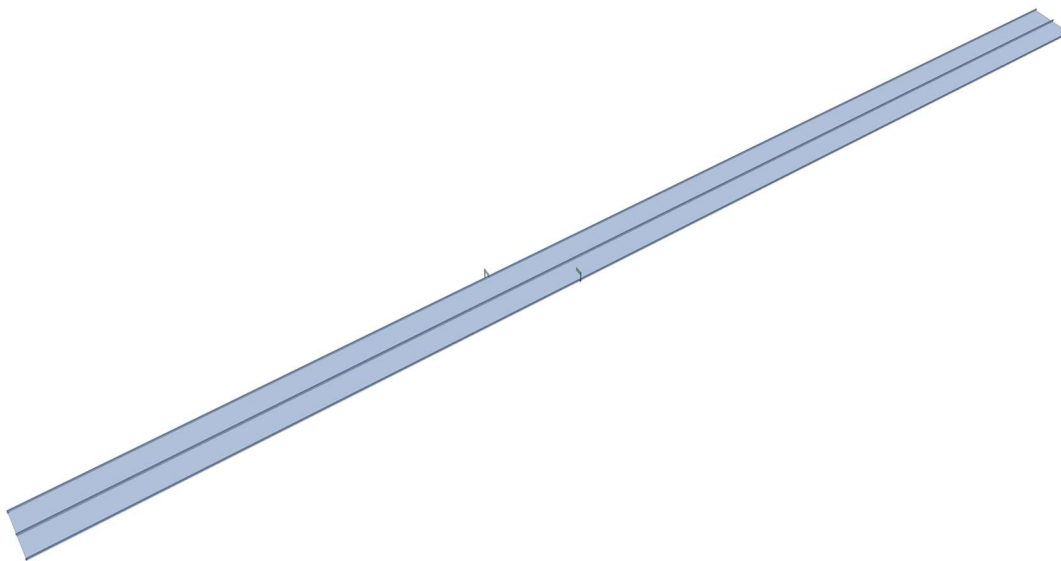


Figure 4-7: Highway model

In order to restore real urban and highway scenarios, roadside trees and some common small-scale objects such as traffic lights, traffic signs, bus stations are considered in the simulation, as seen in Figure 4-8 and Figure 4-9.

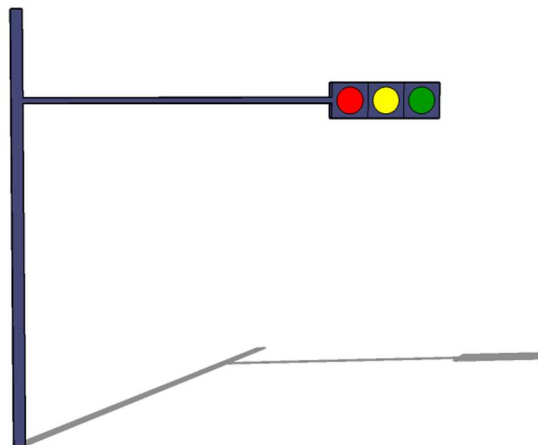


Figure 4-8: Traffic light model

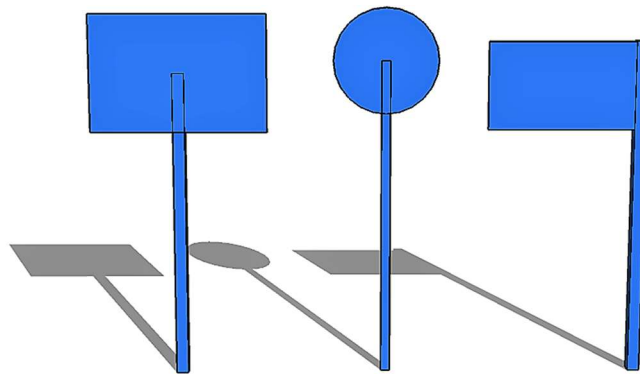


Figure 4-9: Traffic signs model

4.5.4 Configuration details

The considered carrier frequency for the simulation is 22.6 GHz with a bandwidth of 1 GHz for the terrestrial MN system. Both Tx and Rx beam patterns are same as the Tx antenna beam pattern of MN system. For urban city, the Tx is placed on top of the building with a height of 25 m. For the highway scenario, the Tx is placed on the traffic light with a height of 10 m. As shown in Figure 4-10, the Rx is placed on top of the bus at a height of 3.2 m (bus height: 3 m) located 0.1 m from the rear. The travel distance of the bus, where Rx is located is 500 m for both urban and highway scenarios.

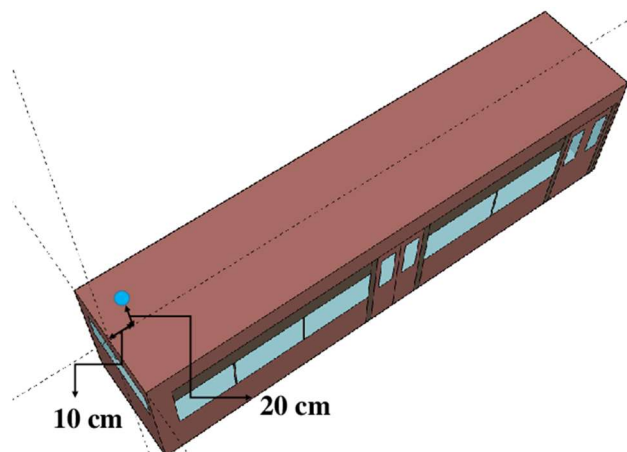


Figure 4-10: Rx location at a bus for MN system

For the satellite-terrestrial communication link, the carrier frequency (22.1 – 23.1 GHz) is the same as the terrestrial MN system. In addition, the communication scenario and the travel track are also the same with the terrestrial mobile network system. The main difference is that the location of the Tx is aboard Koreasat 6, a GEO satellite, positioned at 116° E above the equator. The distance from the satellite to the target scenarios in Seoul is approximately 37470 km. As shown in Figure 4-11, the Rx is carried by an SUV and placed on top of the SUV at a height of 2.4 m (SUV height: 1.75 m) located 1.48 m from the rear.

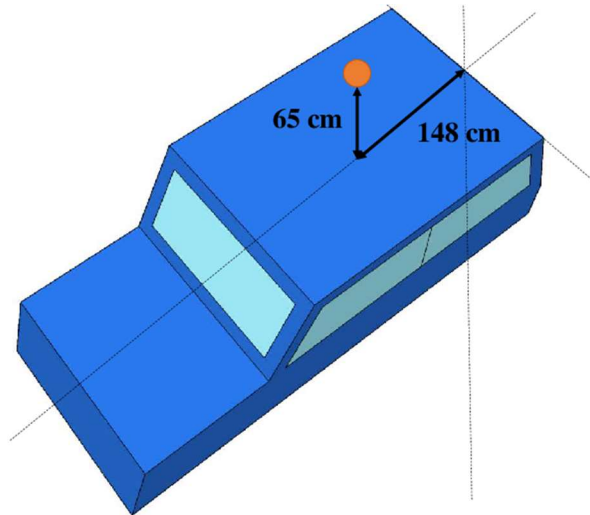


Figure 4-11: Rx location at an SUV for satellite service

Table 4-2 and Table 4-3 conclude the scenario configurations for terrestrial MN system and satellite communication link, respectively. The communication scenarios for both system are almost the same. The most differences are the locations of Tx and the selected antennas for Tx and Rx. In the simulations, direct, reflection, scattering, diffraction and transmission are considered.

Table 4-2: Scenario configuration for terrestrial MN system

Frequency	22.1 – 23.1 GHz		
Bandwidth	1 GHz		
Antenna	Directional antenna		
Tx	Power		20 dBm
	Maximum antenna gain		16 dBi
	Antenna beamwidth		20 degree
	Height	Urban scenario	25 m
		Highway scenario	10 m
Rx	Maximum antenna gain		22 dBi
	Antenna beamwidth		20 degree
	Height		3.2 m
	Travel distance for urban scenario		500 m
	Travel distance for highway scenario		500 m
V2I path	D1: Rx on the Lane 3 (4-lane urban street)		
	D2: Rx on the Lane 5 (8-lane highway)		
Vehicle type	Bus	Shown in Figure 4-2	

Table 4-3: Scenario configuration for satellite link

Frequency	22.1 – 23.1 GHz	
Bandwidth	1 GHz	
Antenna	Directional antenna	
Tx	Power	40.6 dBm
	Maximum antenna gain	53 dBi
	Antenna beamwidth	1 degree
	Approximate distance to Rx	37469.3 km
Rx	Maximum antenna gain	32 dBi
	Antenna beamwidth	3 degree
	Height	2.4 m
	Travel distance for urban scenario	500 m
	Travel distance for highway scenario	500 m
V2I path	D1: Rx on the Lane 3 (4-lane urban street)	
	D2: Rx on the Lane 5 (8-lane highway)	
Vehicle type	SUV	Shown in Figure 4-3

The setup for the simulations is detailed in Table 4-4.

Table 4-4: Simulation setup

Propagation	direct	✓
	reflection	up to 2 nd order
	diffraction	UTD
	scattering	directive scattering model
	transmission	✓
Material	building	brick, marble, toughened glass
	urban furniture, vehicle	metal
	tree	wood
	ground, highway fence	concrete

Table 4-5 summarizes EM parameters of the involved materials, where ε'_r is the real part of the relative permittivity, $\tan \delta$ is the loss tangent, S and α are the scattering coefficient and scattering exponent of the directive scattering model [24]. Particularly, the parameters of wood are calibrated in [25] and [26], while the parameters of concrete are calibrated in [27].

Table 4-5: EM parameters of different materials

Material	ε'_r	$\tan \delta$	S	α
Brick	1.9155	0.0568	0.0019	49.5724
Marble	3.0045	0.2828	0.0022	15.3747
Toughened glass	1.0538	23.9211	0.0025	5.5106
Metal	1	10^{-7}	0.0026	17.7691
Concrete	5.4745	0.0021	0.0011	109
Wood	6.6	0.9394	0.0086	13.1404

Table 4-6 summarizes the propagation mechanisms for different objects in the simulation environment.

Table 4-6: Propagation mechanisms

Object	LOS	Reflection(up to 2 order)	Scattering	Transmission	Diffraction
Tree	✓		✓	✓	
Buildings	✓	✓	✓		✓
Traffic signs	✓	✓			✓
Signal lights	✓	✓			✓
Bus stations	✓	✓			✓
Ground	✓	✓	✓		
Vehicles	✓	✓	✓		✓

Two different weather conditions are considered, i.e. rainy and sunny day; two communication scenarios are considered, i.e. urban and highway scenario. In addition, the interference between the MN system and satellite-terrestrial wireless communication system are also under consideration. Hence, 16 cases are considered in total in this work. They are summarized in Table 4-7 for clarity. The abbreviations should be noted in this table. BS and VeUE is short for base station and vehicle user equipment, respectively, which are served by the terrestrial MN system. SA and SaUE is short for satellite antenna and satellite user equipment, respectively.

Table 4-7: Considered simulation scenarios

Index	Environment	Tx	Rx	Weather	Signal	Interference	Terminology
1	Urban	BS	VeUE	Rainy	✓		Urban-BS2VeUE-R
2	Urban	BS	VeUE	Sunny	✓		Urban-BS2VeUE-S
3	Urban	BS	SaUE	Rainy		✓	Urban-BS2SaUE-R
4	Urban	BS	SaUE	Sunny		✓	Urban-BS2SaUE-S
5	Urban	SA	SaUE	Rainy	✓		Urban-SA2SaUE-R
6	Urban	SA	SaUE	Sunny	✓		Urban-SA2SaUE-S
7	Urban	SA	VeUE	Rainy		✓	Urban-SA2VeUE-R
8	Urban	SA	VeUE	Sunny		✓	Urban-SA2VeUE-S
9	Highway	BS	VeUE	Rainy	✓		Highway-BS2VeUE-R
10	Highway	BS	VeUE	Sunny	✓		Highway-BS2VeUE-S
11	Highway	BS	SaUE	Rainy		✓	Highway-BS2SaUE-R
12	Highway	BS	SaUE	Sunny		✓	Highway-BS2SaUE-S
13	Highway	SA	SaUE	Rainy	✓		Highway-SA2SaUE-R
14	Highway	SA	SaUE	Sunny	✓		Highway-SA2SaUE-S
15	Highway	SA	VeUE	Rainy		✓	Highway-SA2VeUE-R
16	Highway	SA	VeUE	Sunny		✓	Highway-SA2VeUE-S

4.6 Key channel parameters

The channel characteristics for a terrestrial MN system and satellite-terrestrial communication links in urban and highway environments considering two weather conditions (rainy and sunny day) were evaluated based on extensive RT simulation results. For that, the following related

parameters were considered, i.e. path loss (PL), root-mean-square (RMS) delay spread (DS), Rician K -factor (KF), azimuth angular spread of arrival (ASA), azimuth angular spread of departure (ASD), elevation angular spread of arrival (ESA) and elevation angular spread of departure (ESD).

All these channel parameters are fitted by a normal distribution with mean value μ and standard deviation (STD) σ . The extracted parameters are summarized in Table 4-8, Table 4-9 and Table 4-10, where μ_{DS} , μ_{KF} , μ_{ASA} , μ_{ASD} , μ_{ESA} , μ_{ESD} are the mean values of DS, KF, ASA, ASD, ESA, ESD, respectively. The standard deviations of DS, KF, ASA, ASD, ESA, and ESD are σ_{DS} , σ_{KF} , σ_{ASA} , σ_{ASD} , σ_{ESA} , and σ_{ESD} , respectively. As we consider the rain will have severe impact on the channel characteristics, the channel characteristics under rainy condition are analyzed firstly. The suffix -R in the scenario name represents the rainy condition, as introduced in Table 4-7.

4.6.1 Path loss

The path loss describes the amount of signal attenuation between a receiver and a transmitter, which considers the impacts of the propagation path and the distribution of the scatterers in the environment. Considering the transmit power and the antenna gain on both Tx and Rx sides, the received power can be calculated as follows:

$$P_{Rx} = P_{Tx} + G_{Tx} - PL + G_{Rx} \quad (4-7)$$

where P_{Rx} and P_{Tx} are the received and transmit power in dBm, respectively. G_{Tx} and G_{Rx} are the Rx and Tx antenna gain in dBi, respectively. PL represents the path loss in dB.

The received power for all scenarios and all links (listed in Table 9) is shown in Figure 4-12 and Figure 4-13. Dense raindrops cause serious transmission attenuation for high-frequency radio waves above Ku-band (12 - 18 GHz) when passing through the rainy area. Therefore, based on ITU-R P.618-13, the maximum attenuation due to rain at 99.99% and 95% of an average year are considered in this task (22.1 - 23.1 GHz), respectively. In Figure 4-12 and Figure 4-13, the red dotted lines represent the minimum received power at 99.99% of an average year. In the other words, the received power at 99.99% of an average year will be higher than the value in the figures. The green solid lines show the minimum received power at 95% of an average year, which indicates that in the whole year, the received power at 95% of an average year will be higher than the value in the figures. The blue dotted lines represent the received power under the sunny day.

Figure 4-12 shows the received power of the terrestrial-terrestrial links for urban and highway scenarios. For both urban and highway scenarios, the deep fading at a distance around 100 m and 500 m is due to the blockage by the traffic lights on the road. In the cases of Seoul-urban1-BS2VeUE (shown in Figure 4-12 (c)) and Highway-BS2VeUE (shown in Figure 4-12 (d)), when the distance between Tx and Rx is relatively short (distance < 100 m), the received power is relatively low. For the case of Highway-BS2VeUE, due to the limitation of the highway scenario, the Tx can only be placed on both sides of the road, which causes the Rx not always being in the main lobe of the Tx. For the case of Seoul-urban1-BS2VeUE, on the one hand, Tx is usually located above the building, resulting in the distance between the transceivers often not being as close as in the highway scenario; on the other hand, in the simulation, the starting distance between the transceivers is also relatively large (about 90 m). When the starting distance between the transceivers is shortened, the simulation results will be similar to the case of Highway-BS2VeUE. Moreover, the deviation between the received power under the considerations of maximum rain attenuation and no rain does not exceed 10 dB for the terrestrial-terrestrial links (shown in Figure 4-12).

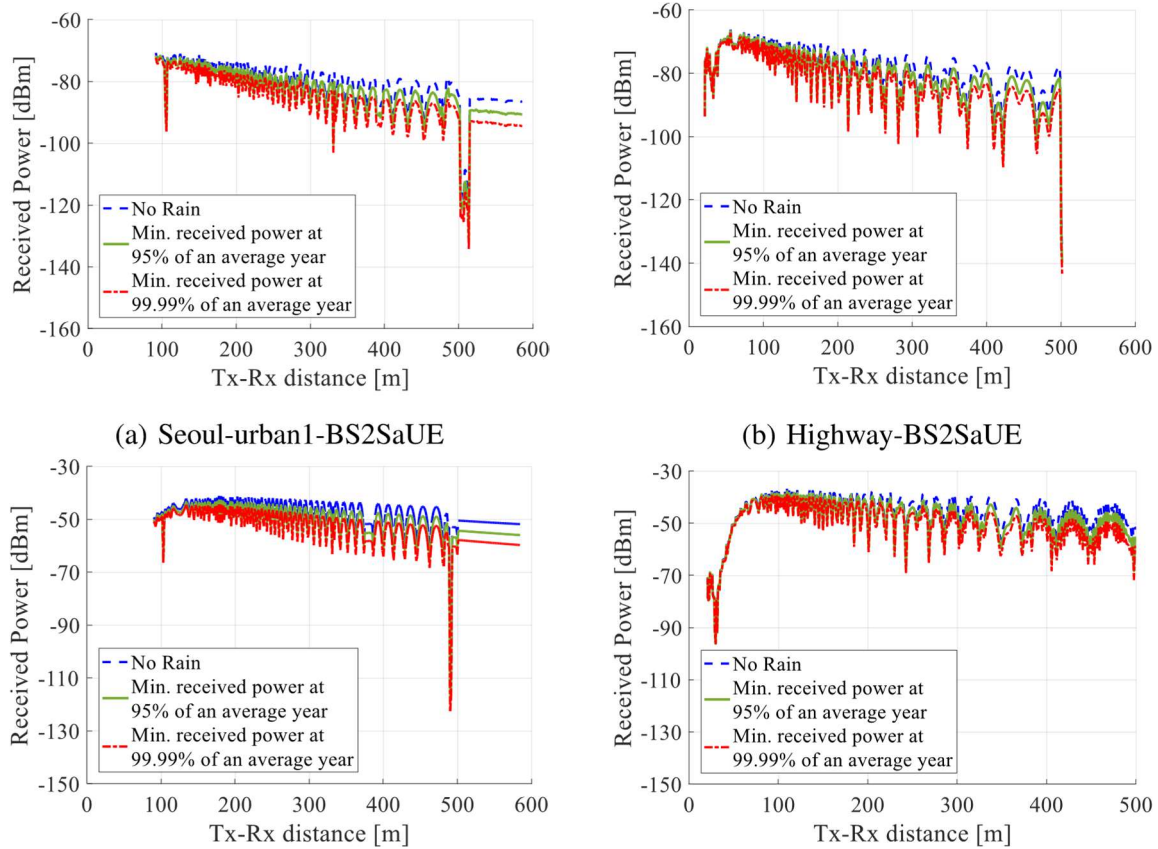


Figure 4-12: Received power when the base station is transmitting

From Figure 4-13, the received power of satellite-terrestrial links for urban and highway scenarios is similar. The deep fading in Figure 4-13 (a) and (c) is also caused by the blockage of traffic lights on the road. Compared to the terrestrial-terrestrial links, due to the change in the geometry of the transceivers position and the obstacles, the position of deep fading in the satellite-terrestrial links is different from the terrestrial-terrestrial links. Moreover, on rainy days, the received power is approximately 30 dB less than that on the sunny day.

In summary, the results indicate that the rain attenuation has a greater influence on the satellite-terrestrial link than the terrestrial-terrestrial link. This is because the distance between the transceivers in the terrestrial-terrestrial link is much shorter than the distance between the transceivers in the satellite-terrestrial link, resulting in a greater impact from rain attenuation on the satellite-terrestrial link.

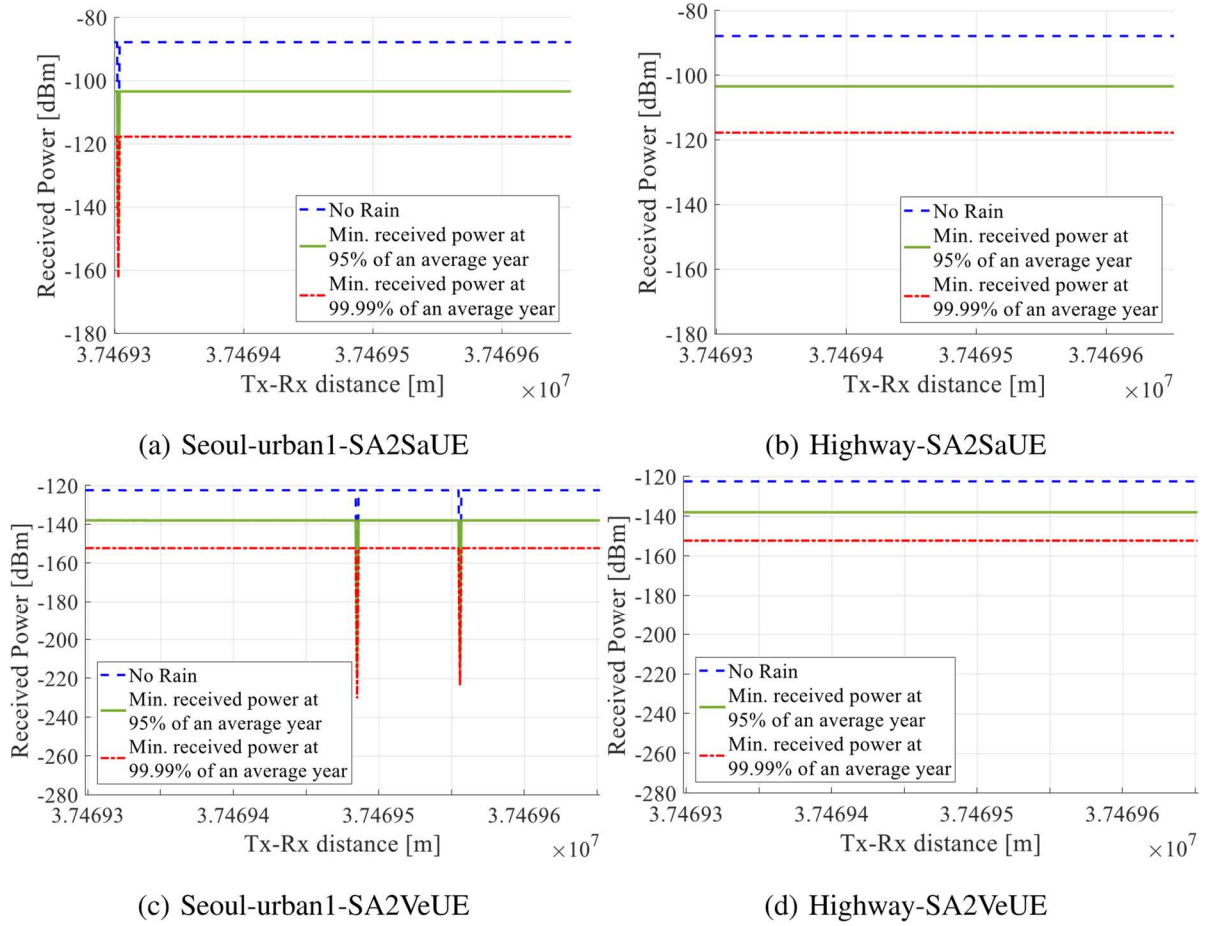


Figure 4-13: Received power when the satellite is transmitting

4.6.2 RMS delay spread

The RMS delay spread is used to quantify the dispersion effect due to multipath propagation in the time delay domain. It is defined as the square root of the second central moment of the power delay profile (PDP) [28]:

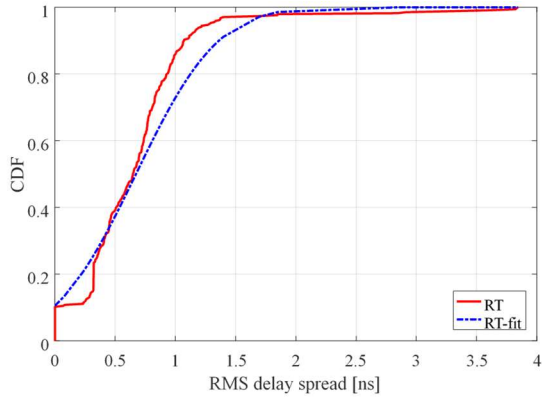
$$\sigma_{\tau} = \sqrt{\frac{\sum_{n=1}^N \tau_n^2 \cdot P_n}{\sum_{n=1}^N P_n} - \left(\frac{\sum_{n=1}^N \tau_n \cdot P_n}{\sum_{n=1}^N P_n} \right)^2} \quad (4-8)$$

where σ_{τ} denotes the RMS delay spread, P_n and τ_n denote the power and the excess delay of the n -th multipath, respectively. The cumulative distribution functions (CDFs) of the RMS delay spreads σ_{τ} in the simulations are shown in Figure 4-14 and Figure 4-15 for the urban and highway scenario, respectively. The mean values and the STDs of the RMS delay spread for each scenario are listed in Table 4-8.

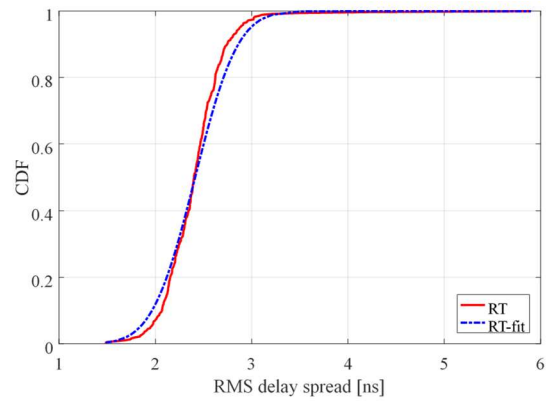
Table 4-8: Extracted parameters for the DS

Scenario	DS [ns]	
	μ_{DS}	σ_{DS}
Urban-BS2VeUE-R	0.67	0.54
Urban-SA2VeUE-R	2.41	0.35
Urban-BS2SaUE-R	3.63	18.72
Urban-SA2SaUE-R	2.42	0.33

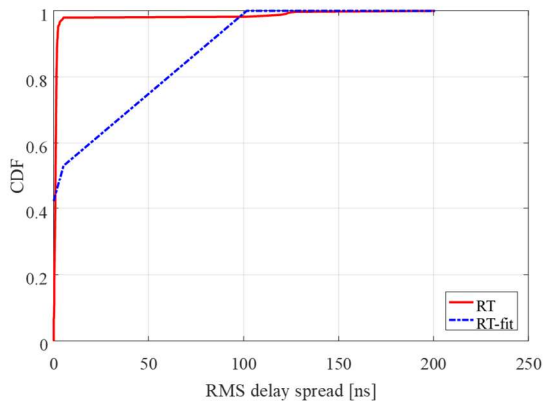
Highway-BS2VeUE-R	3.53	3.78
Highway-SA2VeUE-R	2.37	0.25
Highway-BS2SaUE-R	1.86	25.74
Highway-SA2SaUE-R	2.36	0.25



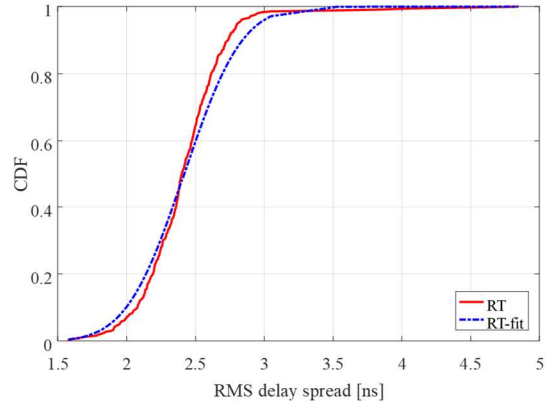
(a) Urban-BS2VeUE-R



(b) Urban-SA2VeUE-R



(c) Urban-BS2SaUE-R



(d) Urban-SA2SaUE-R

Figure 4-14: RMS delay spread for the urban scenarios

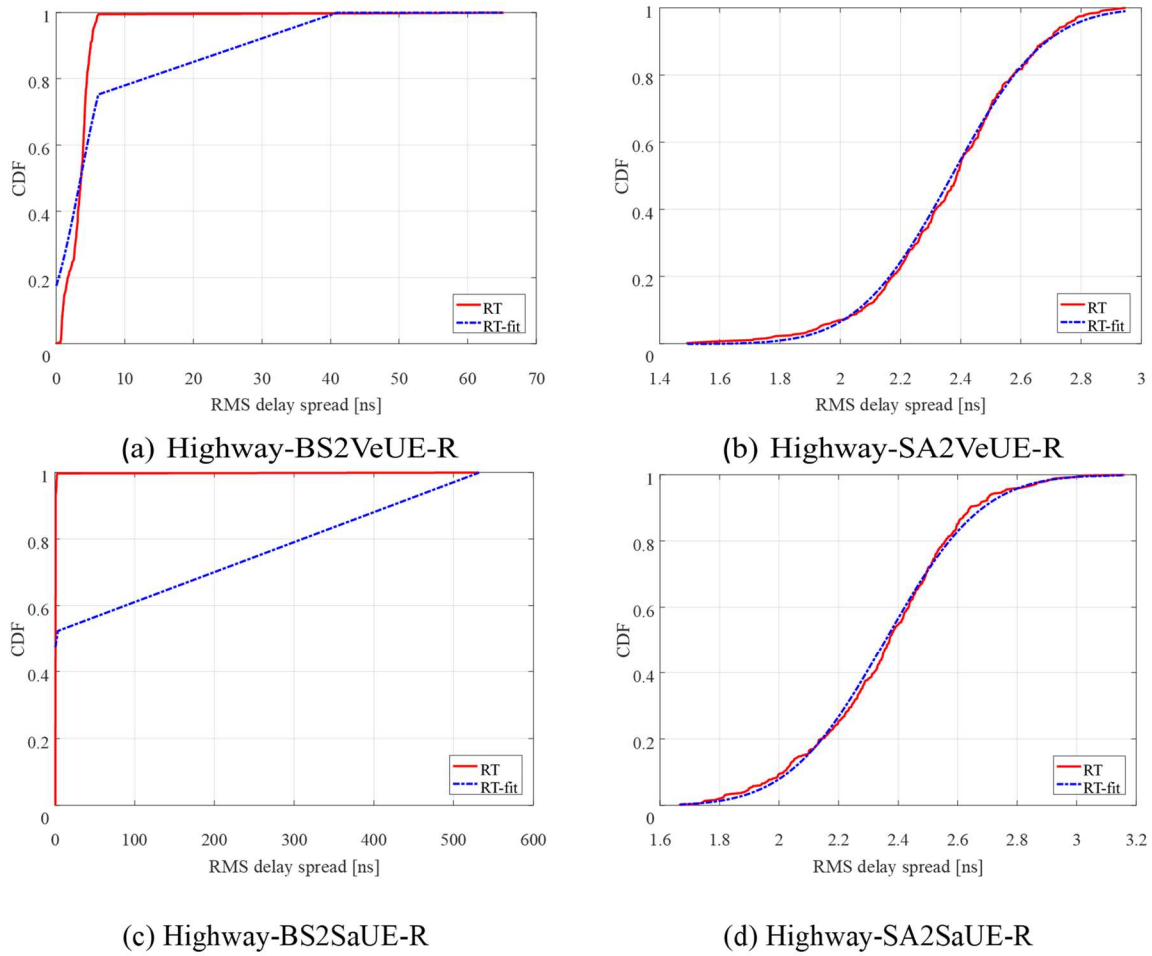


Figure 4-15: RMS delay spread for the highway scenarios

From these figures and the table, it can be seen that in the urban scenario, the μ_{DS} of the satellite communication link (Urban-SA2VeUE-R and Urban-SA2SaUE-R) are similar. For these two cases, with a 90% probability, the RMS delay spread values are less than 3 ns, which means that most of the strong multipath components (MPCs) are concentrated around the LOS path in the time delay domain. It is consistent with the RT simulation results that the scattered rays are mainly scattered on the top of the vehicle. However, an unanticipated RMS delay spread value of 200 ns is observed in the case of Urban-BS2SaUE-R (shown in Figure 4-14 (c)). It is due to the large power and the long delay of the reflection path caused by the distant metal traffic light.

It can be noted that the μ_{DS} of the satellite-terrestrial communication link (Highway-SA2VeUE-R and Highway-SA2SaUE-R) are similar to the results for the urban scenarios. In the case of Highway-BS2VeUE-R (shown in Figure 4-15 (a)), the large DS value is due to the large power and the long delay of the reflection path by the distant metal traffic sign.

However, in the case of Highway-BS2SaUE-R (shown in Figure 4-15 (c)), there is a snapshot that causes the value of the DS to be very large. This might be explained by the misalignment of the direct path and the antenna's main lobe. Under the condition of direct path outside the main lobe, the power is relatively low. However, the scattered and reflected rays from the distant metal traffic light is within the main lobe of the antenna pattern as a result that the power of these rays is relatively high.

4.6.3 Rician K -factor

The Rician K -factor is a key parameter to quantify the channel fading severity, which is defined as the ratio between the power of the strongest component and the sum power of the remaining

components of the received signal [29]. For the narrow-band channel sounding measurement results, the Rician K -factor should be calculated based on moment methods [30]. However, the ultra-wideband (UWB) channel sounding results in this measurement have high resolution in the time domain. Thus, the Rician K -factor can be calculated according to the following definition:

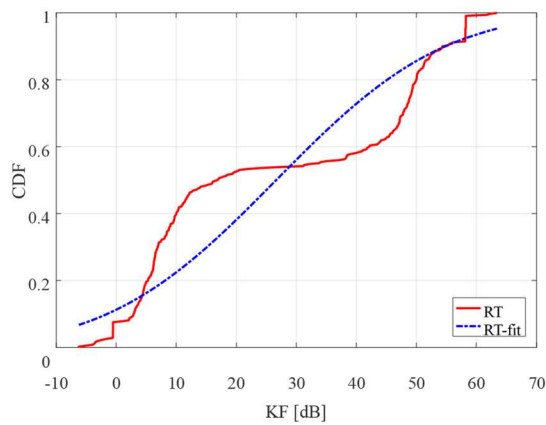
$$KF(\text{dB}) = 10 \cdot \log_{10} \left(\frac{P_{\text{strongest}}}{\sum P_{\text{remaining}}} \right) \quad (4-9)$$

where KF denotes the Rician K -factor, $P_{\text{strongest}}$ and $P_{\text{remaining}}$ denote the power of the strongest component and the power of each of the remaining components, respectively.

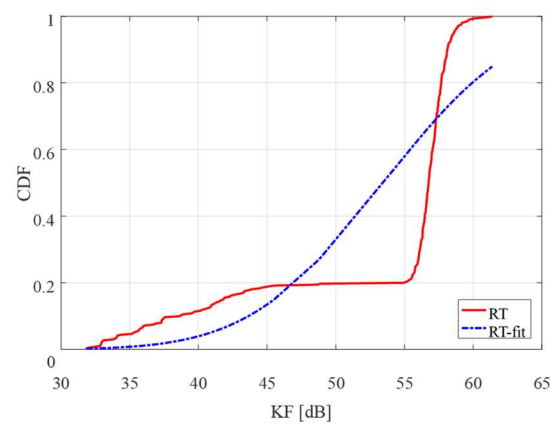
The fitting results for the Rician K -factor are summarized in Table 4-9 and the CDFs are compared in Figure 4-16 and Figure 4-17. From the table and these figures we can find that for satellite-terrestrial communication link, no matter the environment (urban or highway), shows a mean KF μ_{KF} of around 55 dB. The large mean values of the KF indicate that the direct ray contributes more significantly compared to the other rays (an exemplary snapshot is shown in Figure 4-17).

Table 4-9: Extracted parameters for the K -factor

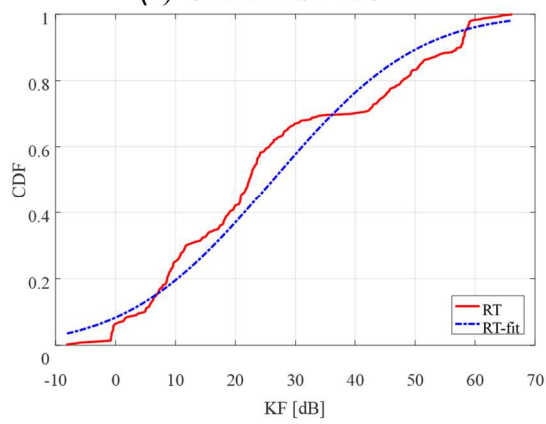
Scenario	KF [dB]	
	μ_{KF}	σ_{KF}
Urban-BS2VeUE-R	26.61	21.96
Urban-SA2VeUE-R	53.44	7.67
Urban-BS2SaUE-R	26.26	18.98
Urban-SA2SaUE-R	56.76	1.27
Highway-BS2VeUE-R	9.65	7.07
Highway-SA2VeUE-R	54.48	6.81
Highway-BS2SaUE-R	7.30	11.10
Highway-SA2SaUE-R	57.06	0.94



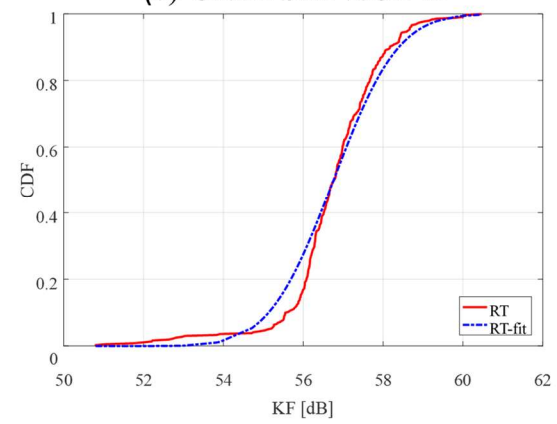
(a) Urban-BS2VeUE-R



(b) Urban-SA2VeUE-R



(c) Urban-BS2SaUE-R



(d) Urban-SA2SaUE-R

Figure 4-16: Rician K -factor for the urban scenarios

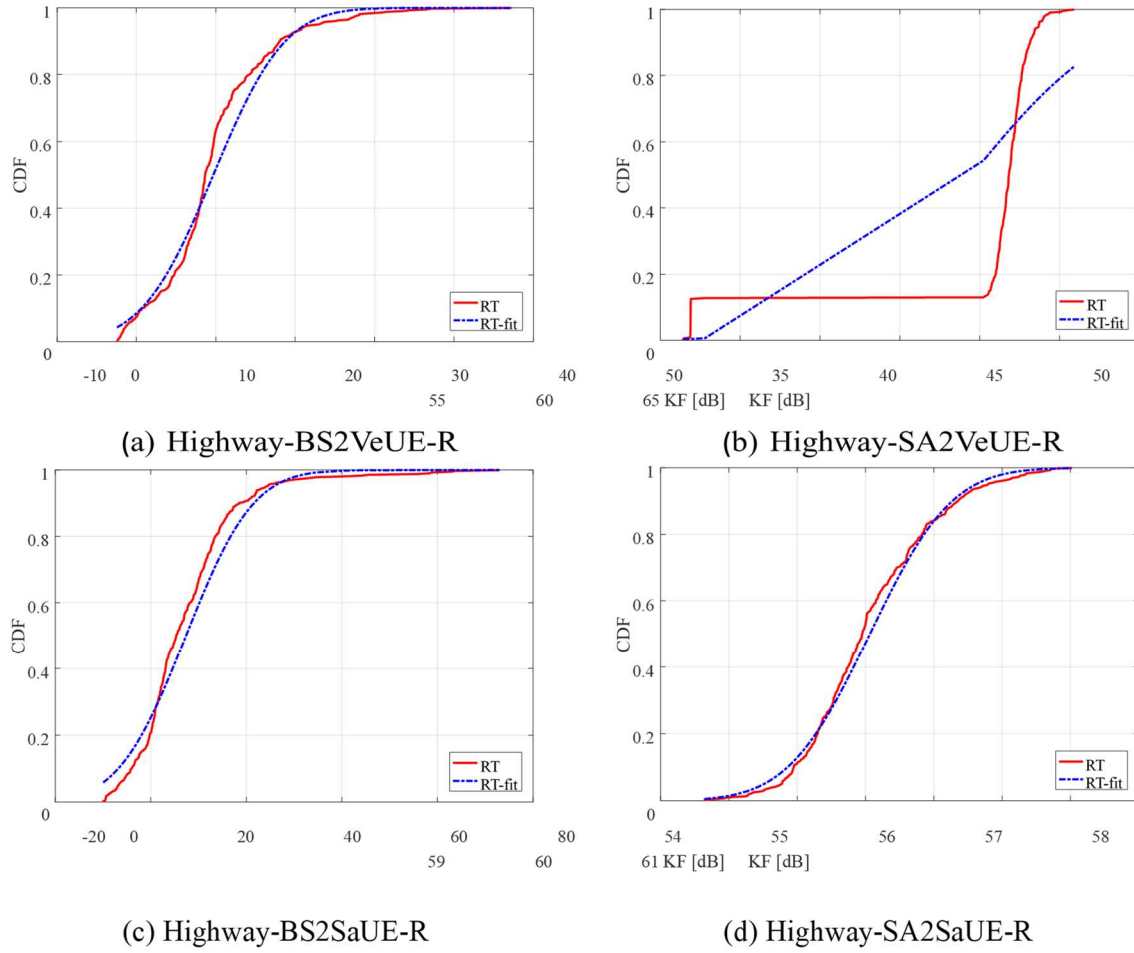


Figure 4-17: Rician K -factor for the highway scenarios

4.6.4 Angular domain

Based on the 3GPP definition, the conventional angular spread calculation for the composite signal is given by

$$\sigma_{AS} = \sqrt{\frac{\sum_{n=1}^N (\theta_{n,\mu})^2 \cdot P_n}{\sum_{n=1}^N P_n}} \quad (4-10)$$

where σ_{AS} denotes the angular spread, P_n denotes the power of the n -th multipath, and $\theta_{n,\mu}$ is defined by:

$$\theta_{n,\mu} = \text{mod}(\theta_n - \mu_\theta + \pi, 2\pi) - \pi \quad (4-11)$$

further, μ_θ is defined as:

$$\mu_\theta = \frac{\sum_{n=1}^N \theta_n \cdot P_n}{\sum_{n=1}^N P_n} \quad (4-12)$$

and θ_n is the angle of arrival/departure of the n -th multipath.

The angular spread values for each case can be found in Table 4-10. In general, the satellite-terrestrial communication links, no matter the environment (urban or highway), show very small mean values for the angular spreads (ASA, ASD, ESA, ESD), even close to zero. This indicates that the number of MPCs is lower than in a terrestrial MN system, and that these MPCs are mainly concentrated in LOS direction.

Table 4-10: Extracted parameters for the angular spreads

Scenario	ASD [°]		ESD [°]		ASA [°]		ESA [°]	
	μ_{ASD}	σ_{ASD}	μ_{ESD}	σ_{ESD}	μ_{ASA}	σ_{ASA}	μ_{ESA}	σ_{ESA}
Urban-BS2VeUE-R	0.15	0.18	0.43	0.22	0.31	4.06	3.40	1.77
Urban-SA2VeUE-R	0.16	0.39	0	0	0.02	0.02	0.06	0.08
Urban-BS2SaUE-R	0.28	0.28	0.31	0.15	3.33	10.84	3.97	4.88
Urban-SA2SaUE-R	0	0	0	0	0	0	0	0
Highway-BS2VeUE-R	1.60	0.81	0.94	0.89	34.30	28.61	3.20	3.55
Highway-SA2VeUE-R	0.01	0.04	0	0	0.01	0.02	0.04	0.02
Highway-BS2SaUE-R	0.34	0.35	0.76	0.77	4.43	3.88	3.49	4.05
Highway-SA2SaUE-R	0	0	0	0	0	0	0	0

5 Conclusions

D3.1 is the first deliverable of WP3, Spectrum Sharing. It is of major importance in the development of the project. Indeed, 5G-ALLSTAR aims at studying cellular / satellite multi-connectivity, in which feasibility and performance highly rely on spectrum usage and network deployment of both systems, which are addressed in this document. Furthermore, the design of efficient algorithms for the coordination of the systems requires accurate channel modelling, also covered by this deliverable.

In a first part, the spectrum situation for 5G is examined. First, the two streams of discussion in ITU are summarized: definition of new interfaces for IMT-2020 and identification of new frequency bands for IMT-2020. NR frequency ranges FR1 and FR2, from 3GPP, are then recalled. Thirdly, an overview of regulatory and licensing issues of 5G satellite system use in mobile bands is provided. Finally, this section describes in detail the frequency bands currently eligible for 5G by satellite, which could be simultaneously used by both terrestrial and non-terrestrial 5G systems. These bands are L-band (1427-1518 MHz), S-band (1980-2010 MHz for uplink and 2170-2200 MHz for downlink), C-band (3.3-4.2 GHz) and Ka-band (24.25- 27.5 GHz).

In a second part, the 5G deployment scenarios are detailed based on the reference system architecture implementing these solutions designed in deliverable D2.2:

- For non-terrestrial networks, 5G-ALLSTAR considers two complementary deployments: GEO satellite deployment in Ka-band and LEO satellite deployment in S-band. An additional scenario, which was not included in the 3GPP NTN deployment scenario, is also in the scope of the project: GEO satellite deployment in Ku-band.
- The terrestrial networks studied in the frame of 5G-ALLSTAR are:
 - Vehicular terminals in two different environments are envisioned: highway and urban.
 - Fixed or handheld terminals, in which BSs are deployed according to a hexagonal grid, with 19 sites and 3 sectors per site.

The terminal deployment is described in a third part. The focus lies on vehicle-type terminals (highway and urban scenarios) and on fixed or handheld terminals. Assumptions on the terminal distributions and movements are provided.

Finally, two channel models are developed in 5G-ALLSTAR, described respectively in the third and in the fourth chapter of this document:

- A geometry-based stochastic channel model based on 3GPP TR 38.811 v15.0.0. The work in 5G-ALLSTAR aims at providing an implementation and further extensions (radio propagation model for LEO and GEO satellites) of this channel model within the QuaD-RiGa channel simulator.
- A ray-tracing based channel model. Simulation is conducted in order to investigate the channel characteristics for a scenario where both the terrestrial moving network and satellite systems provide connectivity to a vehicle

This deliverable provides inputs to:

- Task 3.2 of WP3 (interference analysis of shared spectrum). The analysis of the interference between same or different access systems relies on spectrum, deployment scenarios and channel modelling.
- Task 3.3 of WP3 (algorithms and techniques for interference management). Signal processing techniques for active interference mitigation are studied in this task; frequency bands and channel parameters are required.

- Task 3.4 of WP3 (interference mitigation through RRM). For this task, D3.1 provides spectrum usage and terminal deployment information.
- WP5 (Prototyping, validation and demonstration). The QuaDRiGa channel model described in this document will feed the channel emulator in the European testbed in order to realize a combined satellite/cellular emulation of test scenarios.

References

- [1] 3GPP TS 36.101, "User Equipment (UE) radio transmission and reception (Release 16)," v16.1.0, Tech. Rep., 2019.
- [2] FCC 18-91, Order and Notice of Proposed Rulemaking, Jul. 2018.
- [3] 3GPP TR 38.811, "Study on New Radio (NR) to support non terrestrial networks (Release 15)," v15.0.0, Tech. Rep., 2018.
- [4] S. Jaeckel, L. Raschkowski, K. Börner, L. Thiele, F. Burkhardt and E. Eberlein, "QuaDRiGa - Quasi Deterministic Radio Channel Generator, User Manual and Documentation", Fraunhofer Heinrich Hertz Institute, Tech. Rep. v2.2.0, Online: <https://quadriga-channel-model.de>, 2019.
- [5] 3GPP TR 38.901, "3rd Generation Partnership Project; Technical Specification Group Radio Access Network; Study on channel model for frequencies from 0.5 to 100 GHz (Release 14)," v15.0.0, Tech. Rep., 2018.
- [6] ITU-R S.1503-3, "Functional description to be used in developing software tools for determining conformity of non-geostationary-satellite orbit fixed-satellite service systems or networks with limits contained in Article 22 of the Radio Regulations", Tech. Rep., 2018
- [7] S. Jaeckel, L. Raschkowski, K. Börner, and L. Thiele, "QuaDRiGa: A 3-D multi-cell channel model with time evolution for enabling virtual field trials," IEEE Trans. Antennas Propag., vol. 62, pp. 3242-3256, 2014.
- [8] Online: <https://commons.wikimedia.org/wiki/File:Orbit1.svg>
- [9] S. Jaeckel, "Quasi-deterministic channel modeling and experimental validation in cooperative and massive MIMO deployment topologies", PHD Thesis, TU Ilmenau, 2017
- [10] S. Jaeckel, L. Raschkowski, F. Burkhardt, L. Thiele, "Efficient Sum-of-Sinusoids based Spatial Consistency for the 3GPP New-Radio Channel Model", Proc. IEEE Globecom Workshops '18, 2018
- [11] ITU-R P.676-10, "Attenuation by atmospheric gases", Tech. Rep., 2013
- [12] ITU-R P.835-6, "Reference standard atmospheres", Tech. Rep., 2018
- [13] N. J. Higham, "Newton's method for the matrix square root," Mathematics of Computation, vol. 46, no. 174, pp. 537–549, 1986. [Online]. Available: <http://www.jstor.org/stable/2007992>
- [14] M. Peter, R. J. Weiler, F. Undi, F. El-Kanawati, S. Jaeckel, L. Raschkowski, L. Thiele, K. Sakaguchi, and W. Keusgen, "Investigations on the frequency dependence of the delay spread in an UMi street canyon scenario," in 2016 International Symposium on Antennas and Propagation (ISAP), Oct 2016, pp. 616–617.
- [15] J. Nuckelt, M. Schack, and T. Kürner, "Geometry-based path interpolation for rapid ray-optical modeling of vehicular channels", In 2015 9th European Conference on Antennas and Propagation (EuCAP), pages 1–5, April 2015.
- [16] M. Armbrust, A. Fox, R. Griffith, A. D. Joseph, R. Katz, A. Konwinski, G. Lee, D. Patterson, A. Rabkin, I. Stoica, and M. Zaharia, "A view of cloud computing", Communications of the ACM, 53(4), 2010.
- [17] ITU-R P.530-17, "Propagation data and prediction methods required for the design of terrestrial line-of-sight systems", Technical report, ITU Recommendations, 2017.
- [18] ITU-R P.676-11, "Attenuation by atmospheric gases". Technical report, ITU Recommendations, 2016.
- [19] ITU-R P.837-7, "Characteristics of precipitation for propagation modelling", Technical report, ITU Recommendations, 2017.
- [20] ITU-R P.838-3, "Specific attenuation model for rain for use in prediction methods", Technical report, ITU Recommendations, 2005.
- [21] ITU-R P.618-13, "Propagation data and prediction methods required for the design of earth-space telecommunication systems", Technical report, ITU Recommendations, 2017.

- [22] ITU-R P.840-7, "Attenuation due to clouds and fog", Technical report, ITU Recommendations, 2017.
- [23] ITU-R S.465-6, "Reference radiation pattern of earth station antennas in the fixed-satellite service for use in coordination and interference assessment in the frequency range from 2 to 31 GHz", Technical report, ITU Recommendations, 2010.
- [24] V. Degli-Esposti, F. Fuschini, E. M. Vitucci, and G. Falciaeseca, "Measurement and modelling of scattering from buildings", IEEE Transactions on Antennas and Propagation, 55(1):143–153, Jan 2007.
- [25] F. Wang, and K. Sarabandi, "An enhanced millimeter-wave foliage propagation model", IEEE Transactions on Antennas and Propagation, 53(7):2138–2145, July 2005.
- [26] H. M. Rahim, C. Y. Leow, and T. A. Rahman, "Millimeter wave propagation through foliage: Comparison of models", In 2015 IEEE 12th Malaysia International Conference on Communications (MICC), pages 236–240, Nov 2015.
- [27] K. Guan, B. Ai, B. Peng, D. He, G. Li, J. Yang, Z. Zhong, and T. Kürner, "Towards realistic high-speed train channels at 5G millimeter-wave band - Part II: Case study for paradigm implementation", IEEE Transactions on Vehicular Technology, 67(10):9129–9144, Oct 2018.
- [28] T. Rappaport, "Wireless Communications: Principles and Practice", Upper Saddle River, NJ, USA: Prentice-Hall, 22nd ed. edition, 2002.
- [29] L. Bernado, T. Zemen, F. Tufvesson, A. F. Molisch, and C. F. Mecklenbräuker, "Time- and frequency-varying K-factor of non-stationary vehicular channels for safety-relevant scenarios", IEEE Transactions on Intelligent Transportation Systems, 16(2):1007–1017, April 2015.
- [30] T. Zhou, C. Tao, S. Salous, L. Liu, and Z. Tan, "Channel characterization in high-speed railway station environments at 1.89 GHz", Radio Science, 50(11):1176–1186, Nov 2015.